

ABSTRACT¹

Title of Dissertation: FIRST-PRINCIPLES COMPUTATIONAL STUDY OF FAST PROTON-CONDUCTING OXIDES.

Md Shafiqul Islam, Doctor of Philosophy, 2022

Dissertation directed by: Associate Professor Yifei Mo, Department of Materials Science and Engineering

Solid ceramic proton conductors are a crucial component for hydrogen-based energy devices, such as solid oxide fuel cells, electrolyzers, hydrogen separation membranes, and novel electronic computing devices. I performed first-principles computation to systematically investigate a wide range of perovskite and double perovskite materials and to reveal the effects of different cations and their combinations on the proton diffusion and hydrogen incorporation to rationally guide the future development of these perovskite proton conductors. The high-throughput computation discovered a number of layered double perovskite materials with good proton incorporation capability and fast proton diffusion. The results provided the design principles for the cation mixing in perovskite proton conductors and provided new

¹ Some text of introduction is adapted from my published papers:

Islam, M. S.; Wang, S.; Nolan, A. M.; Mo, Y., “First-Principles Computational Design and Discovery of Novel Double-Perovskite Proton Conductors”, *Chem. Mater.* (2021).

Islam, M. S.; Nolan, A. M.; Wang, S.; Bai, Q.; Mo, Y. “A Computational Study of Fast Proton Diffusion in Brownmillerite Sr₂Co₂O₅”, *Chem. Mater.* 32 (2020) (12), 5028–5035.

Islam, M. S.; Wang, S.; Alex T. Hall; Mo, Y., “First-Principles Computational Design and Discovery of Solid-Oxide Proton Conductors”, submitted.

research directions for novel double perovskite proton conductors for novel energy or electronic devices.

I performed first-principles calculations to reveal the atomistic mechanisms of proton insertion and diffusion in SrCoO_{2.5} (SCO) brownmillerite structure that was reported as a fast proton conductor than typical perovskite-based oxide proton conductors. By studying the hydrogenated brownmillerite SCO in a range of H concentrations, first-principles calculations revealed the proton diffusion mechanisms in brownmillerite which give rise to faster proton diffusion than in perovskites proton conductors. The understanding of fast proton conduction mechanisms in brownmillerite provided insight into the future development and discovery of novel proton conductor materials.

I performed a systematic first-principles computation study on a wide range of ternary oxide materials to understand the role of cations and compositions on materials stabilities and proton conduction in order to identify new proton conductor materials. By analyzing a large set of computation data generated on a wide range of oxide materials with different chemical compositions, our computation revealed how the mole fraction and the species of cations affect water stabilities and hydrogen insertion. By studying the proton diffusion in many different materials, our proton diffusion analysis showed that oxide materials with connected BO₆ octahedra are optimal for fast proton diffusion. Following our materials understanding, our high-throughput computation identified a dozen oxide materials with good water stability, good proton incorporation capability, and fast proton diffusion. This thesis provided a fundamental

understanding and design principles to develop oxide proton conductor materials with good stabilities.

FIRST-PRINCIPLES COMPUTATIONAL STUDY OF FAST PROTON-
CONDUCTING OXIDES

by

Md Shafiqul Islam

Dissertation submitted to the Faculty of the Graduate School of the
University of Maryland, College Park, in partial fulfillment
of the requirements for the degree of
Doctor of Philosophy
2022

Advisory Committee:

Professor Yifei Mo, Chair

Professor Liangbing Hu

Professor Lourdes G. Salamanca-Riba

Professor Paul Albertus

Professor Chunsheng Wang, Dean's representative

© Copyright by
Md Shafiqul Islam
2022

Dedication

To my family

Acknowledgements

First of all, I would like to thank my advisor, Dr. Yifei Mo, for his guidance and support throughout my graduate study. His passion for understanding science and willingness to contribute to the development of energy industry was very inspiring for me in this Ph.D. journey. His highly insightful vision helps me to broaden my perspective to solve a problem more efficiently and think twice before execution. He teaches me to be more responsible in work, do the work with perfection, and importance to convey the scientific work as a consistent story to audience so that the work add value to the community. I also appreciate his effort to improve my scientific writing by multiple revision of manuscript, countless hours of supervision and in-chat discussion.

I would also like to thank my committee members: Dr. Liangbing Hu, Dr. Chunsheng Wang, Dr. Liangbing Hu and Dr. Lourdes G. Salamanca-Riba, and Dr. Paul Albertus.

I want to thank my lab mates, especially Dr. Qiang Bai, Dr. Shuo wang, Dr. Adelaide Nolan, and Dr. Menghao Yang. I appreciate the help from other group members: Mr. Yunsheng Liu, Mr. Alex Thomas Hall, Miss. Boyang Liu, Dr. Xingfeng He, and Dr. Yizhou Zhu. It was a great pleasure to work with you all, and I wish you all the best in the future.

I want to thank my friends for supporting me when staying away from home: Mr. Chapal Barua, Mr. Saiful Islam, Dr. Ashish saha, Mr. Mahmudul Chayan, Ms Jawshan Ara, Mr. Habibur Rahaman, Mrs. Uzma Binte Haidary, Mr. Tahmid Sami

Rahman Nafi, Mr. Amit Kumar Kundu, Ms. Sayma Nowshin Chowdhury, and Mr. Turash Haque Pial. I hope you all enjoy your life to the fullest.

Most importantly, I want to thank my family, my mother Mrs. Monija Islam, and father H.M Sirajul Islam for their sacrifice, support, and unconditional love; my younger sister Mrs. Tahmina Islam for her support and taking care of our parents in my absence; my beloved wife Mrs. Zajeba Tabashsum to help me emotionally and stay with me in all the good/bad times; my mother-in-law Mrs. Nasima Aktar for her excellent suggestions; my brother-in-law Mr. A N A Mushabbir for his lively discussion with me, and my late father-in-law Md. Asadullah.

Above all, I would like to thank my wife for her immense support to complete my Ph.D. and keep me sane over the past few months. But most of all, thank you for being my best friend. I wish to have a lot of memorable moments together in our future days.

Table of Contents

Acknowledgements.....	iii
Table of Contents.....	v
Chapter 1. Introduction.....	1
Chapter 2. Computational Methods.....	7
2.1. Density Functional Theory (DFT) Calculations.....	7
2.2. Proton Site identification.....	7
2.3. Energy of Hydrogen Insertion.....	8
2.4. Nudge elastic band calculations.....	9
Chapter 3. First-Principles Computational Design and Discovery of Novel Double-Perovskite Proton Conductors.....	10
3.1. Introduction.....	10
3.2. Methods.....	11
3.3. Results.....	12
3.4. Discussion and conclusion.....	26
Chapter 4. A Computation Study of Fast Proton Diffusion in Brownmillerite $\text{Sr}_2\text{Co}_2\text{O}_5$	28
4.1. Introduction.....	28
4.2. Methods.....	29
4.3. Results.....	30
4.4. Discussion.....	40
Chapter 5. First-Principles Computational Design and Discovery of Solid-Oxide Proton Conductors.....	45
5.1. Introduction.....	45
5.2. Methods.....	46
5.3. Results.....	49
5.4. Discussion and Conclusions.....	63
Chapter 6. Conclusions and Future Work.....	65
6.1. Conclusions.....	65
6.2. Future work.....	67
Publications.....	68
Appendices.....	69
Appendix A.....	69
Appendix B.....	86
Appendix C.....	94
Bibliography.....	99

Chapter 1. Introduction[†]

Fast proton conductor materials are essential components in hydrogen-based energy devices, including proton-conducting solid oxide fuel cells (SOFCs), solid oxide electrolyzer cells (SOECs), and hydrogen gas separation membranes.¹⁻⁸ Recently, proton-conducting materials have been utilized for novel electronic devices, such as switchable optical devices, proton-gated transistors, and synaptic transistors for neuromorphic computing, opening new opportunities for next-generation computing.^{9,10,19-23,11-18} For SOFC/SOEC energy devices, increasing proton conduction in electrolyte membranes and electrode materials can increase the power output,²⁴⁻²⁷ lower the operational temperature, and improve their efficiency.²⁸⁻³³ Current state-of-the-art proton conducting oxide materials are largely reported in a small number of materials systems, such as perovskite, brownmillerite, and Ruddlesden-Popper.³⁴⁻⁴¹ However, only a small number of these materials, for example, Y-doped BaZrO₃ and other substituted variant compositions, simultaneously exhibit the required high ionic conductivity and good stabilities for the application in these energy devices⁴²⁻⁴⁶. These requirements on multiple materials properties greatly limit the available choices of materials for different applications. Therefore, there is significant interest in developing new solid-state ceramic materials that can exhibit high proton conduction and meet other required properties such as stabilities.

[†] Some text of introduction is adapted from my published papers:

Islam, M. S.; Wang, S.; Nolan, A. M.; Mo, Y., “First-Principles Computational Design and Discovery of Novel Double-Perovskite Proton Conductors”, *Chem. Mater.* (2021).

Islam, M. S.; Nolan, A. M.; Wang, S.; Bai, Q.; Mo, Y. “A Computational Study of Fast Proton Diffusion in Brownmillerite Sr₂Co₂O₅”, *Chem. Mater.* 32 (2020) (12), 5028–5035.

Islam, M. S.; Wang, S.; Alex T. Hall; Mo, Y., “First-Principles Computational Design and Discovery of Solid-Oxide Proton Conductors”, In preparation, 2022.

To achieve high proton conductivities, these proton-conductor materials should have the capability to incorporate a high concentration of protons while maintaining a low energy barrier of proton migration. However, it has been challenging to simultaneously achieve low migration energy barrier and high proton incorporation. Current state-of-the-art perovskites proton conductors ABO_3 (A-site = Sr^{2+} , Ba^{2+} , B-site = Zr^{4+} , Ce^{4+} , etc.) are substituted with aliovalent cations of Y^{3+} , Gd^{3+} , or Yb^{3+} to create oxygen vacancies, which facilitate the incorporation of protons through the dissociative adsorption of water.^{3,47-55} In this proton-incorporation mechanism, the incorporated proton concentration is often limited to 0.2 H/f.u. by the dopant concentrations and oxygen vacancy concentrations that can be achieved in the crystal structures. While the aliovalent dopants facilitate the incorporation of protons, the dopant cations trap protons near them, leading to increased energy barriers for proton migration in the crystal structures, as shown in the experimental and computation studies.⁵⁵⁻⁶¹ This proton trapping effect holds for a wide range of perovskite compositions, irrespective of acceptor dopants, increasing the energy barriers for proton migration.^{55-57,60-65} Therefore, in the development of proton conductor materials, a key challenge is to simultaneously achieve a large amount of hydrogen incorporation and low energy barrier of proton migration.⁶⁶⁻⁷⁰

Perovskite materials without aliovalent cation substitutions or dopants are reported with the capability to absorb a larger number of protons than the aliovalent-substituted perovskites. For example, $SmNiO_3$ and $SrRuO_3$ perovskites are reported to absorb up to one hydrogen per formula unit without extrinsic dopant, thanks to the multivalent cations Ni^{+2}/Ni^{+3} and Ru^{+3}/Ru^{+4} , respectively.^{71,72} This high proton

concentration allows the SmNiO₃ material to achieve a high proton conductivity of 1 mS/cm at a significantly lower temperature range (300°C) without dopants.^{41,71,72} High proton concentrations and the lack of proton trapping effects by acceptor-dopant enable high proton conductivities. Therefore, a promising direction for developing fast proton conductors is to discover and design materials with multivalent cations that can incorporate a high concentration of protons.

In addition to having a high proton concentration, a good proton conductor require low energy barriers for proton migration. Different cations in the crystal structures of oxides are known to significantly affect the energy barriers of proton migration. For example, computational studies reported different proton migration energy barriers of 0.27 eV, 0.41 eV, and 0.54 eV in BaZrO₃, BaHfO₃, and BaCeO₃, respectively.^{68,73–75} In addition, perovskites with multiple cations mixed on either A-site or B-site are shown good proton-conducting properties.^{76–80} Ding et al. reported the mixed-cation perovskite PrCo_{0.5}Ni_{0.5}O_{3-δ} with low activation energy barriers and high proton conductivity.⁶⁶ Among these mixed cation perovskites, double perovskites A₂B'B''O₆ with two types of B-site cations arranged in an ordered form are very promising. The double perovskites Sr₂MMoO₆ (M = Co, Ni, Mn, and Mg) are reported as good proton conductor materials for SOFC.^{81,82} Therefore, to guide the discovery of new perovskite proton conductors, it is important to understand how different cations and their mixture influence the proton diffusion in oxide materials.

Beyond perovskite materials, several other types of structures were developed as proton conductors such as the oxygen-deficient cubic perovskite Ba₂CeZnO₅, the Ruddlesden-Popper perovskite Ca₃Ru₂O₇, and brownmillerite BaInO_{2.5}.^{52,83–90}

Recently, Yu and co-workers demonstrated that brownmillerite $\text{Sr}_2\text{Co}_2\text{O}_5$ (SCO) could form a highly hydronated stable phase,^{41,91} $\text{HSrCoO}_{2.5}$ (HSCO), which has a high proton concentration of one H per formula unit of SCO without extrinsic cation doping. In addition, HSCO exhibits an exceptionally high proton conductivity of $0.33 \text{ S}\cdot\text{cm}^{-1}$ and a low activation barrier of 0.27 eV at 40 – 140 °C, which is superior to typical perovskite oxide proton conductors. The high proton conductivity observed in the HSCO structure has not been fully understood.⁹¹ Further investigation is needed to reveal why this protonated brownmillerite-structured compound can achieve much faster protonic conduction without extrinsic dopants compared to typical perovskite proton conductors. This structural dependence of proton conduction requires the understanding of how different crystal structural units such as cation-oxygen polyhedra influence proton diffusion. For example, in the brownmillerite $\text{Sr}_2\text{Co}_2\text{O}_5$, the layers of CoO_4 tetrahedra layers have a higher proton migration energy barrier than the CoO_6 octahedra layers.^{70,91} High proton migration energy barriers around GaO_4 tetrahedra are reported in the $\text{La}_{1-x}\text{Ba}_{1+x}\text{GaO}_{4-x/2}$ structure.⁹² A study and understanding of how different types of polyhedra influence proton conduction in the crystal structure may help guide the design of proton conductors.

In addition to proton diffusion properties, the stabilities of proton conductor materials are critical for their applications, such as in membranes and SOFC/SOEC devices. Good phase stability after protonation and good stability with water in the operational environment of these devices are required. The presence of certain cations in the material's composition enables better water stability. For example, BaCeO_3 exposed to boiled water decomposes into $\text{Ba}(\text{OH})_2$ and CeO_2 , while BaZrO_3 remains

stable in the same environment.⁹³ Doping Zr in BaCeO₃ improves its water stability.^{35,46} Similarly, Ding et al. demonstrated that substitution of Ni in PrCoO₃ could significantly improve water stability in the obtained PrNi_{0.5}Co_{0.5}O₃ composition.⁶⁶ To design proton-conducting oxides with good water stability, it is important to understand how different cations and compositions affect water stability in oxide materials.

First-principles computation is a powerful research approach to acquire a fundamental understanding of materials and has been demonstrated in studying and designing materials for a wide range of applications, including batteries, fuel-cells, catalysts, photovoltaics, thermoelectric, and semiconductors.^{53,58,98–107,59,108–117,61,118–122,70,75,94–97} First-principles computation are performed to study proton diffusion mechanisms, including proton sites, proton migration pathways and energy barriers, and the effect of dopant on proton migration, in a range of oxide materials.^{53,58,113–121,59,61,70,101,107,110–112} In addition, high-throughput computation analyses and materials screening enable the analyses of the structure-property relationship over a wide range of materials space of different cations, anions, compositions, structures, etc., providing general understanding and guiding principles.^{95,96,109,123,97–100,102,103,106,108}

In this thesis, I perform a systematic first-principles computation study to investigate a wide range of oxide materials, to understand the role of cations, compositions, and structures on the properties, such as proton diffusion, hydrogen incorporation, and water stability, and to identify new proton conductor materials. I provide an overview of first-principles computation methods in Chapter 2. I investigate the effects of different cations and their combinations on proton diffusion and hydrogen incorporation in a wide range of perovskite and double-perovskite materials (Chapter

3). I study the atomistic mechanisms of proton diffusion in brownmillerite $\text{Sr}_2\text{Co}_2\text{O}_5$ structure (Chapter 4). I systematically investigate a large number of oxide materials to reveal the effects of cations, compositions, and structures on properties such as water stability and proton incorporation, then predict a number of novel oxide systems for proton conductors (Chapter 5). In chapter 6, I present the conclusions of the dissertation and potential future research work.

Chapter 2. Computational Methods[‡]

In this chapter, I discuss the computational methods used in this study to predict proton conductor material's properties such as proton migration path, proton migration energy barrier, chemical stability, and proton site energetics.^{65,68,120,124–127}

2.1. Density Functional Theory (DFT) Calculations

All density functional theory (DFT) calculations were performed using the Perdew–Burke–Ernzerhof (PBE)¹²⁸ generalized gradient approximation (GGA) functional in Vienna Ab initio Simulation Package (VASP)¹²⁹. The static relaxations and energy calculations of structures were performed using a force cutoff of 0.02 eV/Å and a plane-wave cutoff of 520 eV consistent with parameters used by the *Materials Project*.¹³⁰ The pseudopotential used were consistent with the *Materials Project*.¹³⁰ A Γ -centered $1 \times 2 \times 2$ k-point grid with grid density of 1000 points per atom was used to sample the Brillouin zone.

2.2. Proton Site identification

The proton sites in the oxide structures were identified by evaluating and comparing possible proton positions around oxygen (O). As protons typically bond to O with a O-H bond length of ~ 1 Å,^{3,4} 32 positions for candidate proton sites were generated with a distance of 1 Å around each symmetrically distinctive O site. For each candidate site, a supercell model with one hydrogen inserted into the generated

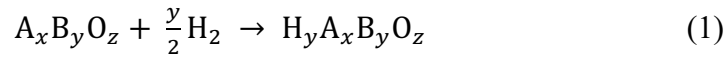
[‡] Part of this chapter has been published in **Islam, M. S.**; Wang, S.; Nolan, A. M.; Mo, Y., “First-Principles Computational Design and Discovery of Novel Double-Perovskite Proton Conductors”, *Chem. Mater.* (2021).

positions was statically relaxed in DFT calculations until the proton relaxed into a local equilibrium position. This process was repeated for all 32 positions and identified a number of proton sites with local minimum energies around each oxygen site. The procedure was performed on each distinctive oxygen site to identify all the distinct proton sites in the perovskite structure.

For identifying the minimum energy structure including proton, 100 protonated structures were generated for each composition from the identified proton sites using the same scheme as in previous studies.^{70,95,99} For each of the composition materials, 10000 distinctive configurations of protonated structures were generated by randomly sampling and placing the appropriate amount of protons from all the identified proton sites in the structure using *pymatgen*.¹³¹ Among these structures, 100 lowest electrostatic Ewald energy structures were selected for further structural relaxation in DFT calculation, and eventually, the lowest energy structure was identified.^{130,131}

2.3. Energy of Hydrogen Insertion

The hydrogen insertion energy, i.e., the reaction energy $\Delta E_{\text{hydrogen}}$ for forming $\text{H}_y\text{A}_x\text{B}_y\text{O}_z$, was evaluated according to the reaction



The reaction energy $\Delta E_{\text{hydrogen}}$ for a given amount y of hydrogen insertion was calculated as

$$\Delta E_{\text{hydrogen}} = \frac{E(\text{H}_y\text{A}_x\text{B}_y\text{O}_z) - E(\text{A}_x\text{B}_y\text{O}_z) - y E_{\text{H}}}{y} \quad (2)$$

where $E (A_x B_y O_z)$ and $E (H_y A_x B_y O_z)$ are the energies of the structures before and after hydrogen insertion, respectively. E_H is the energy of hydrogen calculated as $0.5 E_{H_2O} - 0.25 E_{O_2}$, where E_{O_2} is the energy of oxygen fitted by Wang et al.¹³²

2.4. Nudge elastic band calculations

Nudged-elastic-band (NEB) calculations were performed to determine the minimum energy path and the energy profile for the proton migration between proton sites.^{65,68,133} The initial migration path was constructed by placing images linearly interpolated between the initial and final states of statically relaxed proton configurations. Atomic positions in final NEB images were optimized until the residual forces were less than 0.02 eV/\AA with an energy convergence of 10^{-9} eV/atom . The migration energy barrier (E_a) was calculated as the energy difference between the highest and lowest energies from the converged migration pathway.

Chapter 3. First-Principles Computational Design and Discovery of Novel Double-Perovskite Proton Conductors[§]

3.1. Introduction

First principles computation is a powerful approach to study proton diffusion mechanism in these oxide materials including proton sites, proton migration pathways and energy barriers, and the effect of dopant on proton migration.^{53,58,116–121,59,61,110–115} In this chapter, we aim to understand how different cations and their combinations affect hydrogen incorporation and proton migration, in order to guide the development of mixed-cation perovskites as proton conductors. We perform first-principles computation to systematically investigate proton incorporation and proton diffusion in a wide range of perovskites ABO_3 and double perovskites $A_2B'B''O_6$, and establish guiding principles for selecting cations for perovskite proton conductors. We observe that lower barrier of proton migration can be achieved with a lower oxidation state and ionic radii of B-cation in perovskites. By studying the effect of B-cation ordering, we find that the double perovskites with layered B-site ordering can simultaneously achieve high proton incorporation and fast proton diffusion without a proton trapping effect. Following this materials design strategy, we perform high-throughput computation to generate a few hundred of candidate double-perovskite materials and

[§] This chapter has been published in **Islam, M. S.**; Wang, S.; Nolan, A. M.; Mo, Y., “First-Principles Computational Design and Discovery of Novel Double-Perovskite Proton Conductors”, *Chem. Mater.* (2021).

discover several layered double perovskite materials as good proton conductors with good proton incorporation and fast proton diffusion. The results provide design principles for perovskite proton conductors and offer new research directions for exploring novel double perovskite proton conductors in novel energy and electronic devices.

3.2. Methods

3.2.1. Selection of perovskite material structure

Perovskite oxides with structures in the $Pm-3m$ space group with phase stabilities of energy above hull (E_{hull}) less than 100 meV/atom were selected from the *Material Project* database.^{130,134,135} The materials list is provided in Table A.3. The thermodynamic phase stability of a structure was quantified by the energy above hull (E_{hull}), which was evaluated from the energy convex hull of the energy of all the compounds in the compositional space obtained the *Materials Project* database.^{130,134,135} The double perovskite $A_2B'B''O_6$ with $Fm-3m$ space group and rock-salt B-site cation ordering were taken from *Materials Project* database (Supporting Information). Then we rearranged the B-site cation to generate a double perovskite structure with a layered B-site ordering.

The new candidate double perovskite structures were generated by substituting half of the B-site element of $2 \times 2 \times 2$ -unit cell ABO_3 cubic perovskite structures of space group $Pm-3m$. The combination of B-site cations ($B' = Ag^{1+}, Al^{3+}, Bi^{3+}, Cd^{2+}, Ce^{3+}, Co^{2+}/Co^{3+}, Cr^{3+}, Cu^+/Cu^{2+}, Dy^{3+}, Er^{3+}, Fe^{2+}/Fe^{3+}, Ga^{3+}, Hg^+, Ho^{3+}, In^{3+}, La^{3+}, Lu^{3+}, Mg^{2+}, Nd^{3+}, Ni^{2+}/Ni^{3+}, Pd^{3+}, Pr^{3+}, Sc^{3+}, Sm^{3+}, Tb^{3+}, Tm^{3+}, V^{3+}, Y^{3+}, Yb^{3+}, Zn^{2+}$

and $B'' = \text{Ce}^{4+}, \text{Ge}^{4+}, \text{Hf}^{4+}, \text{Ir}^{3+}/\text{Ir}^{4+}, \text{Mn}^{3+}/\text{Mn}^{4+}, \text{Mo}^{4+}/\text{Mo}^{5+}/\text{Mo}^{6+}, \text{Nb}^{5+}, \text{Pb}^{4+}, \text{Re}^{4+}, \text{Ru}^{3+}/\text{Ru}^{4+}, \text{Sn}^{4+}, \text{Ta}^{5+}, \text{Te}^{4+}, \text{Ti}^{4+}, \text{W}^{4+}/\text{W}^{5+}/\text{W}^{6+}, \text{Zr}^{4+}$) were chosen such a way that the resultant material compositions were charge neutral after hydrogen incorporation. The A-site cation was Ba and Sr (Supporting Information). The candidate double perovskite materials were statically relaxed in the DFT calculation to achieve the lowest energy structure.

3.3. Results

3.3.1. Proton Site and Migration in Perovskites

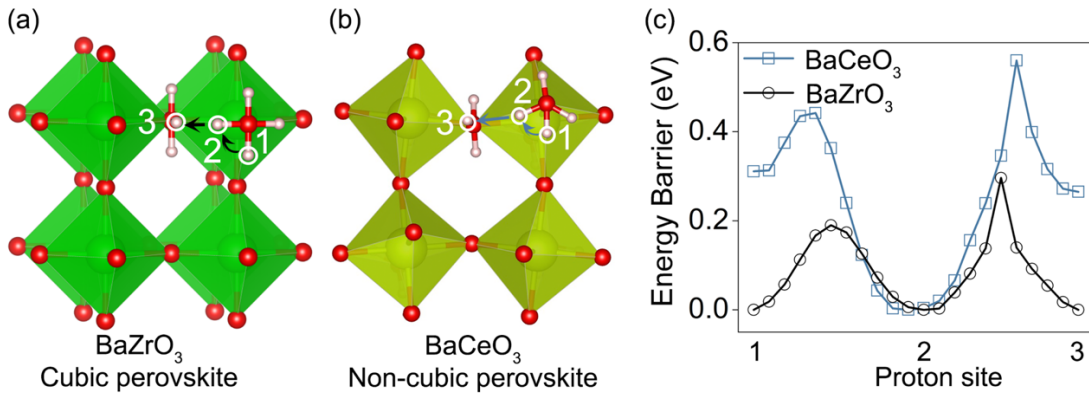


Figure 3.1. Proton site locations (white sphere) and proton migration paths (arrow) in (a) cubic and (b) orthorhombic perovskite structures. (c) The proton migration energy profile of proton rotation (site 1 to 2) and proton jump (site 2 to 3) mechanisms in the perovskite structures of (a) and (b).

Using first-principles computation, we identify the proton sites, site energies, and proton migration barriers in different perovskite phases, using the cubic BaZrO₃ and orthorhombic BaCeO₃ as model systems. In the ABO₃ perovskite crystal structure, the A-site cation is coordinated with oxygen anions to form a 12-fold cuboctahedron,

and the B-site cation is coordinated with oxygen anions to form a BO_6 octahedron.^{136,137} Protons in the perovskites bond with the nearest-neighbor oxygen anion with a bond length of approximately 1 Å (O-H) and a hydrogen bond (O--H) with the next nearest neighbor oxygen (Figure 3.1a,b). In the cubic perovskite structure (e.g. BaZrO_3), all the proton sites have identical surrounding environments of anion and cation (Figure 3.1a) and thus have identical site energies (Figure 3.1c). The same proton site energies are also observed in other cubic perovskites such as BaTiO_3 and SrTiO_3 , suggesting easy proton migration in the crystal structure.^{57,138} Proton migrates among these sites bonded to oxygens through jump (site 2 to 3) and rotation (site 1 to 2) (Figure 3.1a,b). In general, the proton jump has a higher energy barrier than rotation (Figure 3.1c), because the O-H covalent bond is broken and reformed during jumping, while only the weaker hydrogen bond is broken during rotation.^{4,139} Therefore, the proton jump is the rate-limiting step for proton migration in the perovskite materials. Our results for proton site energies and proton migration energy profiles are in agreement with other reported values in cubic perovskite materials.^{55,57,140,141}

In comparison, non-cubic orthorhombic or tetragonal perovskite structures such as BaCeO_3 (Figure 3.1b) have reduced symmetry compared to the cubic perovskite. As a result, proton sites have different site energies (Figure 3.1c) due to different anionic or cationic distribution compared to cubic perovskites (Figure A.1). This different site energies are reported in other non-cubic perovskites SrCeO_3 , SrZrO_3 , BaZrS_3 and SrZrS_3 .^{73,113,138,142} The energy difference among proton sites adds to the migration energy barrier in the proton migration process, as shown in the orthorhombic BaCeO_3 (Figure 3.1c) and SrCeO_3 (Table A.1). In agreement with other reported results,^{73,143–}

¹⁴⁷ non-cubic perovskite structures have higher energy barriers for proton migration. Therefore, cubic-structured perovskites are desired crystal structure for fast proton conductors.^{3,148}

3.3.2. Factors Governing Proton Diffusion in Perovskite

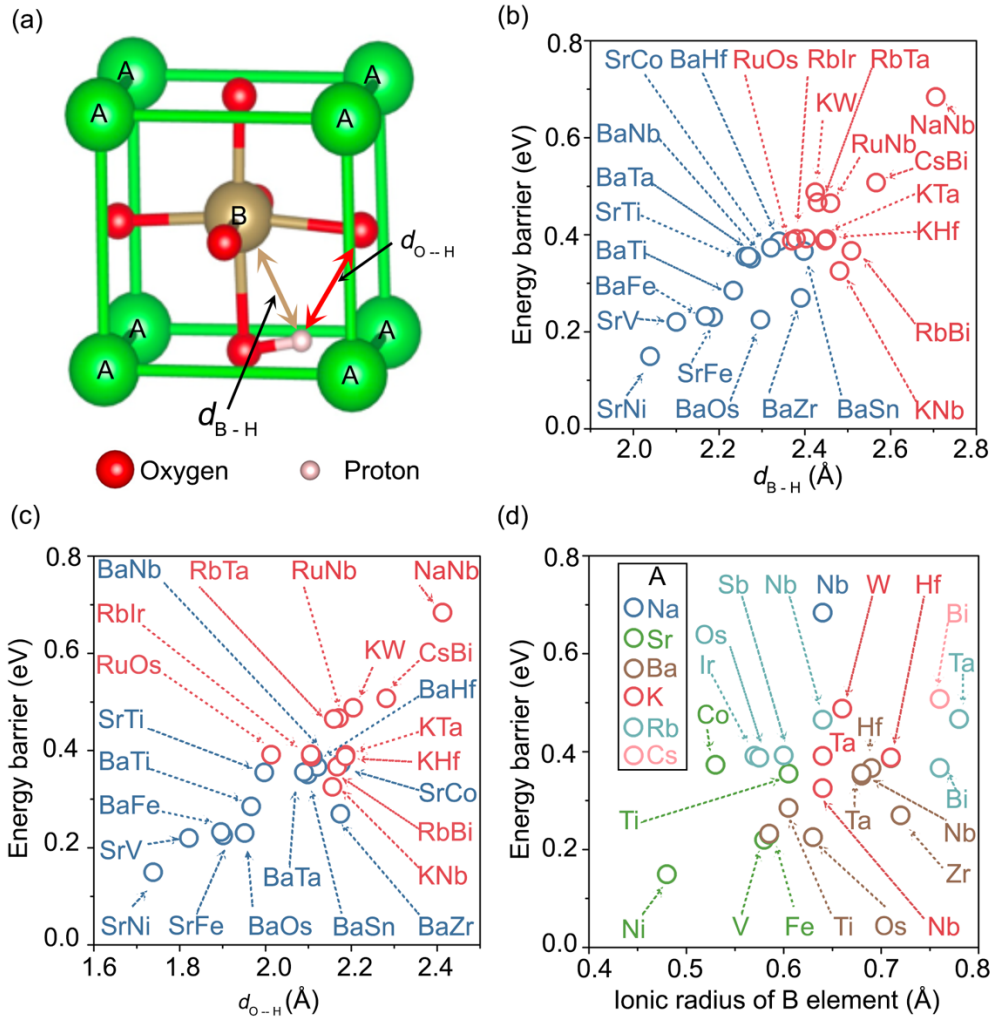


Figure 3.2. (a) Atomic structure of cubic ABO_3 perovskite showing the distance from proton and the nearest B-site cation (d_{B-H}) and the O--H hydrogen bond length between proton and the second nearest oxygen in the BO_6 octahedron (d_{O-H}) of the optimized equilibrium structure. The energy barrier of proton jump as a function of (b) d_{B-H} and (c) d_{O-H} for different ABO_3 perovskites. The legends in (b) and (c) are the cations AB of ABO_3 compositions, and the B-site cations with oxidation state 4 and 5 are marked in blue and red, respectively. (d) The energy barriers of proton jump as a function of ionic radius of B-site cation (marker text) in perovskite compositions with different A-site cations (shown in different colors and legend).

Here we aim to understand the factors that affect the proton migration in order to guide the development of perovskite oxide conductors with different cations. Previous studies suggest that proton migration barrier linearly increase with the increment of dopant ionic radius in doped BaZrO₃, and the distance of oxygen-to-oxygen was also proposed as a descriptor for proton jump migration barrier in BaCeO₃, BaZrO₃, BaTiO₃.^{76,110,125} In this chapter, we performed a systematic study on a larger material list of all known cubic-phase perovskites over a wide range of materials parameters. We calculated the energy barrier of a proton jump in all known cubic-phase perovskite compounds with different cation combinations from the *Materials Project* (Table A.4), and correlated the energy barrier of the proton jump to different structural parameters such as ionic radius, lattice parameter, Goldschmidt factor, octahedral distortion, bond length, and electronegativity (Figure A.2).¹⁴⁹ We find that the energy barrier of the proton jump is correlated with the oxidation state of the B-site cation, ionic radius of the B-site cation, the H--O hydrogen bond length from proton to the second nearest oxygen the BO₆ octahedron (d_{O-H}) and the distance from the proton to the nearest B-site cation (d_{B-H}) of the optimized equilibrium structures (Figure 3.2). The perovskites with B-site cations with lower oxidation state, such as Fe²⁺/Fe³⁺/Fe⁴⁺, Ni²⁺/Ni³⁺/Ni⁴⁺ and Co²⁺/Co³⁺/Co⁴⁺, show lower proton migration energies than the perovskites with higher oxidation state elements such as Ta⁵⁺, Nb⁵⁺, Bi⁵⁺, and W⁵⁺ (Figure 3.2b). The perovskites with B-site cations with lower oxidation states in general show lower proton migration barriers. The B-site cations with higher oxidation states repel the proton, which also increases the d_{B-H} . Similarly, a larger radius of the B-site cation may also increase the distance between B and H. In general, a larger B-H

distance $d_{\text{B-H}}$ is correlated with higher proton migration barrier (Figure 3.2b). We further observe a short hydrogen bond length $d_{\text{O-H}}$ reduces the energy barrier as shown in Figure 3.2c. In summary, B-site cation with a lower oxidation state and smaller radius resulting a shorter distance to proton generally lead to a lower proton jump barrier in cubic perovskite materials, which can guide the selection of B-site cations of perovskite proton conductors.

3.3.3. Proton Incorporation in Perovskite

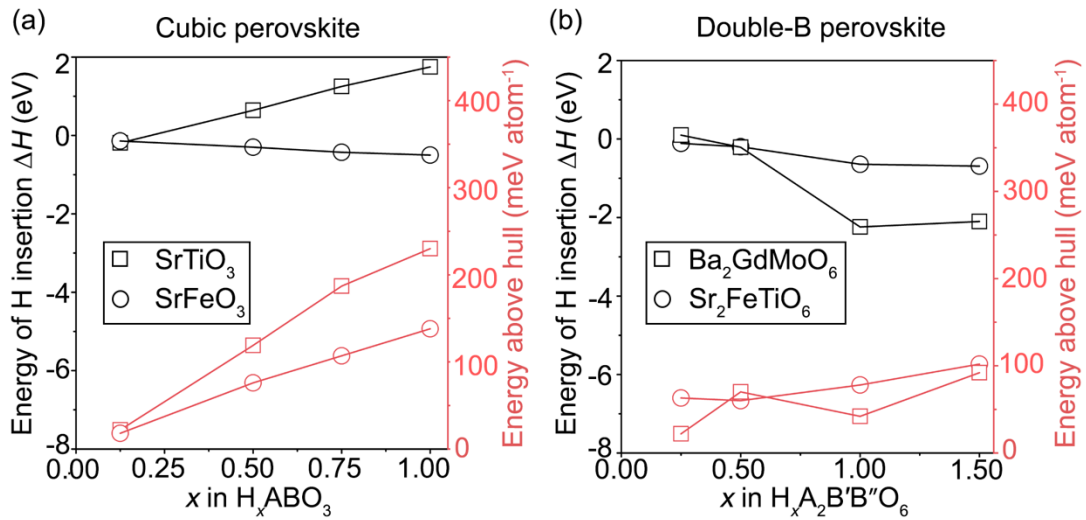


Figure 3.3. Energy of hydrogen insertion (ΔH) (black lines and left y-axis) and energy above hull (red lines and right y-axis) of (a) H_xABO_3 cubic perovskite, SrTiO_3 and SrFeO_3 , and (b) $\text{H}_xA_2\text{B}'\text{B}''\text{O}_6$ double-B perovskite $\text{Ba}_2\text{GdMoO}_6$ and $\text{Sr}_2\text{FeTiO}_6$ as a function of H concentration x .

To evaluate and compare the materials capability to absorb hydrogen, we calculated the hydrogen insertion energy for different hydrogen concentrations (0.125, 0.5, 0.75, 1.0 H/f.u.) in the perovskite materials (Methods). The relation of our

hydrogen insertion energy to the hydration energy to incorporate hydrogen through the dissociation of water is explained and analyzed in the Supplementary Information. Perovskites with the same structure but different cations, such as SrFeO₃ and SrTiO₃, show different capabilities for proton incorporation. Using static DFT energy of H₂ molecules as the reference (Methods), SrFeO₃ has a negative energy of hydrogen incorporation (ΔH) to form H_xSrFeO₃ as hydrogen content x increases up to 1 H/f.u. (Figure 3.3a), suggesting favorable hydrogen insertion. In contrast, the insertion of hydrogen into SrTiO₃ to form H_xSrTiO₃ is endothermic, corresponding to a positive increase in hydrogen incorporation energy ΔH with increasing proton concentration x (Figure 3.3a). Our computation results are in agreement with previous experiments that undoped SrFeO₃ is a proton conductor and that SrTiO₃ needs acceptor doping (e.g. Y, Sc) to exhibit proton conductivity.^{150–152} Similar to SrFeO₃, we also observe that perovskites with multivalent B-cations including BaFeO₃, SrVO₃, RbBiO₃ and SrCoO₃ exhibit similar trends in incorporating hydrogen (Table A.5), suggesting these materials are able to incorporate hydrogen without dopants. Therefore, as identified in our computation, some of the multi-valent cations have the capability of incorporating hydrogen in perovskites.

As a description of phase stability, we also evaluate the energy above hull (E_{hull}) for perovskites with varying ranges of incorporated hydrogen. E_{hull} is defined as the energy difference of the phase to the thermodynamic equilibria phase combinations.^{96,135} However, the phase stabilities of H_xSrFeO₃ and H_xSrTiO₃ decrease (E_{hull} increases) as x increases (Figure 3.3a), in agreement with the experimental observation of the SrFeO₃ decomposition.¹⁵³ We also observe that perovskites with

multivalent B-site cations including BaFeO₃, SrVO₃, and SrCoO₃ exhibit similar trends in decreasing phase stability as a result of hydrogenation (Figure 3.3a), consistent with experimental observation.^{41,69,70,154,155} Compared to these materials, H_xSrTiO₃ has even poorer phase stability with increasing proton content. The phase stability of the materials with incorporated hydrogen is a limiting factor for achieving high hydrogen concentration. A good proton conductor should maintain the phase stability with hydrogen incorporated.

We evaluated the hydrogen incorporation in double perovskites with mixed B-site cations, and found mixtures of B-site cations also led to different hydrogen incorporation. For double perovskite materials such as Ba₂GdMoO₆, proton incorporation is energetically favorable up to 1 H/f.u. (Figure 3.3b) but not further to 1.5 H/f.u., which can be attributed to the valence change of Mo during hydrogen insertion. The double perovskite material Sr₂FeTiO₆ shows favorable protonation at 1 H/f.u. even up to 1.5 H/f.u., which can be attributed to the multi-valent Fe cation (Figure 3.3b). These results suggest that different combinations of cations in double perovskites determine the hydrogen incorporation capability. Similar to single perovskites, the double perovskites show decreasing phase stability as hydrogen concentration increases. The double perovskites such as Ba₂GdMoO₆ and Sr₂FeTiO₆ show better phase stability with 1 H/f.u., compared to single perovskite at the same hydrogen concentration (1 H/f.u.). In our calculation, HBa₂ZrYO₆ shows good phase stability at 1 H/f.u. with reasonable phase stability ($E_{\text{hull}} = 35$ meV/atom, Supporting Information), in agreement with the report that proton conductor Y-doped BaZrO₃ has good stability with incorporated hydrogen.¹⁵⁶ Therefore, double perovskites containing multivalent

cations can incorporate a decent amount of hydrogen while maintaining good materials stability, and these attributes of double perovskites make them promising candidates for proton conductors.

3.2.4. Proton Diffusion in Double Perovskite

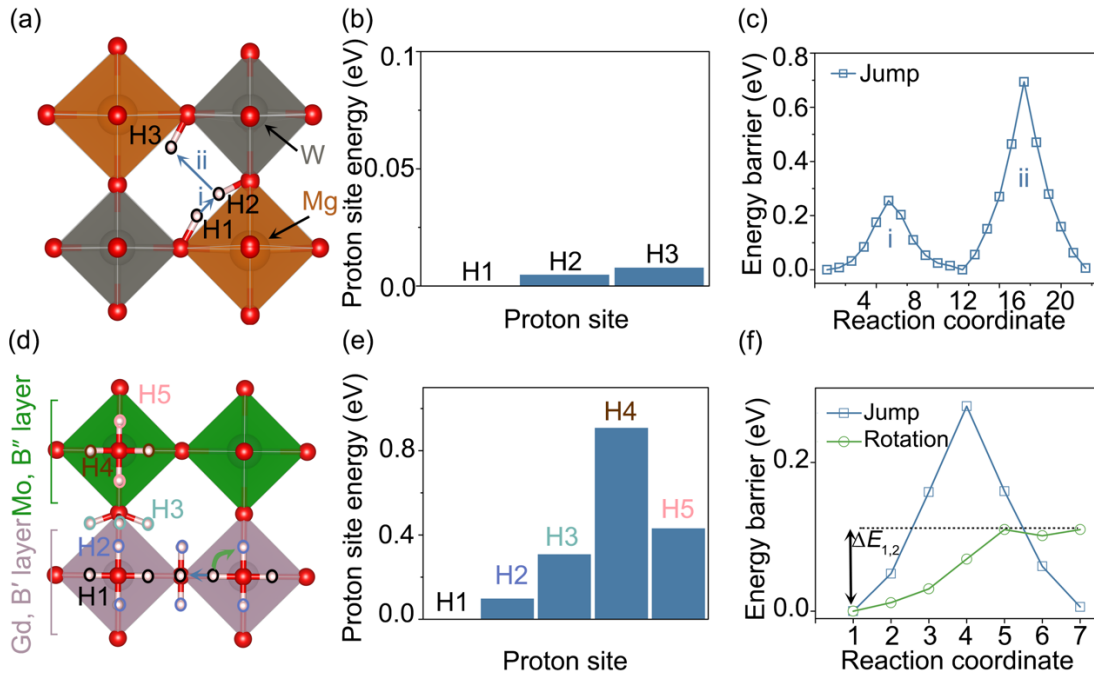


Figure 3.4. Proton migration in double-B perovskites. In double perovskite Ba_2MgWO_6 with B-site rock-salt ordering, (a) proton sites (white sphere) and proton migration pathway (arrow), (b) proton site energies, and (c) migration energy profile. (d) Double perovskite $\text{Ba}_2\text{GdMoO}_6$ with B-site cation layered ordering with (e) proton site energies and (f) migration energy in GdO_6 octahedron layer.

B-site cations in double perovskites generally exhibit either rock-salt or layered ordering.¹⁵⁷ For example, double perovskite Ba_2MgWO_6 has rock-salt B-site cation ordering and $\text{Ba}_2\text{GdMoO}_6$ has layered B-site cation ordering.^{158,159} Using these double

perovskites as model systems, we calculated the proton sites and the proton migration mechanism in the B-site rock-salt and layered ordered double-B perovskites (Figure 3.4). In the rock-salt-ordered double perovskite Ba_2MgWO_6 , the low-energy proton sites locate closer to Mg, the B'-site cation of lower oxidation state, in agreement with our identified trend of B-site cations in single perovskites (Figure 3.4a). These proton sites have identical site energies (Figure 3.4b) but have two proton jump pathways. The proton jump near Mg and within the same MgO_6 octahedron has a low proton jump barrier of 0.25 eV (Figure 3.4c), and the other jump pathway to a different MgO_6 octahedron bypassing W, the B''-site cation of higher oxidation state, has a higher proton jump energy barrier of 0.69 eV (Figure 3.4c). As shown in our calculation results for several rock-salt double-B perovskites (Table A.6), double perovskites with lower oxidation state B-site cations have lower proton jump energy barriers, in agreement with the trend for single perovskites. Since both proton jump pathways are necessary for percolated proton migration in the double perovskite structure, the cations with higher oxidation state limit the overall proton conduction. Therefore, double perovskites with rock-salt B-site ordering have a high overall activation energy for proton diffusion.

In contrast, double perovskites with layered B-site cation ordering form separate layers of $\text{B}'\text{O}_6$ octahedron and of $\text{B}''\text{O}_6$ octahedron (Figure 3.4d). The proton sites (H1 and H2) in the $\text{B}'\text{O}_6$ octahedron layer with lower oxidation state B'-site cation have lower site energies, whereas the proton sites (H4 and H5) in $\text{B}''\text{O}_6$ octahedron layer have higher site energies (Figure 3.4e). For the proton sites (H3) bonded to the oxygen shared by two $\text{B}'\text{O}_6$ and $\text{B}''\text{O}_6$ octahedron, the proton sites are attracted to B'-

site cation with lower oxidation state, due to the lower repulsive forces (Figure 3.4e). In other layered double-B perovskite materials we calculated (Table A.8), proton sites are in the B'O₆ layer to have lower energy.

Because the protons are localized in the low oxidation state B'-site cation B'O₆ octahedron layer, proton jump and rotation (Figure 3.4d) happen within the B'O₆ octahedron layer. In the layered double-B perovskite Ba₂GdMoO₆, the proton jump in the B'O₆ octahedron layer has an energy barrier of 0.27 eV, and proton rotation has an even lower barrier of 0.11 eV (Figure 3.4f). Therefore, in the layered double perovskite, the B'-site cations with lower oxidation state trap the protons and also have low barrier for proton migration, and the B'O₆ octahedron layer provides fast continuous planar proton diffusion, leading to fast overall proton migration in the layered double-B perovskite materials. Similarly, recent computation studies also reported that high concentration of dopant that form a connected layer can form fast proton diffusion pathways in BaZrO₃.^{56,160} The effect of oxygen vacancy on the proton diffusion is analyzed in the Supporting Information, and may require further studies. In summary, our computation proposes double perovskites with layered B-site cation ordering as promising proton conductors that can have both good proton incorporation and fast proton diffusion.

3.4.5. Computation Prediction of New Double Perovskites with Layered B-Site Ordering

In order to discover new double perovskites as proton conductors, I performed computational screening for a wide range of cubic-structured double-B perovskite compositions $\text{HBa}_2\text{B}'\text{B}''\text{O}_6$ for a wide range of B' and B''-site cations in the layered ordering. The candidate $\text{HBa}_2\text{B}'\text{B}''\text{O}_6$ materials are generated to have the B'-site cation with the oxidation state +3 (or multivalence including +3) and the B''-site cation with oxidation state of +4 or +5/+6 (Figure 3.5, data in the Supporting Information). As an exploratory search of new materials, we include some combinations of B-site cations that appear to be not charge balanced, because some double perovskites have B-site cations which exist in non-common oxidation states.^{157,161} Since the phase stability of protonated materials is essential, we use the energy above hull for the materials with 1 H/f.u. to access the phase stability of the predicted candidate materials, as a number of layered double-B perovskite materials show good phase stability with 1 H/f.u. in our calculations (Section 3.2.3). In particular, the double perovskites with B' as group III or lanthanide group elements, and B'' as Ce^{4+} , Hf^{4+} , Pb^{4+} , Sn^{4+} , Ta^{5+} , Ti^{4+} , and Zr^{4+} show decent phase stability with proton incorporation. In addition, some of these B-site cations with lower valence can be beneficial for proton migration.

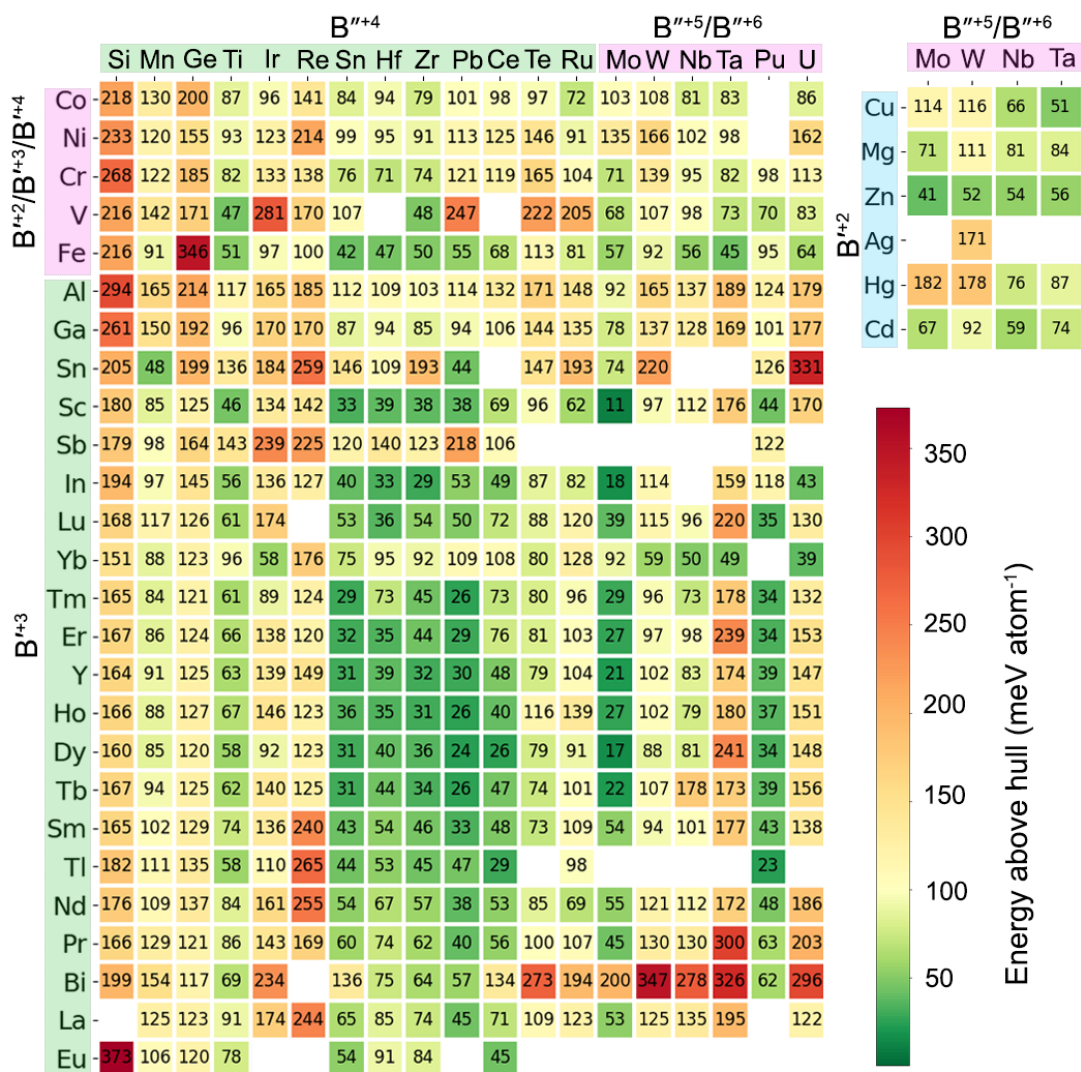


Figure 3.5. The calculated energy above hull E_{hull} (color bar) of layered double-B perovskite $\text{HBa}_2\text{B}'\text{B}''\text{O}_6$ predicted by computation. The cations are arranged in ascending order of ionic radius.

octahedron ($B' = \text{Zn, Sc, In, Lu, Tm, Er, Y, Ho, Dy, Tb}$ and Sm) layer increases as ionic radius of B' increases (Figure 3.6) with the exception of $B'' = \text{Ti}$ and Mo . The trend of low proton migration barrier for smaller B' -site cation in layered double-B perovskite structure is similar to the trend discussed in Section 3.2.2 for single perovskite structure. This trend of fast proton diffusion for smaller B-site cations is a general design principle for fast proton conductors.

In addition, many calculated double-B perovskites in hydrogenated states $\text{HBa}_2\text{B}'\text{B}''\text{O}_6$ energetically prefer layered B-site cation ordering to rock-salt ordering (Figure 3.6). These layered B-site cation ordering in double perovskites is beneficial to achieve low proton migration energy barrier as opposed to rock-salt ordered structure as shown in section 3.2.4. In conclusion, our first-principles computation predicts multiple double-B perovskites with layered B-site cation ordering as potential proton conductors.

3.4. Discussion and conclusion

In this chapter, I employ first-principles computation to systematically analyze the hydrogen incorporation and proton diffusion in a large number of known or predicted perovskite materials including single perovskites and double perovskites with a wide range of B-site cations. The computation study reveals the key descriptors of B-site cation on affecting proton migration.

Some B'' -site cations such as $\text{Ce, Zr, Ta, Hf, Pb, Sn,}$ and Mo in general maintain good phase stability with decent amount of hydrogen incorporated. The layered-

ordered double-B perovskites overcome the proton-trapping effect in current proton conductors, such as Y-doped BaZrO₃, in which the Y dopants trap protons than the Zr cation in the B-site,^{55,56} and increases the proton migration energy.^{55,57,60–64}

While many of the compounds evaluated here are computationally predicted and are to be confirmed in experiments, the results offer useful guidance for the future materials design of perovskite materials for fast proton conduction. For example, the computation shows that dopants such as Y, In, and Sc in combination with Zr or Ce are good B-site cation combinations, consistent with the well-known Y-, In-, or Sc-doped BaZrO₃ and BaCeO₃. In addition, for proton migration, B-site cations with lower valence and smaller radius in general leads to a lower energy barrier for proton jump. Nevertheless, the work greatly broaden the potential materials space of proton conducting perovskite materials, which can motivate further applications in novel electronic computing devices.^{9,10,19–23,11–18} In particular, the newly discovered double perovskite materials are of great potential for future devices relying on proton conducting materials. In summary, the computation results provide systematically understanding and guidance for the ration design of perovskites for proton insertion and diffusion for novel energy and electronic devices.

Chapter 4. A Computation Study of Fast Proton Diffusion in Brownmillerite Sr₂Co₂O₅**

4.1. Introduction

The goal of this thesis is understanding the fundamental mechanisms of proton incorporation and fast proton diffusion in this new brownmillerite SCO material in order to provide insight to the future research and development of novel proton-conducting oxide materials. Computational studies can directly investigate the detailed atomistic mechanism of proton diffusions including the site, bonding, energetics, and hopping of protons in the brownmillerite structure of SCO and HSCO. While computation studies reported the electronic structure of hydronated SCO^{91,162}, the fast proton diffusion in the HSCO structure observed in the experiments has not been fully understood. Further investigation is needed to reveal why this protonated brownmillerite-structured compound can achieve much higher protonic conduction without extrinsic dopants than typical perovskite proton conductors that require a significant amount of aliovalent cation doping.

In this chapter, I perform first-principles computation to investigate the proton diffusion mechanism in brownmillerite SCO and its associated hydronated structures. The calculations identify the site positions and energies of incorporated protons as a function of hydrogen concentration, and evaluate the possible diffusion pathways for fast proton conduction. I find the 1D proton diffusion pathway has a low barrier in the brownmillerite structure with sluggish diffusion across the pyramid layers.

** This chapter has been published in **Islam, M. S.**, Nolan, A. M., Wang, S., Bai, Q., Mo, Y, “A Computational Study of Fast Proton Diffusion in Brownmillerite Sr₂Co₂O₅”, *Chem. Mater.* 32 (2020) 5028–5035.

Furthermore, I explore other selected brownmillerite-structured compounds for potential proton diffusion and compare to perovskite proton conductors. The results provide insights into future design and discovery of fast proton conductors.

4.2. Methods

We used a supercell model with 32 formula units of $\text{SrCoO}_{2.5}$ (SCO) with a size of $15.745 \text{ \AA} \times 11.148 \text{ \AA} \times 10.939 \text{ \AA}$. The calculated lattice parameters from DFT relaxation agrees with experiment (Table B.1).¹⁶³ Similar approach to chapter 2 is performed to identify all the distinct proton sites in the SCO structure (Figure 4.2a).

For the hydronated $\text{H}_x\text{SrCoO}_{2.5}$ (H_xSCO) at higher H concentration $x > 0.03125$, the structures with inserted protons were identified by evaluating a large number of possible configurations of protons in the SCO structure using the same scheme as in previous studies and chapter 2^{95,99}. For each composition of H_xSCO with different H concentration ($x = 0.125$ to 1), similar approach to chapter 2 is performed to find the lowest energy structure was used as the representative structure for each H_xSCO composition.

4.3. Results

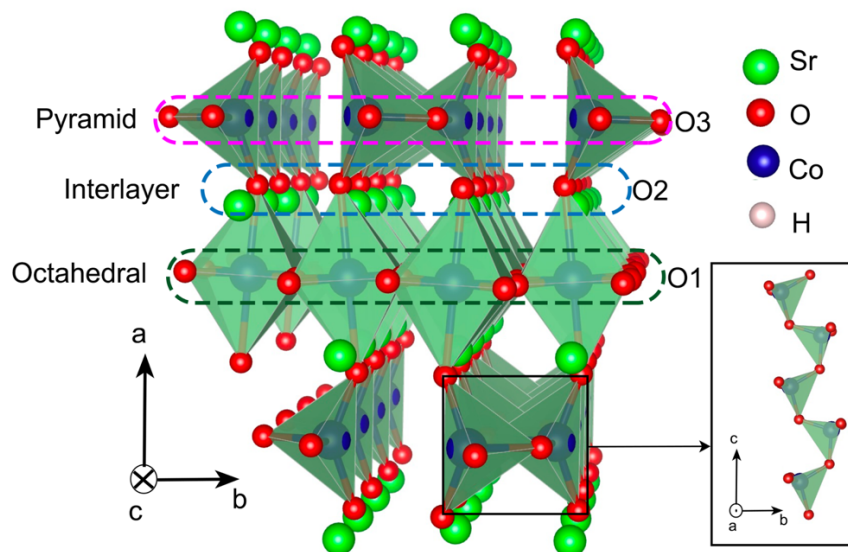


Figure 4.1. SrCoO_{2.5} brownmillerite structure. CoO₆ octahedra are connected into a 2D layer, and CoO₄ pyramids are connected into a 1D chain (top view shown in inset). The oxygen Wyckoff sites O1, O2, and O3 were termed octahedral, interlayer, and pyramid, respectively, according to their local cation environments.

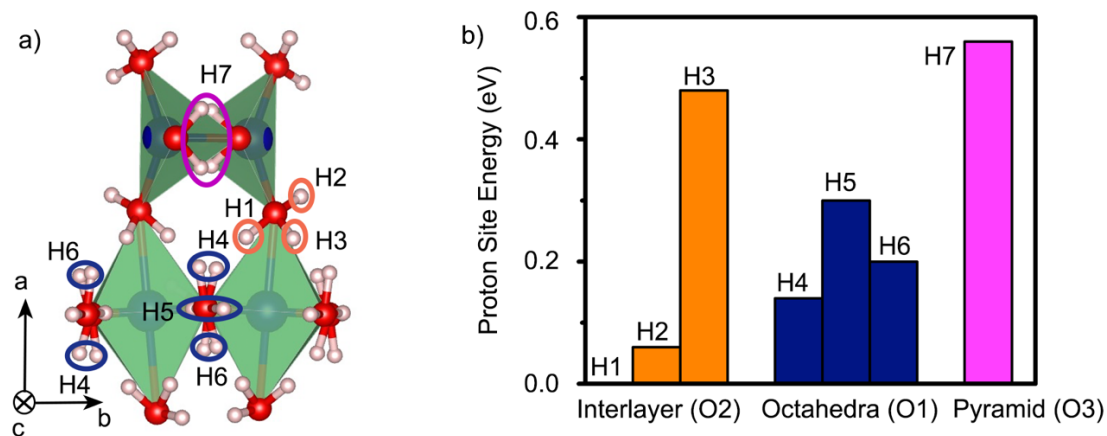


Figure 4.2. Proton sites and energies in SrCoO_{2.5} from first-principles calculations. (a) Positions of proton sites (white sphere). Identical sites are grouped, and colors indicate their corresponding O sites, such as interlayer (orange), octahedral (blue), or pyramid (pink) O sites. (b) Proton site energy referenced to the H1 site with lowest site energy.

4.3.4. Proton sites in the brownmillerite structure

The SCO brownmillerite structure is comprised of alternating layers of CoO_6 octahedra and CoO_4 pyramids (Figure 4.1).^{163,164} The layer of CoO_6 octahedra is packed similarly to that in the perovskite structure, and the layer of CoO_4 pyramids can be considered as a layer of octahedra with one oxygen missing. Every other pyramid layer is separated by an octahedral layer along the a axis and shifted in the b axis direction by one octahedron. Within the pyramid layer, connected oxygen sites form a 1D chain along the c axis. The pyramid and octahedral layers share one oxygen, which is regarded as the interlayer O2 site. The oxygen Wyckoff sites $8c$ O1, $8c$ O2, and $4b$ O3 are named in this chapter as the octahedral layer, interlayer, and pyramid layer oxygen sites, respectively, according to their local coordination environments (Figure 4.1).

The proton sites in the SCO brownmillerite structure were identified by DFT calculations. Similar to the proton in perovskite oxides,^{5,53,165} the protons in brownmillerite bond to an O ion forming a covalent O-H bond with a bond length of approximately 1 Å. Each bond is aligned towards another neighboring oxygen ion forming a hydrogen bond (Figure 4.2a), except for proton site H7 on the pyramid layer oxygen. On each oxygen, there are multiple proton sites with different orientations (Figure 4.2a). Here, we categorize proton sites based on the position of their bonded oxygen as interlayer, octahedral, and pyramid. The calculated low-energy sites (Figure 4.2) in general agree with the previous study (Table B.2), and we have identified additional sites, such as H3 and H5.¹⁶² For a single dilute proton in SCO, the H1 site on the interlayer oxygen has the lowest energy among all proton sites, and the H2 site on the same interlayer oxygen has a slightly higher energy of 0.06 eV. Proton sites H4

and H5 on octahedral O1 oxygens have a higher site energy of 0.14 eV and 0.3 eV respectively, and the H3 site has a significantly higher energy of 0.48 eV. The H7 site on pyramid O3 oxygen has an even higher energy of 0.56 eV. This difference in the strong site preference may be caused by different local bonding environment of oxygen and proton interactions with other cations and oxygen ions.³ For example, the A-site Sr cations may have an effect on the H site energy preferences due to different distances with H sites in different O layers and their electrostatic repulsions with protons (Figure B.2). The effect of Van der Waals interactions on H site energies and site positions was evaluated and found to be small (Supporting Information). According to the predicted proton site energy, protons are expected to occupy the interlayer sites in SCO at low H concentration.

4.3.5. Hydrogen insertion in Brownmillerite.

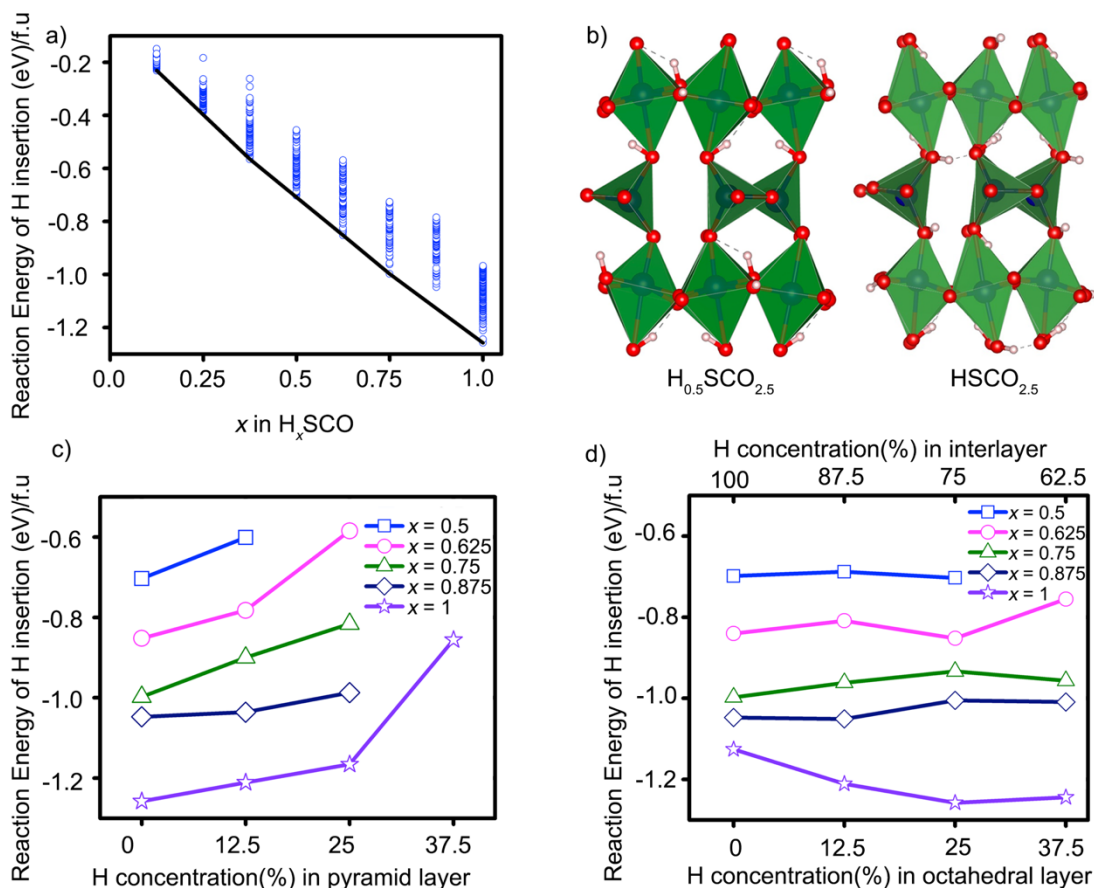


Figure 4.3. The energy and structure of hydrogen insertion in brownmillerite. a) The reaction energy of hydrogen insertion in H_xSCO for different H concentration x . The black line represents the convex hull of the minimum energies from the calculated structures. b) Lowest energy structures of $H_{0.5}SCO$ and $HSCO$. The reaction energy of hydrogen insertion in H_xSCO as a function of H concentration in the c) pyramid layer and d) octahedral layer. Each line represents a different H concentration x in H_xSCO and each point represents the structure with the minimum energy at the given H concentration in the corresponding oxygen layer.

The structures of hydronated H_xSCO at higher H concentrations were generated using the calculated proton sites. The calculated reaction energy of hydrogen insertion in H_xSCO decreases upon an increase of H concentration (Figure 4.3a), suggesting

energetically favorable insertion of hydrogen into SCO at conditions of dilute hydrogen. However, the energy above hull (E_{hull}) of H_xSCO increases with increasing H concentration x to 65 meV/atom for HSCO at $x = 1$. The structural stability of H_xSCO in first-principles calculations is consistent with previous experimental observations of HSCO material.⁹¹ Using Bader charge analysis,¹⁶⁶ we quantified the Bader charge around Co ions in H_xSCO structures at different H concentrations and showed the valence of Co reduces upon H insertion (Figure B.3), in consistent with a prior computation study.¹⁶⁷ Therefore, the multivalence of $\text{Co}^{2+/3+}$ accounts for the charge compensation of hydrogen insertion.

In the H_xSCO structures at high H concentration x , the configuration and energies of the proton sublattice are affected by the energetic preference of proton sites as identified in section 4.3.1. The energies of H_xSCO are investigated by varying the H concentration among different proton sites on the oxygen of octahedral, inter-, and pyramid layers at a given H concentration x (Figure 4.3). For the entire range of H concentration in H_xSCO , increasing proton concentration in the pyramid layer increases the reaction energy (Figure 4.3c). Thus, the proton sites in the pyramid layer are still highly unfavorable in H_xSCO at high H concentration, consistent with proton site preference in SCO with dilute H. Indeed, the pyramid layer is empty of protons in all lowest energy structures across the range of H concentration. At non-dilute H concentration in H_xSCO , the proton sublattice occupies a fraction of octahedral and interlayer sites, as shown by the representative lowest energy structure of H_xSCO at $x = 0.5$ and 1 (Figure 4.3b). To investigate the proton site preferences in H_xSCO at high H concentration x , we varied the H concentration in the interlayer and octahedral layer,

and found that the change in the energy of $H_x\text{SCO}$ (Figure 4.3d) is small for a wide range of H concentrations in these layers. Therefore, in $H_x\text{SCO}$ at high H concentration, protons are distributed among interlayer and octahedral layer sites. This lack of the proton preference among interlayer and octahedral layers in $H_x\text{SCO}$ compared to dilute H in SCO may be caused by the increased H-H interactions and the valence change of the Co cation, which reduce the small site energy difference of less than 0.3 eV between proton sites (H1-H5) in the octahedral layer and interlayer.¹⁶⁷ The small energetic preference of proton sites among interlayer and octahedral layers in $H_x\text{SCO}$ is greatly beneficial for proton transport. In $H_x\text{SCO}$, a significant fraction of proton sites in the octahedral layer and interlayer are available for proton hopping, and small energy changes during the transition of proton sublattice suggest a low energy barrier for proton migration.^{97,108,168,169}

4.3.6 Proton diffusion

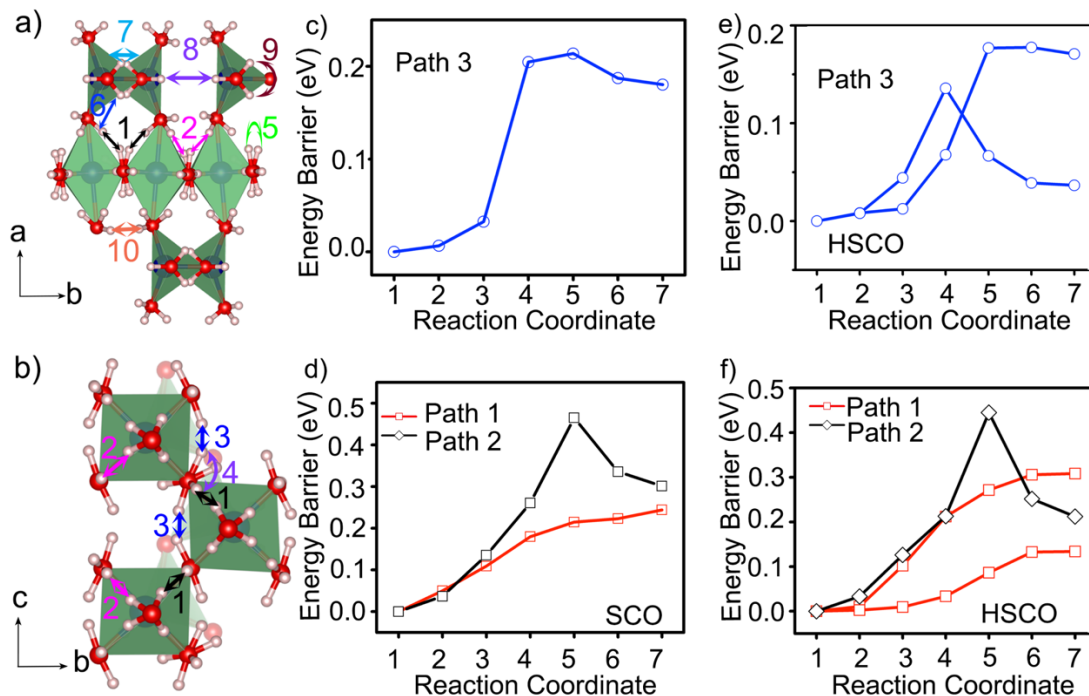


Figure 4.4. Proton migration in the brownmillerite structure. (a, b) The pathways for proton migration marked by arrows. Energy profiles of proton migration within the octahedral layer (path 3) and interlayer to octahedral layer (paths 1 and 2) in (c, d) $\text{SrCoO}_{2.5}$ and (e, f) $\text{HSrCoO}_{2.5}$.

As shown in previous studies,^{4,5,53,168} proton migration in solid oxides, such as perovskites, consists of two elementary steps: a proton jump and a proton rotation. A proton jump is the hop of a proton from one oxygen to another by breaking and reforming the O-H bond, and a proton rotation is the reorientation of the O-H bond on the same oxygen site. For proton transportation to percolate throughout the oxide structure, protons must undergo both jumps and rotations. We used nudged-elastic band (NEB) calculations to investigate proton migration, including jumps and rotations, for a variety of pathways among predicted proton sites in SCO and HSCO (Figure 4.4).

Since the proton sites on pyramid layers have high site energies, proton migration through the pyramid layer is expected to have a high barrier. Indeed, a proton jump to the pyramid layer from the interlayer (path 6 in Figure 4.4) was found to have a high energy barrier of 0.42 – 0.66 eV among all pathways considered (Table B.3). Thus, the pyramid layer may impede the proton diffusion along the *a* direction, consistent with experiments,⁹¹ and confine the proton migration within the 2D planes of the interlayer and octahedral layers.

Given the large number of proton sites in the interlayer and octahedral layers, there are many possible pathways for proton hopping among them (Figure 4.4). We evaluated proton migration along many of these pathways in SCO and HSCO and found most of these pathways have low migration barriers. In particular, the proton jumps along the pathway in the octahedral layer (path 3 in Figure 4.4b) along the *c* axis has an energy barrier of 0.18 eV. For proton jumps between interlayer and octahedral layers, path 1, between H1 and H4 sites, has an energy barrier of 0.21 – 0.25 eV, and path 2, between H2 and H6, has a barrier of 0.4 – 0.46 eV. In addition, the energy barrier of proton rotation (Figure 4.4) is low as 0.13 – 0.26 eV for paths 4 and 5. From the calculated proton barriers, the percolation of proton migration through the SCO brownmillerite structures may consist of the jumps of paths 1 and 3 with rotations of path 4 and 5. Hydrated brownmillerite HSCO exhibits a similar proton migration mechanism and energy barriers, such as 0.13 – 0.3 eV for path 1, 0.37 – 0.49 eV for path 2, and 0.135 – 0.18 eV for path 3 (Figure 4.4). The proton migration energy barriers are similar at other hydrogen concentrations of H_xSCO (*x* = 0.25, 0.5, 0.75). For paths 1, 2 and 3, the energy barriers are in the ranges of 0.17 – 0.3 eV, 0.37 – 0.45

eV and 0.14 – 0.23 eV, respectively (Table B.3). The overall activation energy for H_xSCO , considering this range of proton migration pathways, is in good agreement with the experimental activation energy of 0.27 eV. In addition, we evaluated the local charge on Co cations near the proton, and found that the local charge on Co changes and transfers to other Co during the proton migration (Figure B.4). Given the charge on Co tends to trap protons, preventing them from migrating, this cation charge transfer may facilitate proton jumping between different Co-O polyhedra.^{106,170–172} Therefore, the multivalence of $Co^{2+/3+}$ and this charge transfer alleviate the proton trapping effect observed in aliovalent B-site doped perovskites such as Y-doped $BaZrO_3$. In summary, our calculations reveal fast proton diffusion in SCO and HSCO in between the octahedral layers and interlayers with particularly fast 1D channels along the c axis.

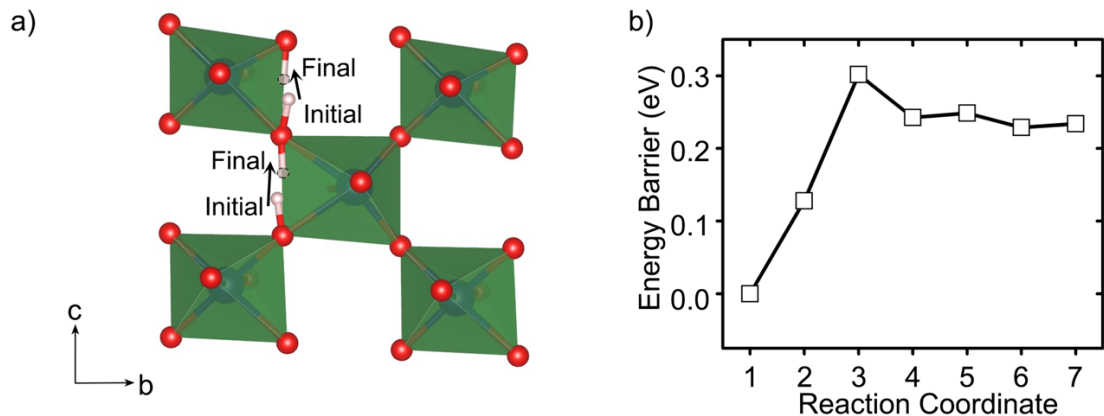


Figure 4.5. a) The pathway of cooperative migration of two protons in HSCO and b) energy profile of the cooperative migration.

We further investigated the cooperative jump of multiple protons, such as Grotthuss mechanism,¹⁷³ in brownmillerite HSCO. From NEB calculations, the cooperative jump of two protons (Figure 4.5) shows a low barrier energy of 0.3 eV.

This low barrier suggests the cooperative migration of protons may be activated for proton transport in brownmillerite $H_x\text{SCO}$. Such low-barrier cooperative proton migration may be explained by the similar energies for a wide range of configurations in the proton sublattice in $H_x\text{SCO}$ as shown in section 4.3.2, suggesting the frustration of the proton sublattice and cooperative transition between these different configurations.^{108,169,174} In summary, our calculations reveal fast proton diffusion in between the octahedral layers and interlayers of SCO and HSCO over a range of H concentrations, with particularly fast 1D channels along the c axis.

4.3.7. New brownmillerite compounds

To understand whether brownmillerite structures are generally good for proton conduction, we evaluated the proton transport in a number of compounds in brownmillerite-structure generated by substituting cations in the A or B sites. First, we investigated $\text{MgCoO}_{2.5}$, $\text{CaCoO}_{2.5}$, and $\text{BaCoO}_{2.5}$ to establish the effect of the A-site cation on proton diffusion. $\text{MgCoO}_{2.5}$ is found to be highly unstable with an E_{hull} of 183 meV/atom, which is reflected by the significant distortion of CoO_6 octahedra in the relaxed structure. This distortion in the CoO_6 octahedra also leads to an anisotropic, higher migration energy barrier for the path 1 proton jump, which is also observed for proton migration in perovskites.^{148,175} In $\text{CaCoO}_{2.5}$, the path 1 proton jump exhibits barriers of 0.22 eV and 0.42 eV. $\text{BaCoO}_{2.5}$ shows a good stability (E_{hull} of 0 eV/atom) and no octahedral distortion but shows a high barrier of 0.5 eV for the path 1 proton jump. Therefore, other A cations do not lead to improvement of proton diffusion in brownmillerite SCO and HSCO.

For brownmillerite structures $\text{SrXO}_{2.5}$ with other B-site cations ($X = \text{Ni}, \text{Cr}, \text{Mn}, \text{Fe}, \text{Ti}$), $\text{SrXO}_{2.5}$ with $X = \text{Ni}, \text{Cr}, \text{Mn}$ show higher energy barriers of 0.39, 0.4, and 0.45 eV (Table B.4), respectively, for the path 1 proton jump. By contrast, $\text{SrXO}_{2.5}$ with $X = \text{Fe}, \text{Ti}$ are potential proton conductors comparable to SCO with lower barriers of 0.32 and 0.21 eV, respectively, for the path 1 proton jumps between interlayer and octahedral layers (Figure B.5). Although $\text{SrTiO}_{2.5}$ shows a low proton-jump barrier, its hydrogenated phase ($\text{H}_{0.125}\text{SrTiO}_{2.5}$) shows poor stability with an energy above hull E_{hull} of 120 meV/atom much higher than that of $\text{H}_{0.125}\text{SrCoO}_{2.5}$ ($E_{\text{hull}} = 19$ meV). In comparison, $\text{SrFeO}_{2.5}$ (SFO) shows a low proton migration barrier of 0.32 eV and good stability ($\text{H}_{0.125}\text{SrFeO}_{2.5}$ with $E_{\text{hull}} = 17$ meV) comparable to the stability of $\text{H}_{0.125}\text{SrCoO}_{2.5}$. Brownmillerite SFO may be a promising proton conductor similar to SCO.

4.4. Discussion

The computational study revealed the proton diffusion mechanism in the brownmillerite SCO structure, which consists of alternating octahedral and pyramid layers. The proton diffusion across the pyramid layer is sluggish due to the high energy of proton bonding with oxygens in the pyramid layer. The fast proton diffusion is mostly through proton jumping and rotation among the oxygen sites on the octahedral layers and interlayers, with a fast 1D diffusion channel along the tetrahedral chain.

Table 4.1. Phase stability comparison of $H_xSrFeO_{2.5}$ and H_xSrFeO_3

x	$E_{\text{hull}}(H_xSrFeO_{2.5})$ meV/atom	$E_{\text{hull}}(H_xSrFeO_3)$ meV/atom
0	0	0
0.125	17	35
0.5	38	76
1	54	138

Given that the brownmillerite structure can be considered as a perovskite structure with half of the oxygens missing from every other octahedral layer, a comparison between brownmillerite and perovskite may provide insight to why brownmillerites provide fast proton diffusion. In the brownmillerite structure, the fast proton diffusion occurs through the oxygens in octahedral layers and the interlayer, similar to that in perovskites. The pyramid layers, which only exist in the brownmillerite structure, do not provide proton diffusion pathways due to their high energy for proton occupancy.

Compared to perovskites, a key advantage of brownmillerite SCO is the ability to incorporate a large number of protons without any dopants. As shown in the computation and previous experiments, brownmillerite SCO can incorporate a large amount of H, up to 1H/f.u., to form HSCO, and maintain good structural stability. This large proton incorporation is compensated by the valence change of B-site transition metals, such as Co. As predicted by the computation, the H incorporation capability of SCO was observed for other brownmillerite-structured compounds, such as $SrFeO_{2.5}$, which also showed good stability as $HSrFeO_{2.5}$. However, this high level of H incorporation is not possible in the cubic perovskites $SrCoO_3$ and $SrFeO_3$. In the calculations, incorporation of a small amount of H ($x = 0.125$) on the relaxed sites on

the octahedral oxygen is enough to raise the E_{hull} of SrCoO_3 to 35 meV/atom, and the same H incorporation in $\text{SrFeO}_{2.5}$ raises the E_{hull} to 17 meV/atom. The incorporation of 1 H/f.u. in the perovskites SrFeO_3 and $\text{HSrFeO}_{2.5}$ raises the E_{hull} to 138 meV/atom and 54 meV/atom, respectively. In addition to the cubic perovskites, orthorhombic perovskites such as SmNiO_3 and SrRuO_3 are experimentally reported to have good hydrogen insertion capability without doping. For these two materials, first principles calculations using the same scheme also show negative hydrogen incorporation energy with increasing proton concentration up to 1H/f.u. (Figure B.6), consistent with prior experiments.^{71,72,176} These results confirm that B-site cations with the capability to change valence may facilitate hydrogen incorporation. However, the calculations also revealed the thermodynamic phase stability of these perovskite materials decreases with increasing hydrogen concentration (Figure B.6), in agreement with the experimental observation of the phase instability of H_xSrRuO_3 .⁷² In summary, compared to single perovskites, the brownmillerite SCO shows good phase stability even at high hydrogen concentration.

In comparison to the brownmillerite SCO, a fundamentally different proton incorporation mechanism in common perovskite proton conductors, such as BaZrO_3 and BaCeO_3 , requires aliovalent B-site doping, e.g. Y-doped BaZrO_3 and Yb-doped BaCeO_3 , to create oxygen vacancies for proton incorporation.^{3,177–179} As a result, the proton concentration in perovskites is limited by the number of B-site dopants. In addition, these aliovalent dopants bind with protons and induce a proton trapping effect, leading to higher activation energy of proton transportation and lower proton conductivity.^{55,59,62,113,127} In contrast, the brownmillerite structure can incorporate

hydrogen without dopants. In brownmillerite SCO, the B-site cations, such as Co and Fe, can change valence and enable the structure to take in a high concentration of H without dopants. In addition, another brownmillerite, BaInO_{2.5}, can also incorporate a large amount of hydrogen without dopants through water dissociation, but the proton migration mechanisms in this structure should be more similar to perovskites.⁸⁹ Moreover, in brownmillerite SCO, the proton sites in MO₆ octahedra have similar energies, reducing the potential energy surface for proton hopping. In addition, the Co cations with mixed oxidation states can also transfer charge within the structure and may alleviate the proton trapping effect. At high H concentration, proton sublattices exhibit similar energies over a wide variety of proton configurations, leading to a highly disordered proton sublattice. The highly disordered mobile-ion sublattice can result in fast ion conduction through correlated migration mechanisms, leading to low activation energy and high ionic conductivity.^{97,169,174,180,181} Similar mechanisms have been shown in fast lithium-ion conductors exhibiting a high lithium ionic conductivity of greater than 1mS/cm at room temperature (RT).¹⁸²⁻¹⁸⁴

My understanding of the fast proton transport mechanism in the brownmillerite structure suggests future directions in developing new proton-conducting materials. In order to achieve significantly higher proton conductivity than current perovskite oxides, the candidate materials should eliminate the proton trapping effects caused by the aliovalent doping for hydrogen incorporation. The candidate materials should be able to incorporate a large amount of hydrogen while maintaining structural stability, and these incorporated protons should have similar site energies. In addition, a significant fraction of proton sites should be vacant for proton hopping, and a highly

disordered proton sublattice is desired. Recently, Li super-ionic conductors were found to exhibit such features and were demonstrated with a high lithium ionic conductivity of greater than 1mS/cm at RT,^{97,135,181} and computational studies discovered multiple novel Li-ion conductors with high ionic conductivity.^{97,108,185} Novel proton conductors can be developed and discovered by activating a similar fast proton diffusion mechanism as in brownmillerite SCO.

Chapter 5. First-Principles Computational Design and Discovery of Solid-Oxide Proton Conductors^{††}

5.1. Introduction

First-principles computation is a powerful approach for studying fundamental materials mechanisms and for materials discovery and design.^{57,59,110,119,122,126,186,65,68,70,75,101,107–109} In this study, we perform a systematic first-principles computation study on a wide range of ternary oxide materials to understand the role of cations and compositions on the proton conduction and the material stabilities, and also to identify new proton conductor materials. According to our computation results, the cations and their mole fractions significantly affect water stability, and high concentrations of hydrogen incorporation can be achieved with multivalent B-cations in oxide materials. By studying the proton diffusion in many different materials, we find that oxide materials with connected BO_6 octahedra are optimal for fast proton diffusion. Following these materials analyses, our high-throughput computation identifies twelve candidates with good water stability, good capability of hydrogen incorporation, and fast proton diffusion. Our results provide general design principles for oxide proton conductors and offer new research directions for novel proton conducting materials.

^{††} This chapter will be published

Islam, M. S.; Wang, S.; Alex T. Hall; Mo, Y., “First-Principles Computational Design and Discovery of Solid-Oxide Proton Conductors”, submitted.

5.2. Methods

5.2.1. Water Stability

To evaluate water stability, we calculated the reaction energies of $A_xB_yO_z$ materials with H_2O using the energies of existing entries in the *Materials Project* (MP) database. These reactions with H_2O were analyzed by treating the reactants as a pseudo-binary

$$C_{pseudo-binary}(C_{A_xB_yO_z}, C_{H_2O}, a) = (1 - a) \cdot C_{A_xB_yO_z} + a \cdot C_{H_2O} \quad (5.1)$$

where $C_{A_xB_yO_z}$ and C_{H_2O} are the compositions of $A_xB_yO_z$ and H_2O normalized to one atom per formula unit, respectively, and a is the mole fraction of the H_2O in the pseudo-binary. This pseudo-binary is the reactants with the energy

$$E_{Reactant} = (1-a) E_{A_xB_yO_z} + a E_{H_2O} \quad (5.2)$$

where $E_{A_xB_yO_z}$ are the DFT energies of $A_xB_yO_z$ materials from the MP database. E_{H_2O} is the DFT energy of H_2O from the MP database. The phase equilibria of the pseudo-binary mixture of $A_xB_yO_z$ and H_2O were then determined by constructing the convex energy hull with all relevant phases using the DFT energies from the MP database.^{98,134} The reaction products were the phase equilibria with the minimum energy $E_{Product}$. For those materials that were stable with water at the original value of E_{H_2O} , a high value of E_{H_2O} would be used so phase equilibria could still be identified as the reaction products. To describe the water stability of a material, the reaction energy ΔE_{H_2O} with H_2O was calculated as

$$\Delta E_{H_2O} = E_{Product} - E_{Reactant} \quad (5.3)$$

and was normalized to one atom of total formula unit of the reactant. For those materials that were stable with water at the original $E_{\text{H}_2\text{O}}$, the values of reaction energies $\Delta E_{\text{H}_2\text{O}}$ would be positive, allowing the comparison of the relative stabilities among different materials.

5.2.2. Energy above hull

The energy above the hull of the $\text{H}_y\text{A}_x\text{B}_y\text{O}_z$ composition was calculated by constructing the convex energy hull using the DFT energies from the MP database.

5.2.3. Proton Diffusion

In this chapter, I only evaluated proton jump energy barriers, which is known to be the rate-limiting step of proton migration.^{3,57,68,73,187,188} The NEB calculations were performed in a supercell with lattice parameter of 8 Å or larger with a single proton. The proton migration paths were identified by selecting the set of equivalent oxygen atoms in the structure. By taking one of the oxygen atoms from each set, the proton migration paths were identified between the oxygen atom and the first nearest neighbor oxygens within a 4 Å cutoff distance. The calculated migration energy barriers of these identified proton migration paths were then used to generate proton migration paths around other equivalent oxygen atoms, enabling the evaluation of the lowest migration energy barrier of the material. We used three-image NEB calculations to obtain the energy barriers as the first screening step for proton diffusion. For those materials with a low proton migration energy barrier of less than 0.5 eV, NEB

calculations with five images along the pathway were performed to obtain more accurate energy profiles and barriers for proton migration.

5.3. Results

5.3.1. High-throughput Computation of Proton Conducting Oxides

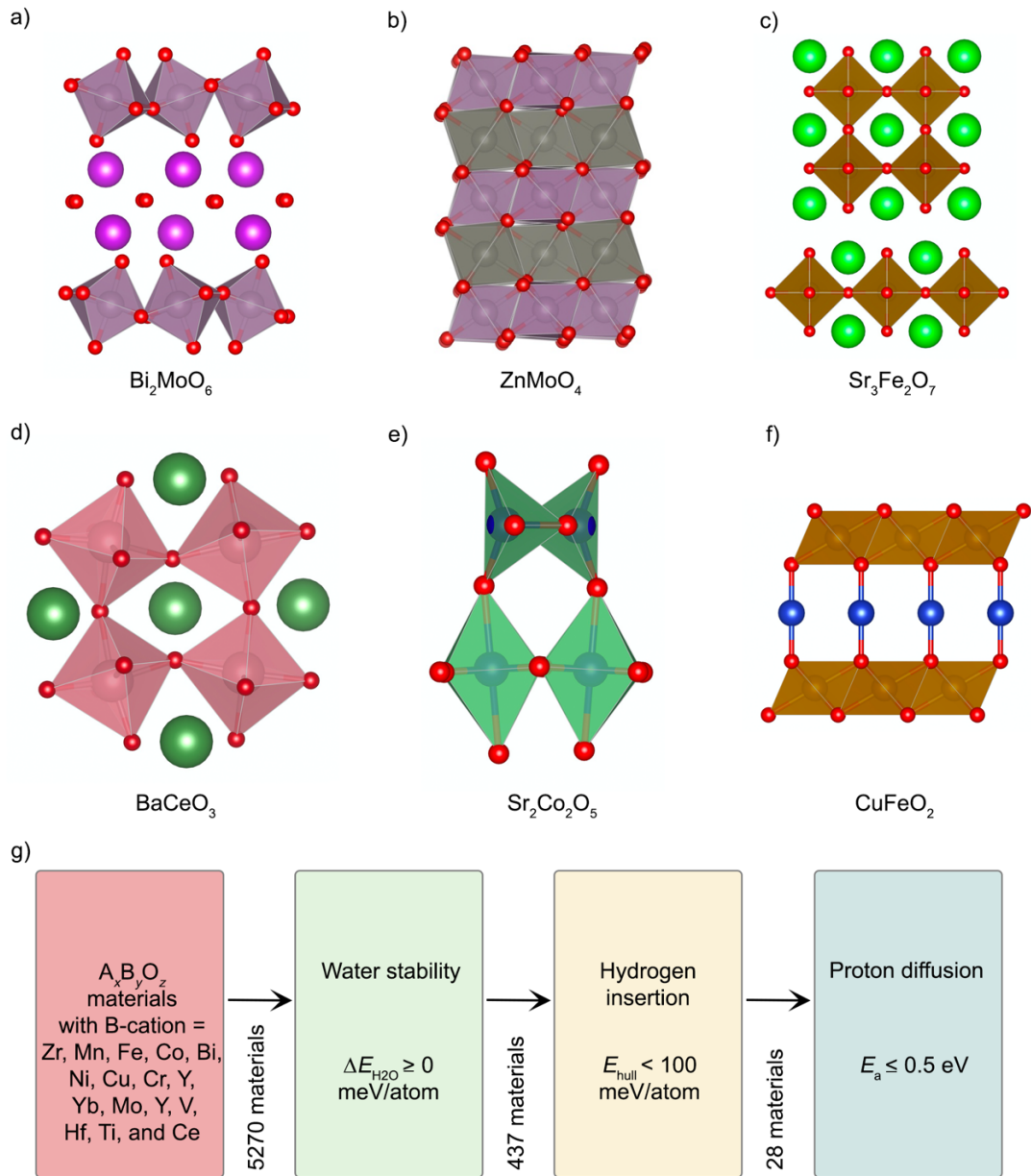


Figure 5.1. Crystal structures of a) Bi_2MoO_6 , b) ZnMoO_4 , c) $\text{Sr}_3\text{Fe}_2\text{O}_7$, d) BaCeO_3 , e) $\text{Sr}_2\text{Co}_2\text{O}_5$, and f) CuFeO_2 as examples from the formula classes A_xBO_6 , A_xBO_4 , $\text{A}_x\text{B}_2\text{O}_7$, A_xBO_3 , $\text{A}_x\text{B}_2\text{O}_5$, A_xBO_2 , respectively. g) High-throughput computation workflow for studying proton conductor materials.

From all the oxide materials in the *Materials Project* (MP) database,¹³⁰ we selected 5270 materials with the general formula $A_xB_yO_z$, where $B = \text{Fe, Co, Bi, Ni, Mn, Mo, Cu, V, Cr, Y, Yb, Nb, Ti, Zr, Ce, Hf}$ and $A = \text{any element except F, Cl, Br, I, and S}$. These multivalent B-cations, such as Fe, Co, Ni, Mn, Mo, Cu, V, and Cr, compensate the change of charge upon hydrogen incorporation, as shown in previous studies.^{71,72,164} Most of the candidate materials can be categorized into six formula classes, A_xBO_6 , A_xBO_4 , $A_xB_2O_7$, A_xBO_3 , $A_xB_2O_5$, and A_xBO_2 , each with a wide range of A- and B-cation combinations in different crystal structures, including perovskites, brownmillerite, and Ruddlesden-Popper (Examples are illustrated in Figure 5.1a-f). A computation workflow is performed to evaluate the water stability, hydrogen incorporation, and proton diffusion in these materials (Figure 5.1g). To evaluate the water stability, we calculate the water reaction energies of these materials (Methods), and the materials with decent water stability with water reaction energy $\Delta E_{H_2O} \geq 0$ meV/atom (section 5.2.2) are further investigated for hydrogen incorporation. The hydrogen incorporation capability of the materials is evaluated (section 5.2.3) by calculating the hydrogen insertion energies of the hydrogenated structures with a hydrogen concentration of 1 H per B-cation generated by computation (Methods). In addition, given that the hydrogenated structures should also maintain good phase stability, we select the materials that have calculated energy above the hull $E_{\text{hull}} < 100$ meV/atom at the hydrogenated structures. For studying proton diffusion (section 5.2.4), we perform nudged-elastic-band (NEB) calculations for the distinct proton migration pathways in the materials and identified the lowest energy migration path (Methods). The materials with migration energy barriers less than 0.5 eV are identified as potential

proton conductor materials (section 5.2.5), which also have good water stability and the capability for incorporating hydrogen. In the following sections, we analyze and summarize the results of the materials for each computation step, which may provide general guidance for future design and selection of proton conductor materials.

5.3.2. Water Stability of Proton Conducting Oxides

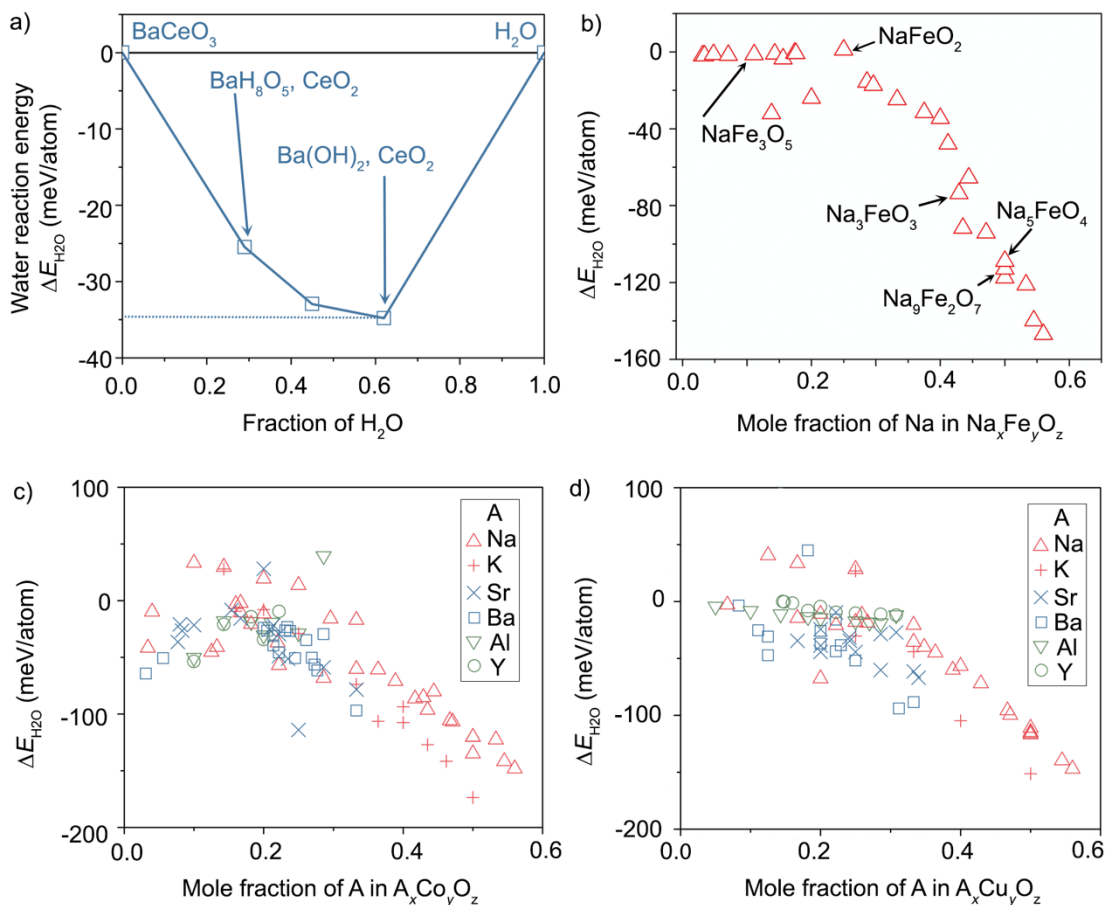


Figure 5.2. a) The reaction energies of the pseudo-binary mixture of BaCeO_3 and H_2O as a function of the mixing fraction. b) Water reaction energies ($\Delta E_{\text{H}_2\text{O}}$) of $\text{Na}_x\text{Fe}_y\text{O}_z$ as a function of Na mole fraction (X_{Na}). Water reaction energies as a function of the mole fraction of A-cation in c) $\text{A}_x\text{Co}_y\text{O}_z$ and d) $\text{A}_x\text{Cu}_y\text{O}_z$ (A=Na, K, Sr, Ba, Al, Y)

We evaluate the water stability of the materials by calculating the water reaction energies of the materials with H_2O (Methods). For instance, the reaction energies of the pseudo-binary mixture of BaCeO_3 and H_2O (Figure 5.2a) show that BaCeO_3 can favorably react with H_2O to form Ba(OH)_2 and CeO_2 , in good agreement with experimental observations.^{189–195} We calculate and compare water reaction energies for a wide range of $\text{A}_x\text{B}_y\text{O}_z$ materials. In general, the materials with a high mole fraction

of A-cation exhibit poor water stability. For example, $\text{Na}_x\text{Fe}_y\text{O}_z$ compositions with increasing Na mole fraction exhibit a more negative water reaction energy, i.e., poorer stability with water (Figure 5.2b). Similar trends are observed among $\text{A}_x\text{Co}_y\text{O}_z$, $\text{A}_x\text{Cu}_y\text{O}_z$ (Figure 5.2c-d) and other formula classes (Figure C.1).

Among the compounds within each formula class, the water stabilities vary with the cations in the compositions. In particular, the A-cation plays a critical role in determining water stability (Figure 5.2c,d). The A-cations with the oxidation states of 1+, such as Li, K, Na, and 2+, such as Ca, Sr, and Ba, generally lead to poorer stability with H_2O , as a result of the energetically favorable formation of these alkaline or alkaline earth metal hydroxides. In contrast, the materials with A-cations of oxidation-state of 3+, such as Al, Ga, In, Sc, Y and Lanthanum group elements La, Pr, Nd, Sm, Eu, Gd, Tb, Dy, Ho, Er, Tm, Yb, show less negative water reaction energies (Figure 5.2c-d, Figure C.1), i.e., better stabilities with H_2O . These results suggest the compounds having A-cations with a high oxidation state and a low mole fraction for good water stability.

Our plot of the water reaction energies for a wide range of oxide compositions also show the significant effect of B cations on water stability (Figure 5.3a-d, Figure C.2 and Supporting Information). For ABO_3 (Figure 5.3a), Ce, Co, and Ti-based compounds are less stable with water (more negative water reaction energies) than those containing Ni, V, or Zr. In agreement with experiments,^{189–192} our scheme also shows that BaZrO_3 exhibits good water stability while BaCeO_3 does not. The Ruddlesden–Popper Pr_2NiO_4 is reported to slowly decompose in an H_2O containing environment,^{196–198} which agrees with our calculation results (Figure 5.3b). Our

calculations show that PrNiO_3 is more stable than PrCoO_3 (Figure 5.3a), in good agreement with the experiments by Ding et al. that demonstrated $\text{PrNi}_{0.5}\text{Co}_{0.5}\text{O}_3$ with significantly improved water stability than PrCoO_3 .⁶⁶ Therefore, the results of the cation trends on water stability can be used to guide the cation substitution for improving water stability. In general, good water stabilities are observed for several B-cation compositions, including AMnO_4 , AmoO_4 , A_2MoO_4 , A_2MoO_6 , A_3MoO_6 , $\text{A}_2\text{Mn}_2\text{O}_7$, $\text{A}_2\text{V}_2\text{O}_7$, $\text{A}_{0.5}\text{VO}_3$, and ACuO_2 . To guide the cation selection for designing oxides with good water stability, we plot the water reaction energies for a wide range of oxide compositions (Figure 5.3a-d, Figure C.2).

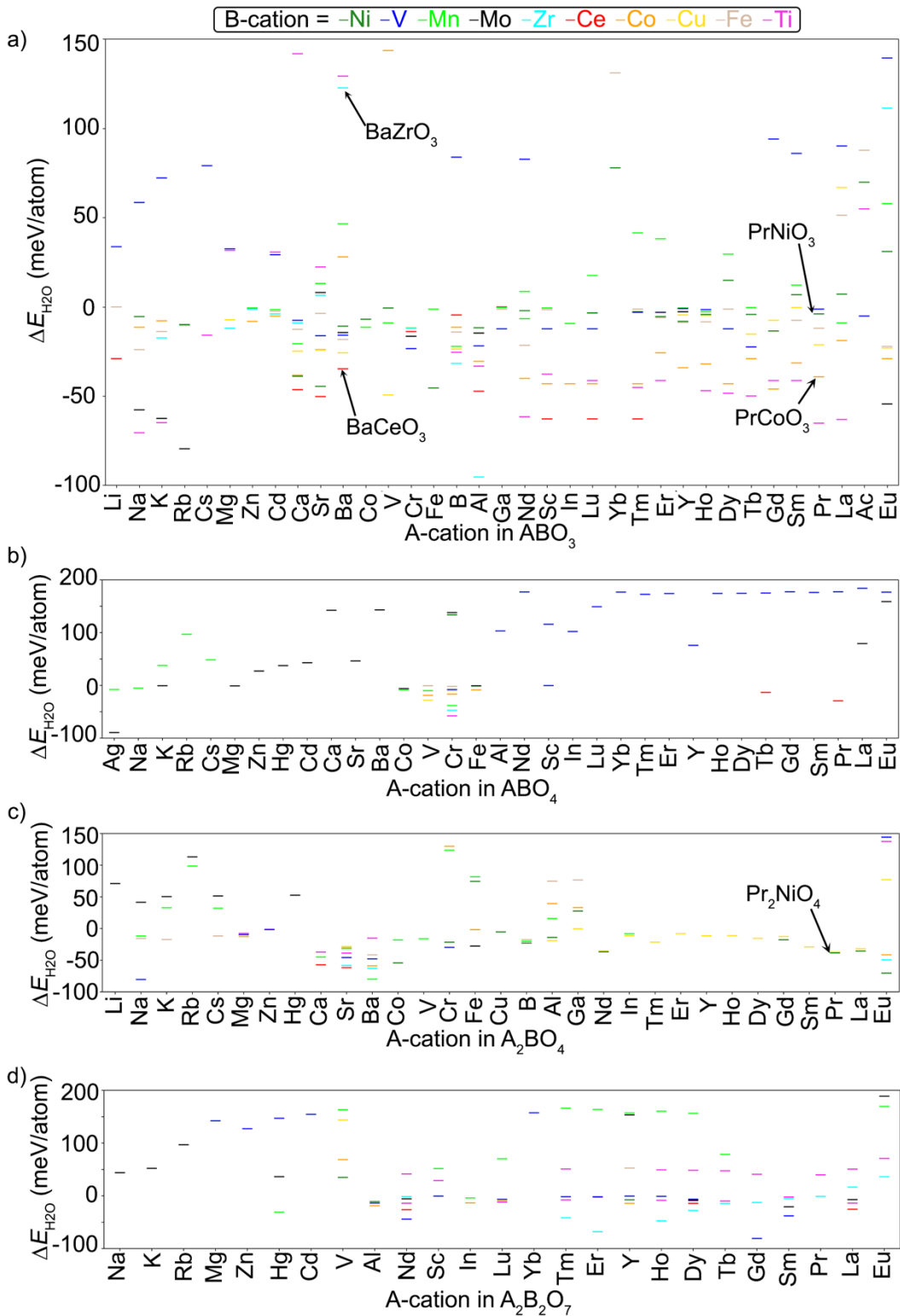


Figure 5.3. Water reaction energies ($\Delta E_{\text{H}_2\text{O}}$) for the materials in a) ABO_3 , b) ABO_4 , c) A_2BO_4 , and d) $\text{A}_2\text{B}_2\text{O}_7$ formula classes. A-cations are arranged in ascending order of oxidation states from left to right.

We evaluate hydrogen incorporation in materials with good water stability having $\Delta E_{\text{H}_2\text{O}} \geq 0$ meV/atom (Methods). The hydrogen insertion energies are assessed in the materials with inserted hydrogen concentration of 1 H per B-cation. For example, the brownmillerite $\text{Sr}_2\text{Co}_2\text{O}_5$ to form $\text{H}_2\text{Sr}_2\text{Co}_2\text{O}_5$ after inserting 1 H per Co-cation has a negative hydrogen insertion energy (Figure 5.4a), in agreement with the previous experimental studies that showed favorable hydrogen incorporation to the same concentration.^{41,70} In contrast, the perovskite BaCeO_3 exhibits a positive hydrogen insertion energy (3.12 eV/H), in agreement with the fact that acceptor dopants are required in BaCeO_3 for incorporating hydrogen.^{3,41,91,93,145,146} In this way, our computation approach identifies the materials that can incorporate hydrogen directly without aliovalent doping.

In addition, we calculate the energy above the hull E_{hull} of these protonated structures to evaluate the phase stability of the hydrogenated materials.^{70,98,134,135,199,200} The E_{hull} values of the protonated structures generally remain low in the materials with more negative hydrogen insertion energies $\Delta E_{\text{hydrogen}}$ (Figure 5.4b and C.3). These materials with low E_{hull} may retain good phase stability during hydrogenation. A range of candidate materials containing A-cations including K, Na, Rb, Sr, or Ba, and B-cation including Cu, Co, Fe, Mn, or Ni show negative hydrogen insertion energies (Figure 5.4c-d) and good phase stability with $E_{\text{hull}} < 100$ meV/atom. Notably, many compositions in A_xBO_6 , $\text{A}_x\text{B}_2\text{O}_7$, and A_xBO_4 with B = Mo (A = Y, Dy, Sm, Pr, La, Eu, Nb, Tb, or Cr) demonstrate good capability for hydrogen incorporation. Therefore, our computation identifies many materials with multivalent cations that can incorporate a high concentration of hydrogen.

5.3.4. Proton Diffusion in Oxide Materials

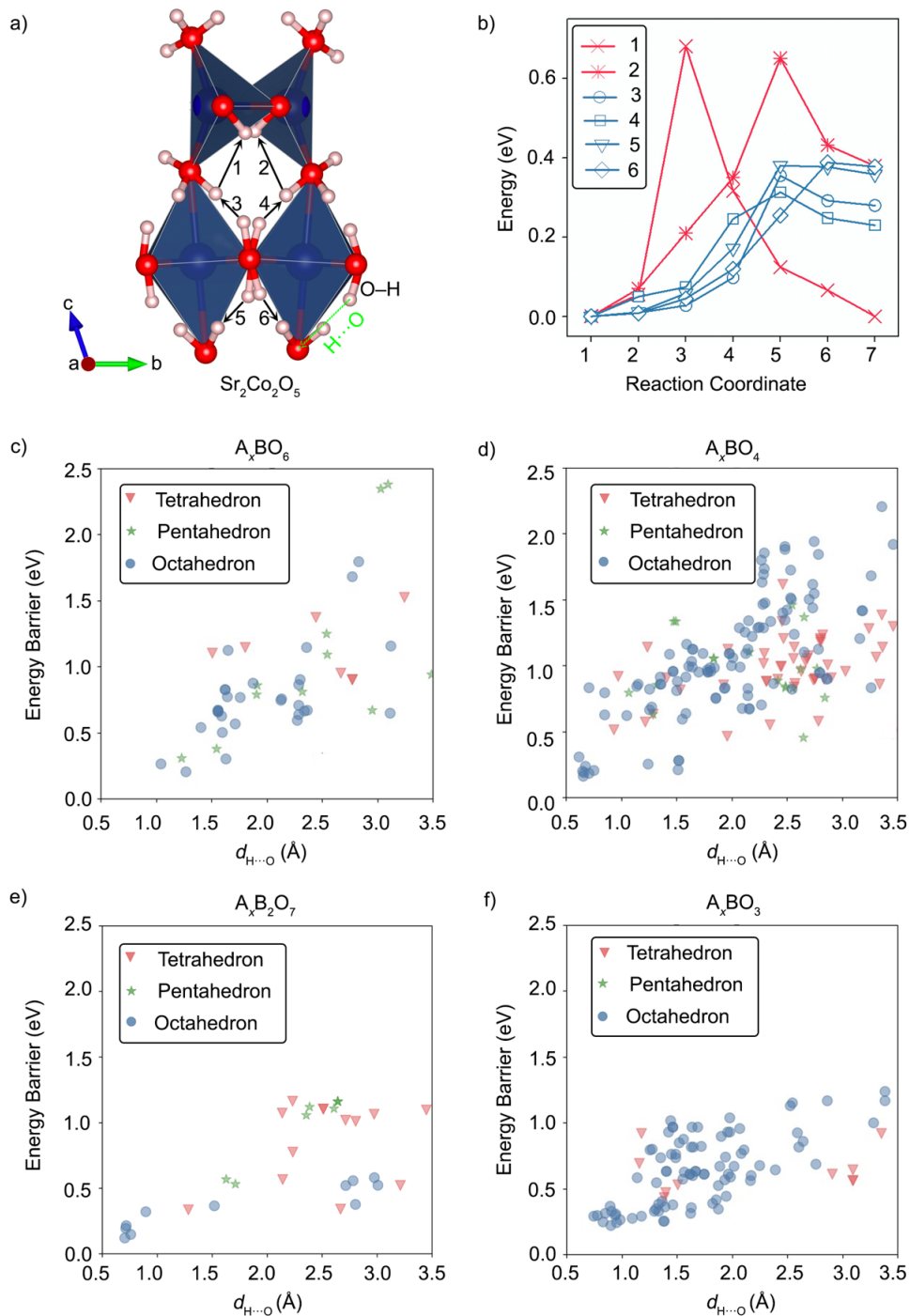


Figure 5.5. a) Proton sites and migration pathways and b) the energy profile of the proton migration in $\text{Sr}_2\text{Co}_2\text{O}_5$. The energy barrier of proton migration as a function of hydrogen bond length $d_{\text{H}\cdots\text{O}}$ for different pathways in a range of materials in c) A_xBO_6 , d) A_xBO_4 , e) $\text{A}_x\text{B}_2\text{O}_7$, and f) A_xBO_3 formula classes.

We evaluate proton diffusion in the materials with good water stability and hydrogen incorporation capability (Table 5.1). In oxides, protons bond with their nearest-neighbor oxygen anions with a bond length of approximately 1 Å (O–H) (Figure 5.5a). The proton diffusion consists of proton jumps between two neighboring oxygens and proton rotations around an oxygen anion. The proton jumps are known to have higher energy barriers than the proton rotations,^{3,57,68,73,187,188} and are often rate-limiting. Here we only evaluate the proton jumps for screening proton-conductors. We analyze all proton jump pathways among the oxygens in different B-cation coordination environments, such as BO₄ tetrahedra, BO₅ pentahedra, and BO₆ octahedra, in the candidate oxide materials. For example, the Sr₂Co₂O₅ brownmillerite structure contains CoO₆ octahedra and CoO₄ tetrahedra (Figure 5.5a), which form a network of proton migration pathways (Figure 5.5a). As shown by the NEB calculations, the energy barriers of proton jump migrations along the edges of CoO₆ octahedra are significantly lower than those along the edge of CoO₄ tetrahedra (Figure 5.5b).

By analyzing the proton migration energy barriers in these candidate materials, we observe that the energy barriers for proton jump migration along BO₆ octahedra are generally lower than other types of BO_x polyhedra (Figure 5.5c-f). The energy barrier of proton jump migration can be understood by the breaking and reforming of an O–H covalent bond with the nearest-neighbor oxygen and a hydrogen bond (H···O) with the next nearest-neighbor oxygen, which becomes the new O–H covalent bond after proton jump (Figure 5.5a). We observe that in general shorter hydrogen bond distances ($d_{\text{H}\cdots\text{O}}$) are correlated with lower energy barriers (Figure 5.5c-f). Since shorter hydrogen bond

lengths ($d_{\text{H}\cdots\text{O}}$) are observed for the protons bonded to BO_6 octahedra, the BO_6 octahedra are generally more beneficial for proton migration. This observation may explain why perovskites with 3D-connected BO_6 octahedra are generally good proton conductors and why brownmillerites form fast proton conduction in the octahedra layer.^{70,91}

Table 5.1. Proton conductors identified by computation.

Material composition	ICSD-ID	MP-ID	Space group	Water reaction energy $\Delta E_{\text{H}_2\text{O}}$ (meV/atom)	E_{hull} at 1 H/B-cation (meV/atom)	Hydrogen insertion energy $\Delta E_{\text{hydrogen}}$ (eV/H)	Energy Barrier (eV)
YbFeO ₃	27284	mp-19793	<i>Pnma</i>	70	59	-2.46	0.13
AcFeO ₃	–	mp-861502	<i>Pm$\bar{3}m$</i>	37	101	-1.12	0.16
MoPO ₅	–	mp-26372	<i>Pnma</i>	28	26	-0.61	0.3
Sr ₂ Co ₂ O ₅	162239	mp-645208	<i>Pnma</i>	6	66	-1.19	0.32
YbCoO ₃	172051	mp-687081	<i>Pnma</i>	49	93	-1.78	0.32
Mn ₂ TeO ₆	–	mp-1210598	<i>P4₂/mnm</i>	26	62	-1.54	0.35
NbMoO ₄	–	mp-1220430	<i>Cmmm</i>	39	101	-2.20	0.35
Tb ₂ Mo ₂ O ₇	159771	mp-19200	<i>Fd$\bar{3}m$</i>	1	99	-0.62	0.38
CaFeO ₃	92330	mp-19115	<i>R3c</i>	4	91	-1.61	0.40
CrMoO ₄	–	mp-1213733	<i>Cmmm</i>	137	69	-2.80	0.42
Eu ₃ MoO ₇	–	mp-1213342	<i>P2₁2₁2₁</i>	89	94	-0.25	0.45
SrMnO ₃	157936	mp-559975	<i>C222₁</i>	13	81	-1.25	0.47
Nd ₂ Mo ₂ O ₇	291030	mp-33803	<i>Fd$\bar{3}m$</i>	6	97	-0.33	0.52
YbNiO ₃	189293	mp-19249	<i>Pnma</i>	40	71	-2.05	0.59
EuMnO ₃	95492	mp-20614	<i>Pnma</i>	58	77	-0.72	0.69
Ni(BiO ₃) ₂	–	mp-1101457	<i>P4₂/mnm</i>	38	68	-1.70	0.85
HgMoO ₄	2533	mp-19363	<i>C2/c</i>	37	84	-1.29	0.93
CaMoO ₃	172790	mp-19012	<i>Pnma</i>	6	98	-0.42	0.97
MnMoO ₄	78328	mp-19081	<i>C2/m</i>	62	96	-0.69	0.98
UMnO ₄	–	mp-19173	<i>Imma</i>	0	32	-0.52	1.12
CoWO ₄	15851	mp-19092	<i>P2/c</i>	59	64	-0.65	1.21
TaFeO ₄	–	mp-755628	<i>P2/c</i>	9	41	-1.13	1.35
Mn(PO ₃) ₂	412558	mp-542139	<i>C2/c</i>	2	89	0.06	1.36
FeWO ₄	26811	mp-19421	<i>P2/c</i>	61	47	-0.69	1.42
MnWO ₄	67910	mp-19407	<i>P2/c</i>	76	18	-0.88	1.42
Co(BiO ₃) ₂	–	mp-765403	<i>P321</i>	2	75	-1.81	1.69
NiWO ₄	16685	mp-21179	<i>P2/c</i>	31	93	-0.74	1.91
Mn ₂ CdO ₄	24258	mp-18720	<i>I4₁/amd</i>	22	98	-0.90	1.92

5.3.5. New Proton Conductor Materials

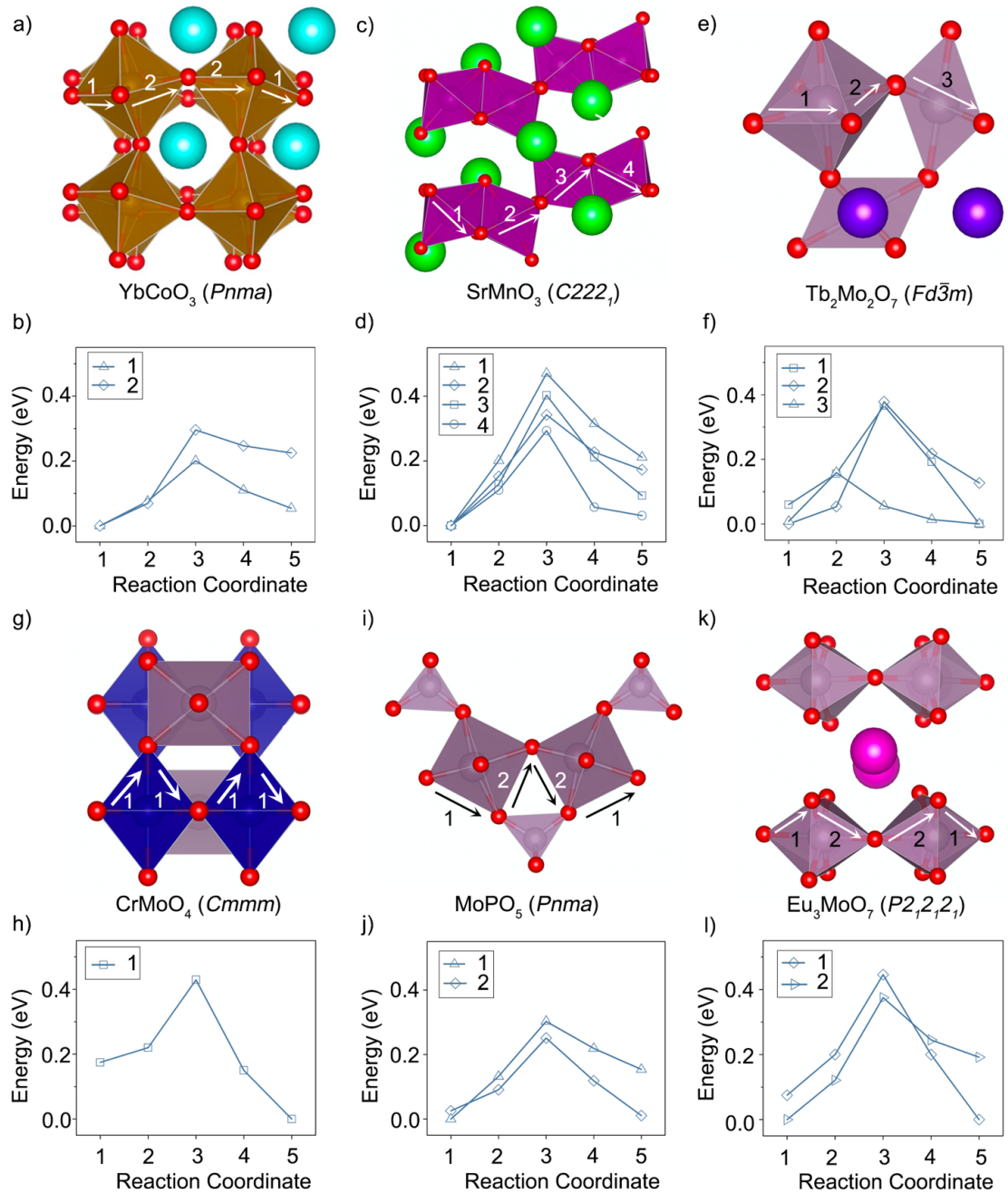


Figure 5.6. Low energy proton migration pathways and the energy profiles in representative proton conductor materials a-b) perovskite YbCoO_3 , c-d) SrMnO_3 , e-f) $\text{Tb}_2\text{Mo}_2\text{O}_7$, g-h) CrMoO_4 , i-j) MoPO_5 , and k-l) Eu_3MoO_7 .

Our high-throughput computation workflow identifies 12 materials with good water stability, good capability of hydrogen incorporation, and fast proton diffusion with a proton migration energy barrier of less than 0.5 eV (Table 5.1). Many of these materials are A_xBO_3 ($AcFeO_3$, $YbCoO_3$, $YbFeO_3$, $CaFeO_3$) and $A_xB_2O_7$ ($Tb_2Mo_2O_7$), as these crystal structures consist of 3D-connected BO_6 octahedra for low-energy proton migration pathways (Figure 5.6). Other identified proton conductors, such as Eu_3MoO_7 , $Sr_2Co_2O_5$, Mn_2TeO_6 , $NbMoO_4$, and $CrMoO_4$, have connected BO_6 octahedra forming 2D layers in the crystal structures for fast proton diffusion (Figure 5.6). These results agree with our finding (section 5.2.4) that the proton migrations are generally easier among BO_6 octahedra. In summary, our computation study on a wide range of materials identifies a number of potential proton conductor oxides and provides related materials design guidelines.

5.4. Discussion and Conclusions

This study employs the first-principles computations to systematically analyze a wide range of ternary oxide materials with a large variety of cation combinations for their hydrogen incorporation, proton diffusion, and water stability, which are relevant for the applications of these materials. Our computational results reveal the impact of cations on stabilities and proton conduction, offering guidelines for future materials design.

Our computation study on a large number of materials identifies that connected BO_6 octahedra in the oxide crystal structures are generally beneficial for fast proton diffusion. This result explains that many well-known proton conductors are

perovskites, which feature 3D-connected BO_6 octahedra. The brownmillerite $\text{Sr}_2\text{Co}_2\text{O}_5$, a newly reported fast proton conductor, exhibits faster proton diffusion in the layer with 2D connected CoO_6 octahedra, in agreement with a previous computational study.⁷⁰ Among the computation-identified proton conductor materials, many contain connected BO_6 octahedra polyhedra, including perovskite AFeO_3 , $\text{A}_2\text{Mo}_2\text{O}_7$, and AMoO_4 , and exhibit low energy barriers of proton migration. The connectivity of cation-oxygen octahedra may serve as a simple feature to identify good proton conductors.

Chapter 6. Conclusions and Future Work^{‡‡}

6.1. Conclusions

I employed first-principles computation to systematically analyze the hydrogen incorporation and proton diffusion in a large number of known or predicted perovskite materials, including single and double perovskites with a wide range of B-site cations. The double perovskites can be optimized for hydrogen incorporation and diffusion using appropriate cation combinations by having two different B-site cations. I found that if these B'-site cations form layered ordering or connect through corner-sharing B'O₆ octahedra, good proton migration pathways with low barrier would form among these B'O₆ octahedra layers. The provided chart for the phase stability of hydrogen incorporated double-B perovskites with different B-site cation combinations might guide the selection of the B-site cations and dopants for designing phase-stable proton-conducting materials. In addition, the calculations showed that the layered B-site cation ordering may be energetically favorable in several hydrogen incorporated phases. Therefore, the proposed double perovskites with two B-site cations provided a promising direction for the future development of the proton conduction materials.

I revealed the atomistic mechanism of proton diffusion in brownmillerite SrCoO_{2.5}, which is promising because of the exceptionally high proton conductivity at

^{‡‡} Some text of introduction is adapted from my published papers:

Islam, M. S.; Wang, S.; Nolan, A. M.; Mo, Y., “First-Principles Computational Design and Discovery of Novel Double-Perovskite Proton Conductors”, *Chem. Mater.* (2021).

Islam, M. S.; Nolan, A. M.; Wang, S.; Bai, Q.; Mo, Y. “A Computational Study of Fast Proton Diffusion in Brownmillerite Sr₂Co₂O₅”, *Chem. Mater.* 32 (2020) (12), 5028–5035.

Islam, M. S.; Wang, S.; Alex T. Hall; Mo, Y., “First-Principles Computational Design and Discovery of Solid-Oxide Proton Conductors”, submitted, 2022.

the hydronated phase ($\text{HSrCoO}_{2.5}$). The calculation suggested that multivalent Co enables SCO to take in 1 H per formula unit to form HSCO without any dopants. The proton sublattices and their energetics were studied in different H concentrations, suggesting a proton sublattice favorable for fast proton diffusion. I systematically studied proton diffusion pathways in the brownmillerite structures, identified sluggish proton diffusion across the CoO_4 pyramid layers, and confirmed the fast diffusion within CoO_6 octahedral layers. I concluded the good structural stability and fast proton diffusion in this brownmillerite compound.

Finally, I employed the first-principles computations to systematically analyze a wide range of ternary oxide materials with a large variety of cation combinations for their hydrogen incorporation, proton diffusion, and water stability, which are relevant for the applications of these materials. The computational results revealed that the connected BO_6 octahedra in the oxide crystal structures are generally beneficial for fast proton diffusion. The high-throughput screening identified multiple A_xBO_3 , A_xBO_4 , and $\text{A}_x\text{B}_2\text{O}_7$ compounds including AcFeO_3 , YbCoO_3 , YbFeO_3 , CaFeO_3 , and $\text{Tb}_2\text{Mo}_2\text{O}_7$, as promising proton conductors. In addition, the computation provided a general understanding of how the cations affect the water stability of the oxide materials. The calculated chart of water stabilities (Figure 5.3 and Figure C.2) with different cation combinations can be used to guide the selection of cations and dopants for designing the oxides with improved water stabilities. In summary, this thesis offered fundamental understanding and proposed design principles to develop oxide proton conductor materials with fast proton conduction and good stabilities.

6.2. Future work

This thesis offers several computationally predicted proton conductor oxide materials with fast proton diffusion, high proton incorporation, and good water stability. Further experimental studies are needed to confirm our computationally predicted new materials. In the experimental synthesis of these materials, the actual compositions may form nonoptimal cationic rearrangement for the proton conduction, which we did not consider in computation. Additionally, while this thesis contains several fundamental studies on proton diffusion in the bulk crystal structure, it did not consider the solid-solid interfaces, including grain boundaries, and how they affect the proton diffusion in the materials. In addition, these predicted materials can be further optimized for hydrogen incorporation and water stability by substituting favorable cations. This is a promising direction to further optimize the candidate materials identified in our computation for their applications in the next-generation energy devices such as SOFCs and SOECs.

Publications

- (1) Zhu, F.; **Islam, M. S.**; Zhou, L.; Gu, Z.; Liu, T.; Wang, X.; Luo, J.; Nan, C. W.; Mo, Y.; Ma, C. Single-Atom-Layer Traps in a Solid Electrolyte for Lithium Batteries. *Nat. Commun.* **2020**, *11* (1), 1–9. <https://doi.org/10.1038/s41467-020-15544-x>.
- (2) **Islam, M. S.**; Nolan, A. M.; Wang, S.; Bai, Q.; Mo, Y. A Computational Study of Fast Proton Diffusion in Brownmillerite $\text{Sr}_2\text{Co}_2\text{O}_5$. *Chem. Mater.* **2020**, *32* (12), 5028–5035. <https://doi.org/10.1021/acs.chemmater.0c00544>.
- (3) **Islam, M. S.**; Wang, S.; Nolan, A. M.; Mo, Y. First-Principles Computational Design and Discovery of Novel Double-Perovskite Proton Conductors. *Chem. Mater.* **2021**. <https://doi.org/10.1021/acs.chemmater.1c02432>.
- (4) **Islam, M. S.**; Wang, S.; Alex T. Hall; Mo, Y., “First-Principles Computational Design and Discovery of Solid-Oxide Proton Conductors”, submitted.

Appendices

Appendix A

Appendix A provides supplementary materials for the chapter 3, including radial distribution analysis, proton migration barrier, correlation between proton migration barrier and structural features, the energy of hydrogen insertion, and predicted new materials.

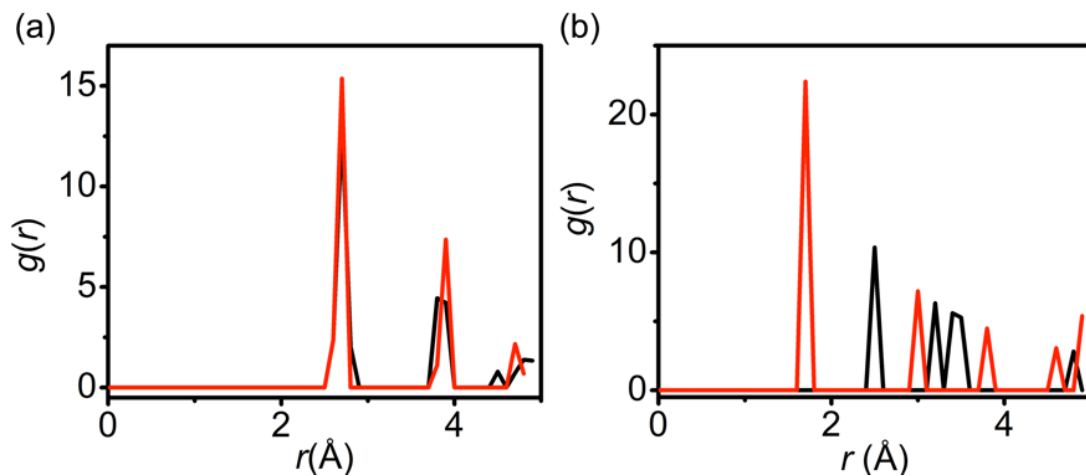


Figure A.1. Radial distribution function $g(r)$ of proton from different hydrogen sites to Ba sites (center) in a) cubic BaZrO_3 perovskite and b) orthorhombic BaCeO_3 perovskite.

Table A.1. Comparison of our calculated proton jump energy barriers in different perovskite structures with reported values.

Composition	This work [eV]	Energy barrier (computation) [eV]	Energy barrier (Experimental) [eV]
BaYb _{0.25} Ce _{0.25} O ₃	0.56	0.22-0.58 ^[73]	0.54 (Nd doped) ^[145]
SrYb _{0.25} Ce _{0.75} O ₃	0.648	0.67 ^[1]	0.63 (Yb doped) ^[143]
BaY _{0.25} Zr _{0.75} O ₃	0.35	0.25-0.29 ^[4, 5]	0.43-0.48 (Y doped) ^[5-7]
SrTiO ₃	0.36	0.3-0.7 ^[9]	0.41 (Sc doped) ^[112]

Table A.2. Comparison of energy barriers of proton jump and rotation in perovskite materials.

Composition	Jump energy barrier [eV]	Rotation energy barrier [eV]
BaFeO ₃	0.21	0.20
BaTiO ₃	0.18, ^[9] 0.29	0.16, ^[68] 0.31
BaZrO ₃	0.27, ^[68] 0.30	0.1, ^[68] 0.18
SrCeO ₃	0.55	0.28
SrFeO ₃	0.23	0.23
SrTiO ₃	0.33, ^[68] 0.36	0.16, ^[68] 0.18
SrZrO ₃	0.80, ^[68] 0.50	0.22, ^[68] 0.43

Table A.3. Structural parameters for analyzing the correlation with proton migration energy barrier.

Parameter	Description
oxi_A	Oxidation state of A-site cation
oxi_B	Oxidation state of B-site cation
r_A	Ionic radius of A-site cation
r_B	Ionic radius of B-site cation
a	Lattice constant of pristine unit cell
t	Goldschmidt factor
d_{O-O}	The oxygen-to-oxygen distance within the same BO_6 octahedron
d_{H-O}	The bond length of the H-O covalent bond between proton to the nearest oxygen
d_{H--O}	The H--O hydrogen bond length from proton to the second nearest oxygen
d_{B-H}	The distance from the proton to the nearest B-site cation
d_{B-O}	The distance of oxygen to B cation in the BO_6 octahedron
d_{A-H}	The distance from the proton to the nearest A-site cation
d_{O-O_t}	Oxygen-oxygen distance within the same BO_6 octahedron at the transition state of proton migration
d_{H-O_t}	The distance from proton to the nearest oxygen within the same BO_6 octahedron at the transition state of proton migration
d_{H--O_t}	Hydrogen bond (O--H) length of migrating proton at the transition state of proton migration
d_{B-H_t}	The distance from the proton to the nearest B-site cation at the transition state of proton migration
d_{B-O_t}	The distance of oxygen to B cation in the BO_6 octahedron at the transition state of proton migration
d_{A-H_t}	The distance from the proton to the nearest A-site cation at the transition state of proton migration
ζ	Stretching parameter of the BO_6 octahedron bonding with proton ^[149]
Δ	Mean stretching parameter of the BO_6 octahedron bonding with proton ^[149]
Σ	Angular distortion parameter of the BO_6 octahedron bonding with proton ^[149]
Θ	Torsional distortion parameter of the BO_6 octahedron bonding with proton ^[149]
$Free_vol$	Free volume (unit cell volume – lattice volume)
Ed_{ABOH}	Ewald energy of hydrogenated structure
X_A	Electronegativity of A-site cation
X_B	Electronegativity of B-site cation
ΔH	Energy of hydrogen insertion at 0.125 H/f.u.
$Vol_{ABO/ABOH}$	Volume ratio of supercell structure before and after hydrogen insertion into the structure

Analyzing the correlation of proton migration energy barrier with crystal structural

parameters. We have performed linear regression analysis to find the correlation of proton jump migration energy barrier (E_a) with a range of structural parameters listed in Table A.3. To quantify the correlation, we perform linear regression of with proton migration energy barrier with two parameters (Figure A.2). The correlation score (R^2)

greater than 0.6 is observed for the parameters $d_{\text{H-O}}$ or $d_{\text{B-H}}$, which are good descriptors of proton migration energy barrier in cubic perovskite structure.

Table A.4. Structural parameters and proton migration barrier of cubic perovskite materials.

Composition	r_A [Å]	r_B [Å]	$2a$ [Å]	d_{O-O} [Å]	d_{H-O} [Å]	d_{H-O} [Å]	d_{B-H} [Å]	d_{B-O} [Å]	d_{A-H} [Å]	E_a [eV]
KTaO ₃	1.64	0.64	8.12	2.71	0.98	2.19	2.45	2.14	2.34	0.39
RbBiO ₃	1.72	0.76	8.54	2.76	0.99	2.17	2.51	2.25	2.51	0.37
BaZrO ₃	1.61	0.72	8.50	2.85	0.99	2.17	2.39	2.24	2.62	0.27
BaNbO ₃	1.61	0.68	8.34	2.83	0.98	2.10	2.28	2.21	2.50	0.35
BaSnO ₃	1.61	0.69	8.38	2.76	0.99	2.12	2.40	2.19	2.54	0.37
BaHfO ₃	1.61	0.71	8.42	2.81	0.98	2.11	2.34	2.21	2.54	0.39
SrTiO ₃	1.44	0.61	7.90	2.71	0.99	2.00	2.26	2.12	2.45	0.36
KNbO ₃	1.64	0.64	8.20	2.74	0.98	2.16	2.48	2.18	2.35	0.33
BaTiO ₃	1.61	0.61	8.07	2.72	0.98	1.97	2.23	2.16	2.44	0.29
CsBiO ₃	1.88	0.76	8.73	2.87	0.98	2.28	2.57	2.32	2.58	0.51
BaTaO ₃	1.61	0.68	8.22	2.82	0.98	2.09	2.27	2.18	2.47	0.36
KHfO ₃	1.64	0.71	8.38	2.78	0.98	2.19	2.45	2.20	2.45	0.39
SrVO ₃	1.44	0.58	7.80	2.63	0.99	1.82	2.10	2.07	2.42	0.22
NaNbO ₃	1.39	0.64	7.95	2.74	1.00	2.41	2.71	2.19	2.23	0.68
RbIrO ₃	1.72	0.57	7.94	2.60	0.98	2.01	2.38	2.11	2.32	0.39
SrAlO ₃	1.44	0.54	7.61	2.55	0.99	1.70	2.00	2.04	2.31	0.15
RbTaO ₃	1.72	0.78	8.06	2.75	0.98	2.17	2.43	2.18	2.34	0.47
KWO ₃	1.64	0.62	8.03	2.73	0.98	2.20	2.42	2.08	2.32	0.49
RbNbO ₃	1.72	0.64	8.23	2.78	0.97	2.16	2.46	2.20	2.37	0.46
RbOsO ₃	1.72	0.58	7.88	2.65	0.97	2.11	2.37	2.09	2.27	0.39
BaOsO ₃	1.61	0.63	8.10	2.61	0.98	1.90	2.30	2.14	2.42	0.23
RbSbO ₃	1.72	0.60	8.08	2.68	0.98	2.11	2.40	2.14	2.35	0.39
SrFeO ₃	1.44	0.58	7.74	2.64	0.98	1.95	2.19	2.06	2.40	0.23
BaFeO ₃	1.61	0.58	8.06	2.74	0.98	1.90	2.17	2.33	2.44	0.23
SrNiO ₃	1.44	0.48	7.72	2.57	0.99	1.74	2.04	2.04	2.38	0.15
SrCoO ₃	1.44	0.53	7.64	2.75	0.98	2.18	2.32	2.03	2.40	0.37
BaCuO ₃	1.61	0.54	8.07	2.68	0.99	1.80	2.11	2.25	2.46	0.21

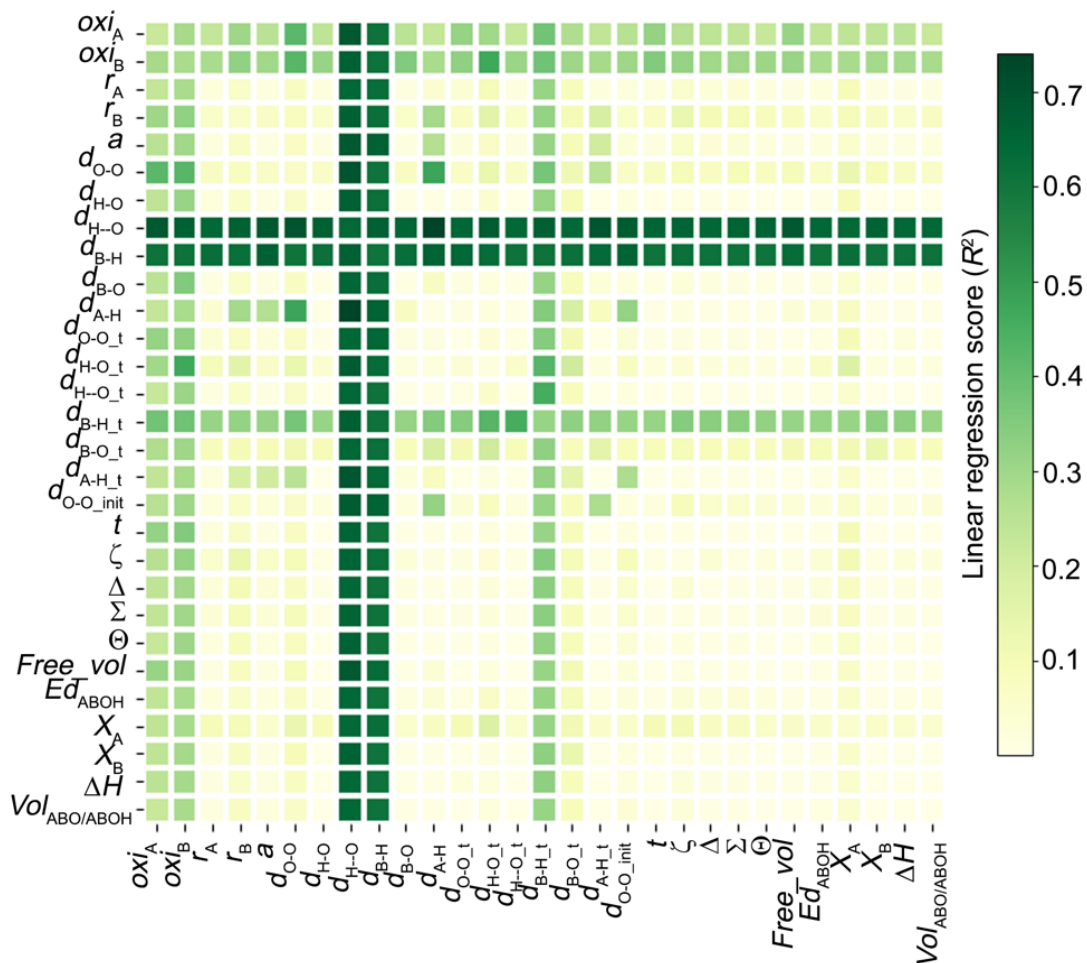


Figure A.2. Correlation score (color bar) of the linear regression proton migration energy barriers to any combinations of two structural parameters of cubic perovskite compositions listed in Table A.4.

Relation between hydrogen insertion reaction and hydration reaction

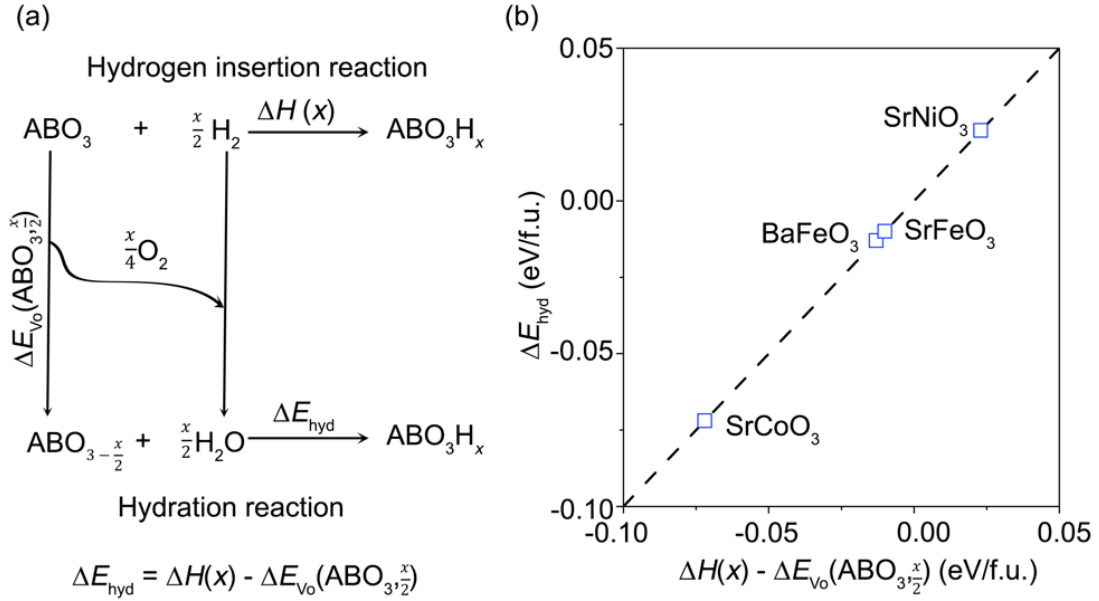


Figure A.3. (a) Schematic of the relation between hydrogen insertion reaction and hydration reaction. (b) Hydration energy as a function of difference between the energy of hydrogen insertion and formation energy of oxygen vacancy.

In this thesis, the energy of inserting x amount of hydrogen in ABO_3 perovskite structure was evaluated according to the reaction



The reaction energy $\Delta H(x)$ for incorporating x amount of hydrogen in the structure (hydrogen insertion energy) was calculated as

$$\Delta H(x) = E(ABO_3H_x) - E(ABO_3) - x\mu_H \quad (2)$$

where, μ_H is the H chemical potential, and $E(ABO_3)$ and $E(ABO_3H_x)$ are the energy of pristine ABO_3 and protonated ABO_3H_x , respectively.

The hydration reaction of the material with $\frac{x}{2}$ amount of oxygen vacancy $ABO_{3-\frac{x}{2}}$ was evaluated according to the reaction



The hydration reaction energy ΔE_{hyd} for incorporating x amount of hydrogen in $\text{ABO}_{3-\frac{x}{2}}$ through hydration was calculated as

$$\Delta E_{\text{hyd}} = E(\text{ABO}_3\text{H}_x) - E\left(\text{ABO}_{3-\frac{x}{2}}\right) - \frac{x}{2}\mu_{\text{H}_2\text{O}} \quad (4)$$

where $\mu_{\text{H}_2\text{O}}$ is the chemical potential of H_2O .

The oxygen vacancy formation in ABO_3 perovskite structure was evaluated using reaction



The formation energy of oxygen vacancy $\Delta E_{\text{Vo}}\left(\text{ABO}_{3,\frac{x}{2}}\right)$ was calculated as

$$\Delta E_{\text{Vo}}\left(\text{ABO}_{3,\frac{x}{2}}\right) = E\left(\text{ABO}_{3-\frac{x}{2}}\right) - E(\text{ABO}_3) + \frac{x}{4}\mu_{\text{O}_2} \quad (6)$$

Where μ_{O_2} is the chemical potential of O_2 . The chemical potential of O_2 , H_2 , and H_2O are related as



$$\frac{x}{2}\mu_{\text{H}_2\text{O}} = x\mu_{\text{H}} + \frac{x}{4}\mu_{\text{O}_2} \quad (8)$$

By combining equation (2), (4), (6) and (8), we can find the energy of hydrogen insertion and hydration energy are related as follows

$$\begin{aligned} \Delta E_{\text{hyd}} &= \Delta H(x) + E(\text{ABO}_3) - E\left(\text{ABO}_{3-\frac{x}{2}}\right) - \frac{x}{2}\mu_{\text{H}_2\text{O}} + x\mu_{\text{H}} \\ &= \Delta H(x) - \Delta E_{\text{Vo}}\left(\text{ABO}_{3,\frac{x}{2}}\right) - \frac{x}{2}\mu_{\text{H}_2\text{O}} + \frac{x}{4}\mu_{\text{O}_2} + x\mu_{\text{H}} \\ &= \Delta H(x) - \Delta E_{\text{Vo}}\left(\text{ABO}_{3,\frac{x}{2}}\right) \end{aligned}$$

$$\Delta E_{\text{hyd}} = \Delta H(x) - \Delta E_{\text{Vo}}(\text{ABO}_3, \frac{x}{2}) \quad (9)$$

Therefore, the hydration energy is equivalent to the hydrogen insertion energy plus the formation energy of oxygen vacancy given the chemical potential of O, H, and H₂O follows the relation in Eq. (9) (Figure A3.a). We also confirm this relation using the DFT calculated energies using several example materials such as SrNiO₃, SrFeO₃, SrCoO₃ and BaFeO₃ (Figure A.3b). These analyses show that the energy of hydrogen insertion is related to the hydration energy and is a good quantity to describe the materials capability to absorb hydrogen.

Table A.5. Energy of hydrogen insertion (ΔH in eV/f.u.) and energy above hull (E_{hull} in meV/atom) of H_xABO_3 cubic perovskite compositions at different x .

Composi tion	ΔH $x = 0.125$	ΔH $x = 0.5$	ΔH $x = 0.75$	ΔH $x = 1$	E_{hull} $x = 0.125$	E_{hull} $x = 0.5$	E_{hull} $x = 0.75$	E_{hull} $x = 1$
CsBiO ₃	-0.13	-0.69	-0.97	-1.25	8	21	29	37
KHfO ₃	-0.14	-0.65	-0.96	-1.21	40	37	40	53
RbBiO ₃	-0.13	-0.58	-0.83	-1.02	0	1	10	29
BaFeO ₃	-0.20	-0.46	-0.55	-0.73	16	43	76	88
SrCoO ₃	-0.32	-0.45	-0.56	-0.67	35	96	120	139
SrFeO ₃	-0.14	-0.30	-0.43	-0.50	18	76	107	138
SrAlO ₃	-0.06	-0.29	-0.44	-0.58	65	113	143	172
RbSbO ₃	-0.09	-0.22	-0.26	-0.33	126	132	131	122
RbIrO ₃	-0.07	-0.17	-0.16	-0.27	79	157	216	252
SrNiO ₃	0.25	-0.05	-0.29	-0.46	64	100	113	135
RbOsO ₃	-0.02	0.23	0.40	0.68	138	206	244	296
KWO ₃	-0.08	0.30	0.60	0.94	49	99	138	179
SrVO ₃	0.07	0.36	0.63	0.90	15	43	68	89
RbNbO ₃	0.02	0.44	0.86	1.28	56	79	117	152
KNbO ₃	0.12	0.59	1.01	1.60	6	40	80	144
SrTiO ₃	-0.19	0.64	1.25	1.75	22	119	187	230
NaNbO ₃	0.21	0.66	1.16	1.55	31	58	109	138
BaSnO ₃	0.17	0.74	0.87	1.06	27	115	123	141
BaOsO ₃	0.22	0.81	0.80	1.18	140	258	257	322
RbTaO ₃	0.14	0.84	1.44	1.96	81	151	216	262
KTaO ₃	0.22	0.99	1.57	2.13	28	115	178	231
BaTaO ₃	0.47	1.00	1.08	1.26	114	162	135	127
BaZrO ₃	0.43	1.06	1.67	1.78	56	116	184	162
BaHfO ₃	0.45	1.20	1.68	2.09	61	142	186	214
BaNbO ₃	0.35	1.28	1.62	2.12	42	161	180	225

Table A.6. Proton migration energy barrier in selected rock-salt double B perovskites. $E_{B'}$ and $E_{B''}$ represents proton migration energy barrier near lower (B') and higher (B'') oxidation state cation respectively.

Composition (Ba ₂ B'B''O ₆)	MPID	Tolerance factor (<i>t</i>)	$E_{B'}$ [eV]	$E_{B''}$ [eV]
Ba ₂ LiOsO ₆	mp-10584	1.04	0.28	0.95
Ba ₂ YOsO ₆	mp-1078303	1.00	0.44	1.29
Ba ₂ DyReO ₆	mp-13932	0.99	0.40	0.48
Ba ₂ TmReO ₆	mp-13934	1.00	0.33	0.41
Ba ₂ MgWO ₆	mp-18986	1.03	0.25	0.69
Ba ₂ NiWO ₆	mp-504723	1.04	0.22	0.74

Table A.7. Site energy differences between site 1 and site 2 (shown in Figure 4d) at the low cationic layer B'O₂ plane (ΔE_{1-2}) in double-B layered A₂B'B''O₆ perovskites.

A-site element	B' element	Ionic radius of B' $r_{B'}$ [Å]	B'' element	Ionic radius of B'' $r_{B''}$ [Å]	Δr ($r_{B''}-r_{B'}$) [Å]	ΔE_{1-2} [eV]
Ba	In	0.62	Zr	0.72	0.10	0.00
Ba	Yb	0.87	Sb	0.76	-0.11	0.01
Ba	Dy	0.91	Mo	0.65	-0.26	0.01
Ba	Yb	0.87	Ta	0.68	-0.19	0.02
Sr	Fe	0.65	Ti	0.61	-0.04	0.02
Sr	Zn	0.74	Mo	0.65	-0.09	0.02
Ba	Ca	1.00	Bi	1.03	0.03	0.03
Ba	Y	0.90	Zr	0.72	-0.18	0.03
Ba	Lu	0.86	Mo	0.65	-0.21	0.04
Ba	Zn	0.74	Mo	0.65	-0.09	0.04
Ba	Zn	0.74	P	0.38	-0.36	0.06
Ba	Tb	0.92	Sn	0.69	-0.23	0.10
Sr	Fe	0.65	Ru	0.57	-0.08	0.10
Ba	Tb	0.92	Mo	0.65	-0.27	0.12
Sr	Fe	0.65	Co	0.53	-0.12	0.12
Ba	Y	0.90	Mo	0.65	-0.25	0.13
Ba	Ho	0.90	Mo	0.65	-0.25	0.14
Ba	Yb	0.87	Sb	0.76	-0.11	0.14
Sr	Zn	0.74	W	0.62	-0.12	0.15
Ba	Yb	0.87	U	0.89	0.02	0.16
Ba	Fe	0.65	Ta	0.68	0.04	0.16
Ba	Mg	0.72	U	0.76	0.04	0.18
Ba	Zn	0.74	W	0.62	-0.12	0.19
Ba	Tm	0.88	Mo	0.65	-0.23	0.19
Ba	Er	0.89	Mo	0.65	-0.24	0.20
Sr	Mn	0.65	Zr	0.72	0.08	0.29
Ba	Nd	0.98	Mo	0.65	-0.33	0.29
Sr	Fe	0.65	Hf	0.71	0.07	0.29
Ba	Co	0.53	Mo	0.65	0.12	0.32
Ba	Zn	0.74	Os	0.58	-0.17	0.33
Sr	Fe	0.55	Mo	0.65	0.10	0.35
Ba	Cr	0.55	Mo	0.65	0.10	0.42

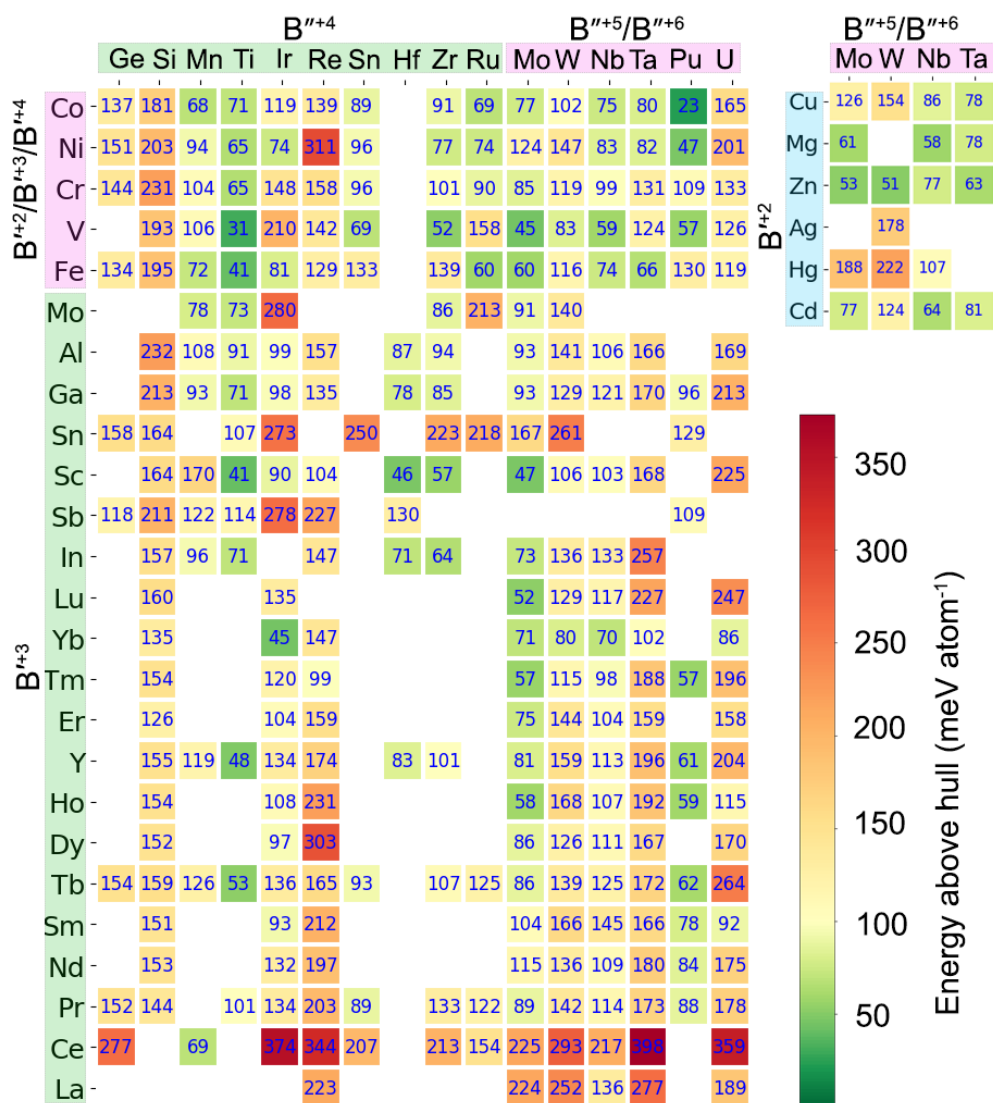


Figure A.4. The calculated energy above hull E_{hull} (color bar) of layered double-B perovskite $\text{HSr}_2\text{B}'\text{B}''\text{O}_6$ predicted by computation. The cations are arranged in ascending order of ionic radius (data in the Excel sheet of the full materials list in Supporting Information).

Table A.8. Newly predicted double-B layered perovskite composition, energy above hull (E_{hull}) and jump energy barrier (E_a) as shown in Figure 3.6.

A-site element	B' element	B'' element	E_{hull} of $A_2B'B''O_6$ H [meV/atom]	E_a (eV)
Ba	In	Ce	49	0.29
Ba	Pr	Ce	56	-
Ba	Tb	Ce	48	-
Ba	Y	Ce	48	-
Ba	Sc	Hf	40	0.25
Ba	In	Hf	34	0.34
Ba	Y	Hf	39	0.43
Ba	Mo	Hf	53	0.55
Ba	Tb	Hf	44	-
Ba	La	Mo	53	0.07
Ba	Pr	Mo	45	0.16
Ba	Ho	Mo	27	0.22
Ba	Er	Mo	28	0.22
Ba	Tb	Mo	22	0.23
Ba	Tm	Mo	29	0.23
Ba	Dy	Mo	18	0.39
Ba	Cr	Mo	58	0.64
Ba	In	Mo	19	-
Ba	Yb	Nb	50	0.13
Ba	Sc	Sn	34	0.25
Ba	Tb	Sn	31	0.48
Ba	Y	Sn	32	0.80
Ba	In	Sn	41	-
Ba	Yb	Ta	50	0.32
Ba	Sc	Ti	47	0.20
Ba	V	Ti	47	0.26
Ba	Mo	Ti	58	0.50
Ba	In	Ti	56	-
Ba	Yb	U	39	-
Ba	In	U	43	-
Ba	Yb	W	60	0.19
Ba	Sc	Zr	38	0.14
Ba	In	Zr	29	0.28
Ba	Mo	Zr	52	0.30
Ba	Y	Zr	32	0.46
Ba	V	Zr	48	0.92
Ba	Tb	Zr	35	-
Ba	Fe	Hf	47	0.17
Ba	Mn	Hf	46	0.22
Ba	Yb	Ir	58	0.39
Ba	Ce	Mn	50	0.42
Ba	Sn	Mn	48	-
Ba	Y	Mo	22	0.19
Ba	Lu	Mo	40	0.20
Ba	Tb	Mo	22	0.21
Ba	Fe	Mo	59	0.28
Ba	Sm	Mo	55	0.28

Ba	Nd	Mo	55	0.31
Ba	Pr	Mo	58	0.35
Ba	Sc	Mo	12	0.64
Ba	Co	Mo	57	0.81
Ba	Sc	Pb	39	0.34
Ba	Pr	Pb	41	-
Ba	Sn	Pb	44	-
Ba	Tb	Pb	26	-
Ba	Fe	Pb	56	-
Ba	In	Pb	53	-
Ba	Y	Pb	31	-
Ba	Bi	Pb	57	-
Ba	Fe	Sn	42	-
Ba	Mn	Ti	58	0.19
Ba	Fe	Ti	52	0.25
Ba	Mn	Zr	37	0.23
Ba	Fe	Zr	50	0.35

Effect of oxygen vacancy on proton diffusion in layered double-B perovskite

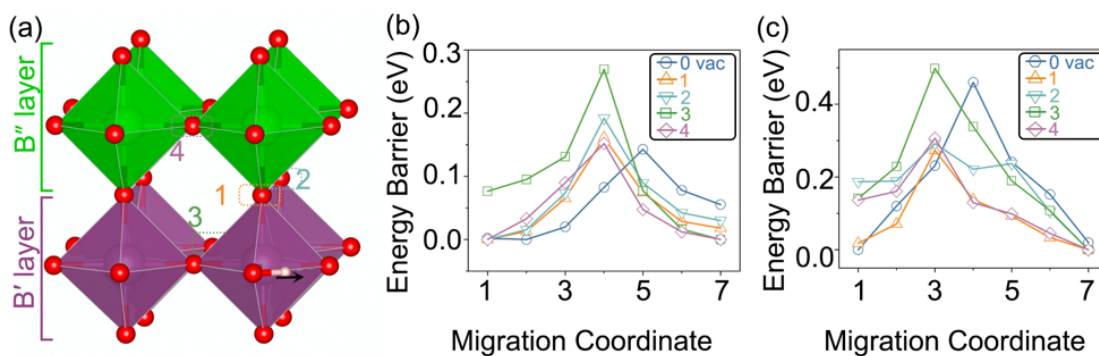


Figure A.5. (a) Proton migration path (black arrow) in layered double-B perovskite in $\text{HA}_2\text{B}'^{3+}\text{B}''^{4+}\text{O}_6$ with different oxygen vacancy positions (marked by number). Proton migration energy barrier for (b) $\text{H}_{0.5}\text{Ba}_2\text{ScZrO}_6$ (c) $\text{H}_{0.5}\text{Ba}_2\text{YZrO}_6$ at different oxygen vacancy position shown in (a).

Table A.9. Relative energy with the oxygen vacancy at different positions.

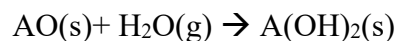
Single oxygen vacancy		Two oxygen vacancy	
Vacancy position	Relative energy (meV/f.u.)	Vacancy position	Relative energy (meV/f.u.)
4	0	1, 3	0
1 or 2	82	4, 4	2
3	88	1, 1	37

To understand oxygen vacancy distribution and their effect on proton migration in layered double-B perovskite structure, we randomly remove one or two oxygen and twice the amount hydrogen atoms from the supercell of $\text{A}_2\text{B}'\text{B}''\text{O}_6\text{H}$. For each composition or oxygen concentration of $\text{A}_2\text{B}'\text{B}''\text{O}_6\text{H}$, a total of 2000 distinct configurations of oxygen vacancy and hydrogen are sampled using *pymatgen*.¹³¹ Among these structures, 20 structures with the lowest electrostatic Ewald energy were selected to perform DFT calculations and the lowest energy structure was identified (Figure A.5a). From our calculated structures, we find an oxygen vacancy is energetically favorable at the position 4 between the B'' layer (with higher oxidation state). For two oxygen vacancies, the most favorable positions are (1, 3) and (4, 4). For

these different positions of oxygen vacancies, we calculate the proton migration energy barrier on the dominant proton migration path (Figure A.5a). We find that the position of the oxygen vacancy would affect the proton migration energy especially when it's close to the proton migration path.

The H₂O energy and the correction scheme

In this study, we set the energy of H₂O as follows.⁷⁵ We considered the hydration reaction of metal oxides



and the hydration energy $\Delta E_{\text{H}_2\text{O}}$ is calculated as

$$\Delta E_{\text{H}_2\text{O}}(\text{AO}) = E(\text{A(OH)}_2) - E(\text{AO}) - E_{\text{H}_2\text{O}}$$

where $E(\text{A(OH)}_2)$ and $E(\text{AO})$ are the formation energy of alkaline earth metal hydroxide and alkaline earth metal oxide, respectively, and $E_{\text{H}_2\text{O}}$ is the energy of H₂O. The DFT calculated $\Delta E_{\text{H}_2\text{O}}(\text{AO})$ is fitted to the experimental hydration energies of MgO, CaO, SrO, and BaO at standard conditions (1 atm pressure and 20°C) from NIST-JANAF thermochemical tables.²⁰¹ As a result, a constant shift of -0.787 eV/H₂O to the DFT energy is included in $E_{\text{H}_2\text{O}}$ to reproduce the experimental values of hydration energy.

Appendix B

Appendix B provides supplementary materials for the chapter 4, including crystal structural details, Bader charge analysis, proton migration barrier, predicted new materials, and the effect of van der Waals interactions.

Table B.1. Comparison of parameters between DFT relaxed structure and experimental structure.¹⁶³

Parameter	Experimental structure ¹⁶³	This study
Sr-Sr distance parallel to CoO ₆ octahedral plane (Å)	3.838	3.80
Sr-Sr distance normal to CoO ₆ octahedral plane (Å)	4.369	4.44
Co-Co distance in octahedral layer (Å)	3.90	3.93
Co-Co distance in pyramid layer (Å)	3.446	3.47
Volume (Å ³)	480.03	484.34

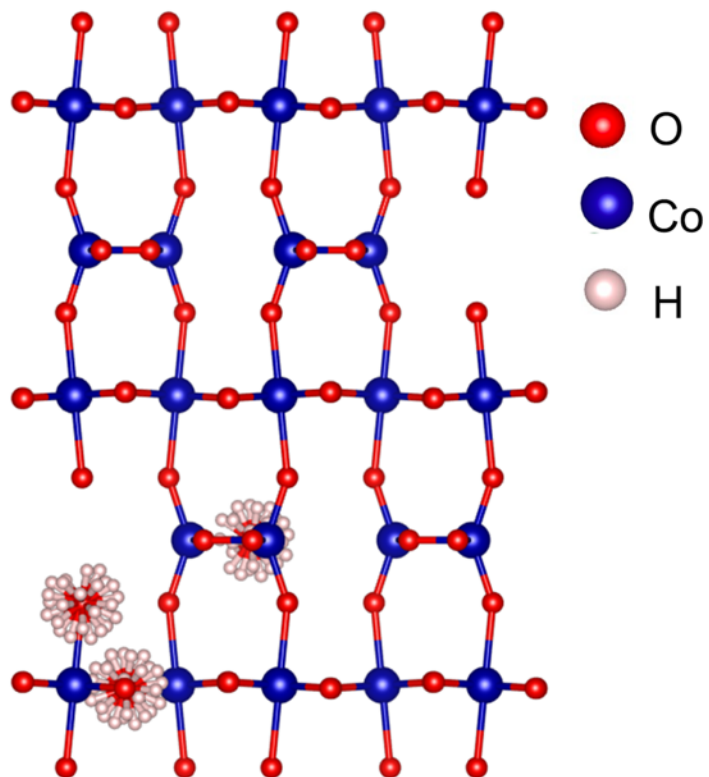


Figure B.1. SCO structure with 32 initial marked positions around each distinct oxygen site. Sr ions are not shown for clarity.

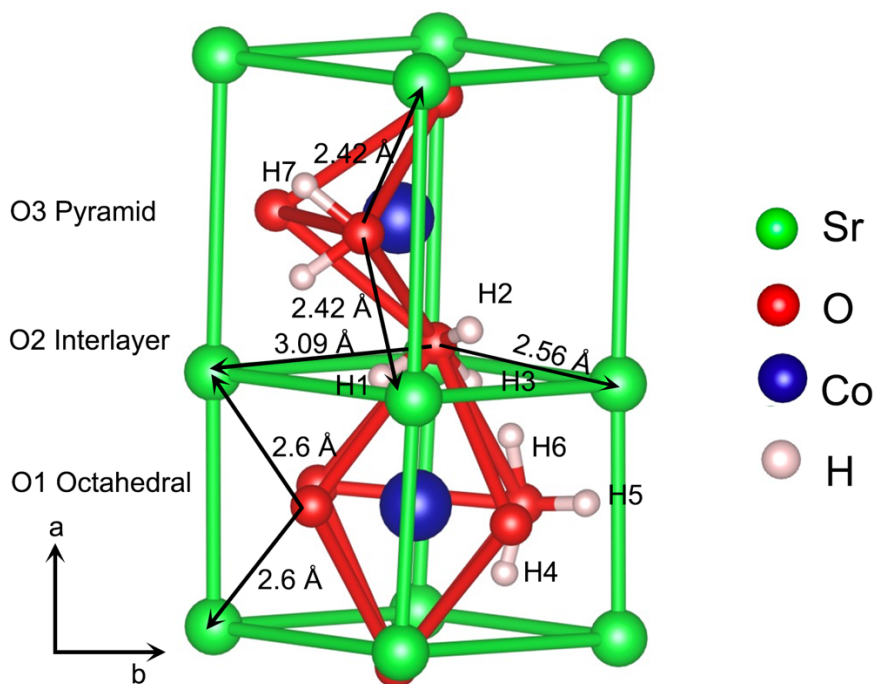


Figure B.2. Illustration of A-site Sr (green) and hydrogen sites (white) with CoO_6 octahedron and CoO_4 tetrahedron in the SCO structure. The distances of A-site Sr cations to interlayer oxygen (O2), octahedral oxygen (O1) and pyramid layer oxygen (O3) are compared. Since the interlayer O2 is off-centered in the bc plane, Sr-O2 has a larger distance of 3.09 Å along the direction of H1 site, whereas Sr-O2 is a much smaller distance of 2.56 Å along the direction of H3 site. This indicates more space for proton at H1 site and less electrostatic repulsion with Sr^{2+} cations, whereas H3 has less space and more electrostatic repulsion with Sr^{2+} . Similarly, Sr-O3, along the direction of H7 site, also has a short distance of 2.47 Å, which explains its high site energy. Therefore, the A-site Sr cations may play a significant effect on the H site energy preferences.

Table B.2. Comparison of site energy with previously reported analysis¹⁶².

Site	Previous study ¹⁶² (eV)	This study
Interlayer, site 1	0	0
Interlayer, site 2	0.04	0.06
Octahedral, site 4	0.15	0.14
Octahedral, site 6	0.19	0.2
Pyramid, site 7	0.58, 0.46	0.56

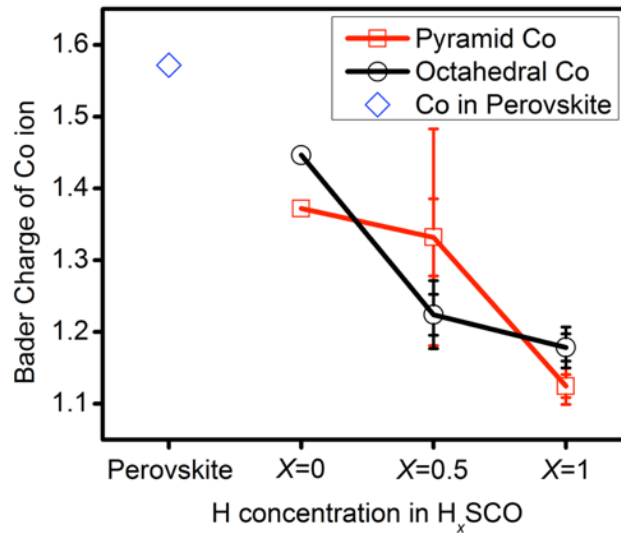


Figure B.3. Bader charge of Co in H_xSCO . Bader charge of Co in perovskite $SrCoO_3$ is higher than those in SCO and H_xSCO . The Bader charge of Co decreases with increasing H concentration.

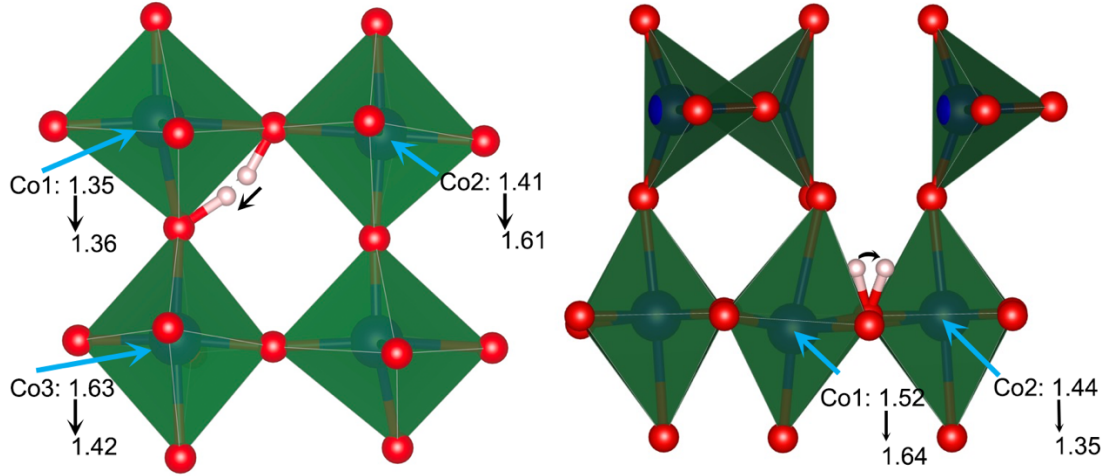


Figure B.4. The change of local Bader charge of Co (indicated by arrow) during a) proton jumps within same Co1 octahedral between O1 oxygen and b) proton rotation from Co1 octahedra to Co2 octahedra. The charge density is evaluated using hybrid exchange functional (HSE06)²⁰². For proton jump in a), the Co1 as the first nearest neighbor for proton does not change, and the electron charge on Co2 transfers to Co3. For the proton rotation in b), the electron charge transfer from Co1 to Co2.

Table B.3. Energy barrier of different proton migration pathways in $H_x\text{SCO}$ ($x=0.125, 0.25, 0.5, 0.75, 1$).

Type	Path	SCO (eV)	SCO (eV)	$H_{0.25}$	SCO (eV)	$H_{0.50}$	SCO (eV)	$H_{0.75}$	HSCO (eV)
Octahedra I/ Interlayer	1	0.21, 0.25	0.3		0.3, 0.17		0.25, 0.23		0.13, 0.31
	2	0.4, 0.41, 0.46	0.37		0.37		0.45		0.37, 0.45, 0.49
	3	0.18, 0.21	0.23		0.14		0.18		0.135, 0.18
	4	0.13, 0.26	-		-		-		0.1, 0.25
	5	0.24	-		-		-		0.26
Pyramid/ Interlayer	6	0.42, 0.66	-		-		-		0.46, 0.65, 0.9
	7	0.44	-		-		-		0.5
	8	0.65	-		-		-		0.67
	9	-	-		-		-		0.43

Table B.4. The energy barrier of proton migration at path 1 and phase stability of $\text{H}_{0.125}\text{ABO}_{2.5}$.

	Substitution element on A/B site	Energy barrier of path1 (eV)	E_{hull} (meV/atom)
	Mg	-	183
$\text{ACoO}_{2.5}$	Ca	0.22, 0.42	5
	Ba	0.5	34
	Cr	0.40	119
$\text{SrBO}_{2.5}$	Mn	0.45	30
	Ni	0.39	66
	Fe	0.32	17
	Ti	0.21	120

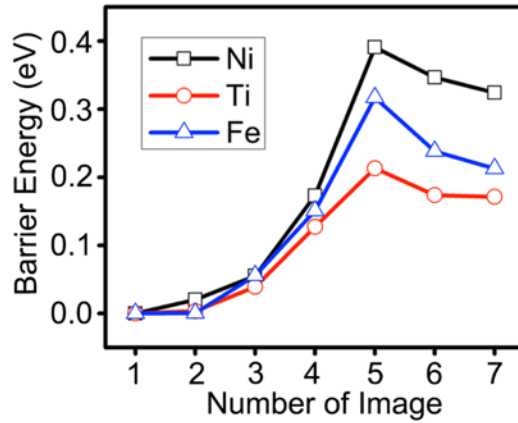


Figure B.5. Energy barrier of proton migration path 1 from interlayer H1 to octahedral H4 site in $\text{SrXO}_{2.5}$ ($X=\text{Ni}, \text{Ti}, \text{Fe}$).

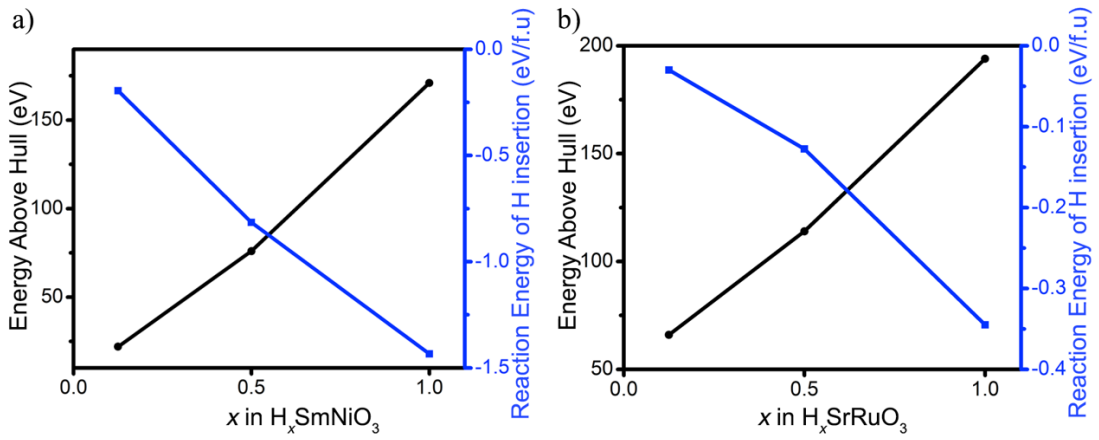


Figure B.6. Energy above hull (black) and formation energy of hydrogen insertion (blue) in a) $SmNiO_3$ and b) $SrRuO_3$.

Effects of Van der Waals interactions on proton sites

To evaluate the effect of Van der Waals interactions on O--H bond and H site energies in hydrogenated SCO, we used the semiempirical correction functional DFT-D2 and DFT-D3 from Grimme.²⁰³ This method captures the local atomic interaction from predetermined constants.^{204,205} We found the H site energies may change by 10 to 40 meV after including dispersion interactions (Table B.5), and the bond length of O--H shortens slightly by less than 0.05 Å for most H sites. We may conclude VdW correction has little effect on site energy and bond distances compared with GGA results.

Table B.5. Comparison of proton site energy and O--H bond length calculated using GGA, DFT-D2 and DFT-D3 method.

Site	GGA		DFT-D2		DFT-D3	
	Relative site energy	O--H distance (Å)	Relative site energy	O--H distance (Å)	Relative site energy	O--H distance (Å)
H1	0.00	2.19	0	2.17	0	2.12
H2	0.06	2.10	0.04	2.05	0.05	2.04
H3	0.48	2.14	0.51	2.15	0.44	2.09
H4	0.14	1.73	0.12	1.72	0.16	1.69
H5	0.30	1.59	0.29	1.59	0.32	1.56
H6	0.21	1.73	0.23	1.71	0.23	1.70
H7	0.56	1.86	0.52	1.91	0.53	1.84

Appendix C

Appendix C provides supplementary materials for the chapter 5.

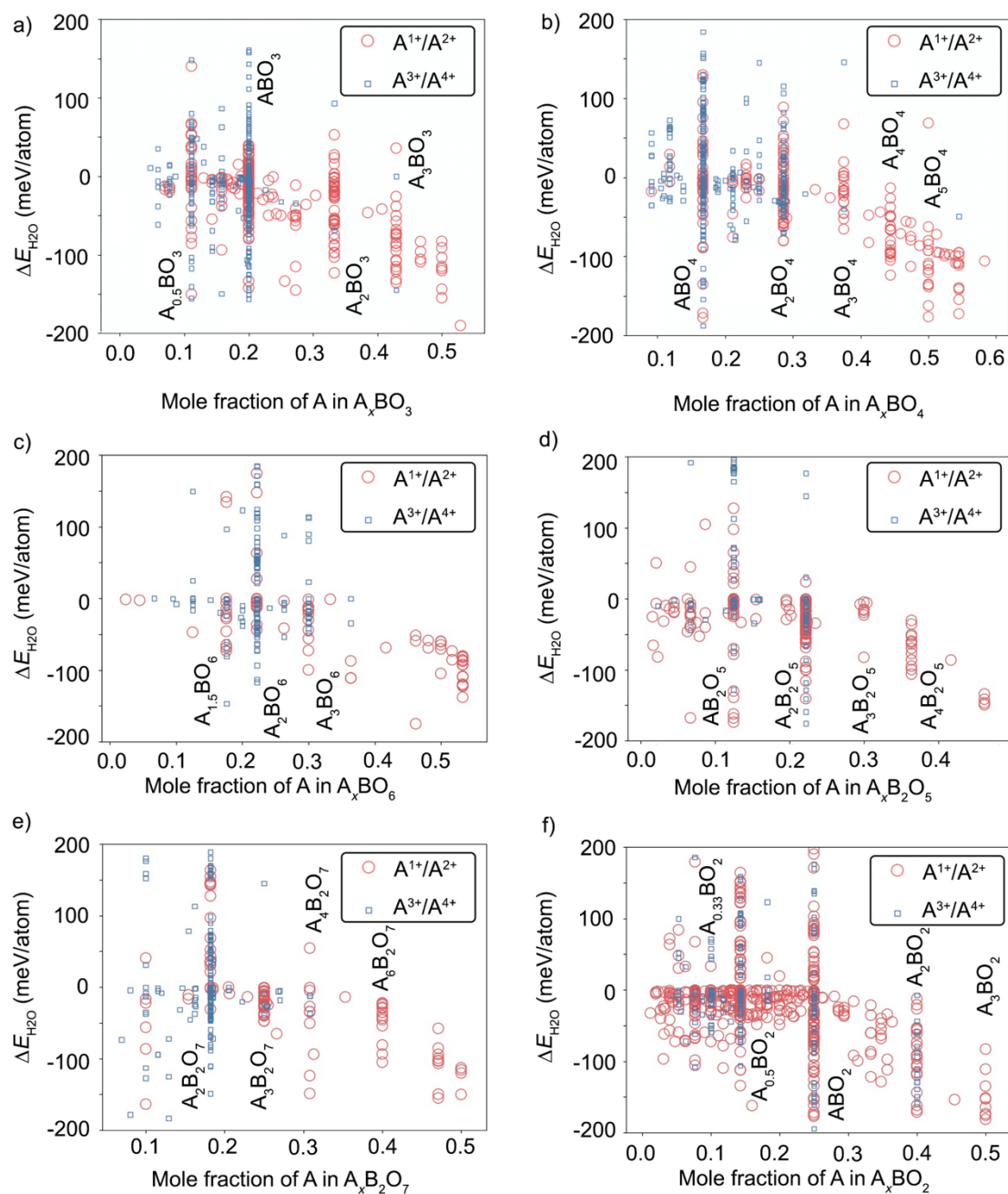


Figure C.1. Water reaction energies as a function of the mole fraction of A-cation in a) $A_x\text{BO}_3$, b) $A_x\text{BO}_4$, c) $A_x\text{BO}_6$, d) $A_x\text{B}_2\text{O}_5$, e) $A_x\text{B}_2\text{O}_7$, and f) $A_x\text{BO}_2$ formula classes. Each point represents water reaction energy of a composition.

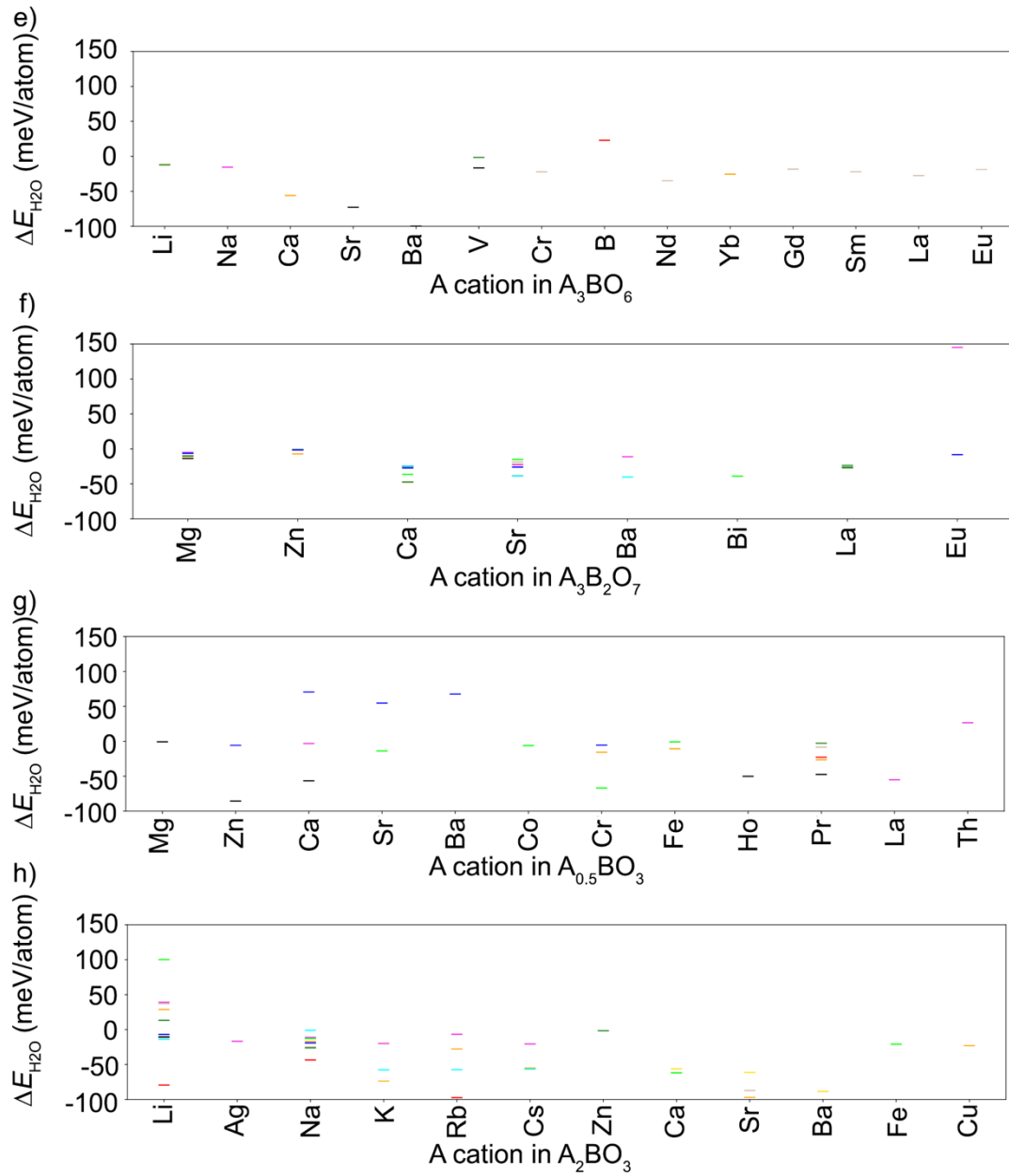


Figure C.2. Water reaction energies ($\Delta E_{\text{H}_2\text{O}}$) for the materials in a) AB_3O_6 , b) AB_2O_4 , c) ABO_2 d) A_2BO_6 , e) A_3BO_6 f) $\text{A}_3\text{B}_2\text{O}_7$ g) $\text{A}_{0.5}\text{BO}_3$, and h) A_2BO_3 formula classes. A-cations are arranged in ascending order of oxidation states from left to right.

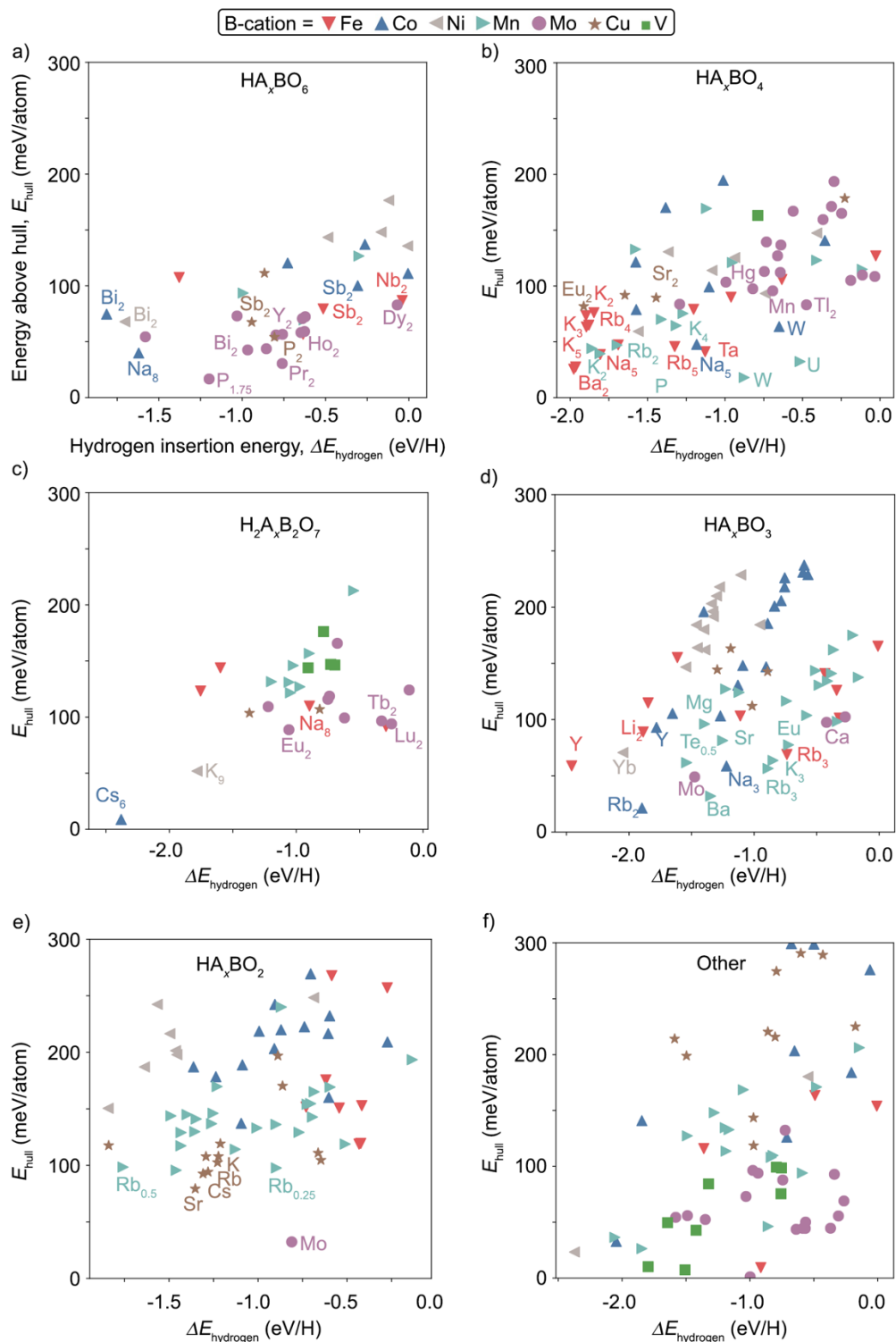


Figure C.3. The energy above hull (E_{hull}) as a function of hydrogen insertion energies for 1 H/B-cation in a) A_xBO_6 , b) A_xBO_4 , c) $\text{A}_x\text{B}_2\text{O}_7$, d) A_xBO_3 , e) A_xBO_2 , and f) rest of the formula classes.

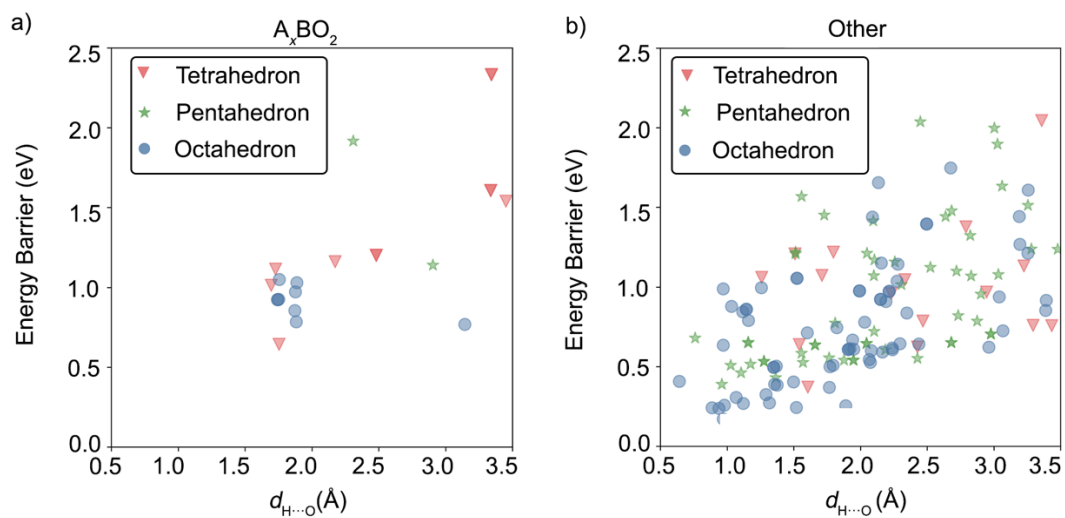


Figure C.4. The energy barrier of proton migration as a function of hydrogen bond length $d_{H\cdots O}$ for different pathways in a range of materials in a) A_xBO_2 and d) rest of the formula classes.

Bibliography

- (1) Steele, B. C. H.; Heinzl, A. Materials for Fuel-Cell Technologies. *Nature* **2001**, *414* (6861), 345–352. <https://doi.org/10.1038/35104620>.
- (2) Haile, S. M. Fuel Cell Materials and Components. *Acta Mater.* **2003**, *51* (19), 5981–6000. <https://doi.org/10.1016/j.actamat.2003.08.004>.
- (3) Kreuer, K. D. Proton-Conducting Oxides. *Annu. Rev. Mater. Res.* **2003**, *33* (1), 333–359. <https://doi.org/10.1146/annurev.matsci.33.022802.091825>.
- (4) Kreuer, K. D. Proton Conductivity: Materials and Applications. *Chem. Mater.* **1996**, *8* (3), 610–641. <https://doi.org/10.1021/cm950192a>.
- (5) Malavasi, L.; Fisher, C. A. J.; Islam, M. S. Oxide-Ion and Proton Conducting Electrolyte Materials for Clean Energy Applications: Structural and Mechanistic Features. *Chem. Soc. Rev.* **2010**, *39* (11), 4370–4387. <https://doi.org/10.1039/B915141A>.
- (6) Bi, L.; Boulfrad, S.; Traversa, E. Steam Electrolysis by Solid Oxide Electrolysis Cells (SOECs) with Proton-Conducting Oxides. *Chem. Soc. Rev.* **2014**, *43* (24), 8255–8270. <https://doi.org/10.1039/c4cs00194j>.
- (7) Vøllestad, E.; Strandbakke, R.; Tarach, M.; Catalán-Martínez, D.; Fontaine, M. L.; Beeaff, D.; Clark, D. R.; Serra, J. M.; Norby, T. Mixed Proton and Electron Conducting Double Perovskite Anodes for Stable and Efficient Tubular Proton Ceramic Electrolysers. *Nat. Mater.* **2019**, *18* (7), 752–759. <https://doi.org/10.1038/s41563-019-0388-2>.
- (8) Irvine, J. T. S.; Neagu, D.; Verbraeken, M. C.; Chatzichristodoulou, C.; Graves, C.; Mogensen, M. B. Evolution of the Electrochemical Interface in High-

- Temperature Fuel Cells and Electrolysers. *Nat. Energy* **2016**, *1* (1), 15014.
<https://doi.org/10.1038/nenergy.2015.14>.
- (9) Yang, X.; Han, J.; Yu, J.; Chen, Y.; Zhang, H.; Ding, M.; Jia, C.; Sun, J.; Sun, Q.; Wang, Z. L. Versatile Triboiontronic Transistor via Proton Conductor. *ACS Nano* **2020**, *14* (7), 8668–8677. <https://doi.org/10.1021/acsnano.0c03030>.
- (10) Herlogsson, L.; Crispin, X.; Robinson, N. D.; Sandberg, M.; Hagel, O. J.; Gustafsson, G.; Berggren, M. Low-Voltage Polymer Field-Effect Transistors Gated via a Proton Conductor. *Adv. Mater.* **2007**, *19* (1), 97–101.
<https://doi.org/10.1002/adma.200600871>.
- (11) Mercier, V. M. M.; Van der Sluis, P. Toward Solid-State Switchable Mirrors Using a Zirconium Oxide Proton Conductor. *Solid State Ionics* **2001**, *145* (1–4), 17–24. [https://doi.org/10.1016/S0167-2738\(01\)00906-7](https://doi.org/10.1016/S0167-2738(01)00906-7).
- (12) Zhu, L. Q.; Wan, C. J.; Guo, L. Q.; Shi, Y.; Wan, Q. Artificial Synapse Network on Inorganic Proton Conductor for Neuromorphic Systems. *Nat. Commun.* **2014**, *5*. <https://doi.org/10.1038/ncomms4158>.
- (13) Wan, C. J.; Zhu, L. Q.; Zhou, J. M.; Shi, Y.; Wan, Q. Memory and Learning Behaviors Mimicked in Nanogranular SiO₂-Based Proton Conductor Gated Oxide-Based Synaptic Transistors. *Nanoscale* **2013**, *5* (21), 10194–10199.
<https://doi.org/10.1039/c3nr02987e>.
- (14) Wen, J.; Zhu, L. Q.; Qi, H. F.; Ren, Z. Y.; Wang, F.; Xiao, H. Brain-Inspired Biodegradable Pectin Based Proton Conductor Gated Electronic Synapse. *Org. Electron.* **2020**, *82* (April), 105782.
<https://doi.org/10.1016/j.orgel.2020.105782>.

- (15) Schober, T. Applications of Oxidic High-Temperature Proton Conductors. *Solid State Ionics* **2003**, *162–163*, 277–281. [https://doi.org/10.1016/S0167-2738\(03\)00241-8](https://doi.org/10.1016/S0167-2738(03)00241-8).
- (16) Wan, C. J.; Zhu, L. Q.; Wan, X.; Shi, Y.; Wan, Q. Organic/Inorganic Hybrid Synaptic Transistors Gated by Proton Conducting Methylcellulose Films. *Appl. Phys. Lett.* **2016**, *108* (4). <https://doi.org/10.1063/1.4941080>.
- (17) Cheng, W.; Liang, R.; Tian, H.; Sun, C.; Jiang, C.; Wang, X.; Wang, J.; Ren, T. L.; Xu, J. Proton Conductor Gated Synaptic Transistor Based on Transparent IGZO for Realizing Electrical and UV Light Stimulus. *IEEE J. Electron Devices Soc.* **2019**, *7* (March), 38–45. <https://doi.org/10.1109/JEDS.2018.2875976>.
- (18) Zhong, C.; Deng, Y.; Roudsari, A. F.; Kapetanovic, A.; Anantram, M. P.; Rolandi, M. A Polysaccharide Bioprotonic Field-Effect Transistor. *Nat. Commun.* **2011**, *2* (1), 2–6. <https://doi.org/10.1038/ncomms1489>.
- (19) Wen, J.; Zhu, L. Q.; Fu, Y. M.; Xiao, H.; Guo, L. Q.; Wan, Q. Activity Dependent Synaptic Plasticity Mimicked on Indium-Tin-Oxide Electric-Double-Layer Transistor. *ACS Appl. Mater. Interfaces* **2017**, *9* (42), 37064–37069. <https://doi.org/10.1021/acsami.7b13215>.
- (20) Yuan, H.; Shimotani, H.; Tsukazaki, A.; Ohtomo, A.; Kawasaki, M.; Iwasa, Y. Hydrogenation-Induced Surface Polarity Recognition and Proton Memory Behavior at Protic-Ionic-Liquid/Oxide Electric-Double-Layer Interfaces. *J. Am. Chem. Soc.* **2010**, *132* (19), 6672–6678. <https://doi.org/10.1021/ja909110s>.
- (21) Zhu, L. Q.; Sun, J.; Wu, G. D.; Zhang, H. L.; Wan, Q. Self-Assembled Dual in-Plane Gate Thin-Film Transistors Gated by Nanogranular SiO₂ Proton

- Conductors for Logic Applications. *Nanoscale* **2013**, *5* (5), 1980–1985.
<https://doi.org/10.1039/c3nr33734k>.
- (22) Zhang, H.; Guo, L.; Wan, Q. Nanogranular Al₂O₃ Proton Conducting Films for Low-Voltage Oxide-Based Homojunction Thin-Film Transistors. *J. Mater. Chem. C* **2013**, *1* (15), 2781–2786. <https://doi.org/10.1039/c3tc30137k>.
- (23) Kapetanakis, E.; Douvas, A. M.; Velessiotis, D.; Makarona, E.; Argitis, P.; Glezos, N.; Normand, P. Molecular Storage Elements for Proton Memory Devices. *Adv. Mater.* **2008**, *20* (23), 4568–4574.
<https://doi.org/10.1002/adma.200801104>.
- (24) Li, F.; Tao, Z.; Dai, H.; Xi, X.; Ding, H. A High-Performing Proton-Conducting Solid Oxide Fuel Cell with Layered Perovskite Cathode in Intermediate Temperatures. *Int. J. Hydrogen Energy* **2018**, *43* (42), 19757–19762.
<https://doi.org/https://doi.org/10.1016/j.ijhydene.2018.09.022>.
- (25) Fabbri, E.; Bi, L.; Pergolesi, D.; Traversa, E. Towards the Next Generation of Solid Oxide Fuel Cells Operating Below 600 °C with Chemically Stable Proton-Conducting Electrolytes. *Adv. Mater.* **2012**, *24* (2), 195–208.
<https://doi.org/https://doi.org/10.1002/adma.201103102>.
- (26) Boudghene Stambouli, A.; Traversa, E. Fuel Cells, an Alternative to Standard Sources of Energy. *Renew. Sustain. Energy Rev.* **2002**, *6* (3), 295–304.
[https://doi.org/https://doi.org/10.1016/S1364-0321\(01\)00015-6](https://doi.org/https://doi.org/10.1016/S1364-0321(01)00015-6).
- (27) Hossain, S.; Abdalla, A. M.; Jamain, S. N. B.; Zaini, J. H.; Azad, A. K. A Review on Proton Conducting Electrolytes for Clean Energy and Intermediate Temperature-Solid Oxide Fuel Cells. *Renew. Sustain. Energy Rev.* **2017**, *79*,

- 750–764. <https://doi.org/https://doi.org/10.1016/j.rser.2017.05.147>.
- (28) Song, M.-K.; Kim, Y.-T.; Fenton, J. M.; Kunz, H. R.; Rhee, H.-W. Chemically-Modified Nafion®/Poly(Vinylidene Fluoride) Blend Ionomers for Proton Exchange Membrane Fuel Cells. *J. Power Sources* **2003**, *117* (1), 14–21. [https://doi.org/https://doi.org/10.1016/S0378-7753\(03\)00166-6](https://doi.org/https://doi.org/10.1016/S0378-7753(03)00166-6).
- (29) Sasikala, S.; Selvaganesh, S. V.; Sahu, A. K.; Carbone, A.; Passalacqua, E. Block Co-Polymer Templated Mesoporous Carbon–Nafion Hybrid Membranes for Polymer Electrolyte Fuel Cells under Reduced Relative Humidity. *J. Memb. Sci.* **2016**, *499*, 503–514. <https://doi.org/https://doi.org/10.1016/j.memsci.2015.11.011>.
- (30) Liu, F.; Yi, B.; Xing, D.; Yu, J.; Zhang, H. Nafion/PTFE Composite Membranes for Fuel Cell Applications. *J. Memb. Sci.* **2003**, *212* (1), 213–223. [https://doi.org/https://doi.org/10.1016/S0376-7388\(02\)00503-3](https://doi.org/https://doi.org/10.1016/S0376-7388(02)00503-3).
- (31) Duan, C.; Tong, J.; Shang, M.; Nikodemski, S.; Sanders, M.; Ricote, S.; Almansoori, A.; O’Hayre, R. Readily Processed Protonic Ceramic Fuel Cells with High Performance at Low Temperatures. *Science (80-.)*. **2015**, *349* (6254), 1321 LP – 1326. <https://doi.org/10.1126/science.aab3987>.
- (32) Nguyen, N. T. Q.; Yoon, H. H. Preparation and Evaluation of BaZr_{0.1}Ce_{0.7}Y_{0.1}Yb_{0.1}O_{3-δ} (BZCYYb) Electrolyte and BZCYYb-Based Solid Oxide Fuel Cells. *J. Power Sources* **2013**, *231*, 213–218. <https://doi.org/https://doi.org/10.1016/j.jpowsour.2013.01.011>.
- (33) Bae, K.; Jang, D. Y.; Choi, H. J.; Kim, D.; Hong, J.; Kim, B.-K.; Lee, J.-H.; Son, J.-W.; Shim, J. H. Demonstrating the Potential of Yttrium-Doped Barium

- Zirconate Electrolyte for High-Performance Fuel Cells. *Nat. Commun.* **2017**, *8* (1), 14553. <https://doi.org/10.1038/ncomms14553>.
- (34) Zhang, L.; Yao, F.; Meng, J.; Zhang, W.; Wang, H.; Liu, X.; Meng, J.; Zhang, H. Oxygen Migration and Proton Diffusivity in Transition-Metal (Mn, Fe, Co, and Cu) Doped Ruddlesden-Popper Oxides. *J. Mater. Chem. A* **2019**, *7* (31), 18558–18567. <https://doi.org/10.1039/c9ta05893a>.
- (35) Zuo, C.; Zha, S.; Liu, M.; Hatano, M.; Uchiyama, M. Ba(Zr_{0.1}Ce_{0.7}Y_{0.2})O_{3-δ} as an Electrolyte for Low-Temperature Solid-Oxide Fuel Cells. *Adv. Mater.* **2006**, *18* (24), 3318–3320. <https://doi.org/https://doi.org/10.1002/adma.200601366>.
- (36) Tao, Z.; Bi, L.; Zhu, Z.; Liu, W. Novel Cobalt-Free Cathode Materials BaCexFe_{1-x}O_{3-δ} for Proton-Conducting Solid Oxide Fuel Cells. *J. Power Sources* **2009**, *194* (2), 801–804. <https://doi.org/https://doi.org/10.1016/j.jpowsour.2009.06.071>.
- (37) Zhao, L.; He, B.; Nian, Q.; Xun, Z.; Peng, R.; Meng, G.; Liu, X. In Situ Drop-Coated BaZr_{0.1}Ce_{0.7}Y_{0.2}O_{3-δ} Electrolyte-Based Proton-Conductor Solid Oxide Fuel Cells with a Novel Layered PrBaCuFeO_{5+δ} Cathode. *J. Power Sources* **2009**, *194* (1), 291–294. <https://doi.org/https://doi.org/10.1016/j.jpowsour.2009.05.001>.
- (38) Zhao, L.; He, B.; Lin, B.; Ding, H.; Wang, S.; Ling, Y.; Peng, R.; Meng, G.; Liu, X. High Performance of Proton-Conducting Solid Oxide Fuel Cell with a Layered PrBaCo₂O_{5+δ} Cathode. *J. Power Sources* **2009**, *194* (2), 835–837. <https://doi.org/https://doi.org/10.1016/j.jpowsour.2009.06.010>.

- (39) Lin, B.; Dong, Y.; Yan, R.; Zhang, S.; Hu, M.; Zhou, Y.; Meng, G. In Situ Screen-Printed BaZr_{0.1}Ce_{0.7}Y_{0.2}O_{3-δ} Electrolyte-Based Protonic Ceramic Membrane Fuel Cells with Layered SmBaCo₂O_{5+x} Cathode. *J. Power Sources* **2009**, *186* (2), 446–449. <https://doi.org/https://doi.org/10.1016/j.jpowsour.2008.09.120>.
- (40) Fabbri, E.; Pergolesi, D.; Traversa, E. Materials Challenges toward Proton-Conducting Oxide Fuel Cells: A Critical Review. *Chem. Soc. Rev.* **2010**, *39* (11), 4355–4369. <https://doi.org/10.1039/B902343G>.
- (41) Lu, N.; Zhang, P.; Zhang, Q.; Qiao, R.; He, Q.; Li, H. B.; Wang, Y.; Guo, J.; Zhang, D.; Duan, Z.; Li, Z.; Wang, M.; Yang, S.; Yan, M.; Arenholz, E.; Zhou, S.; Yang, W.; Gu, L.; Nan, C. W.; Wu, J.; Tokura, Y.; Yu, P. Electric-Field Control of Tri-State Phase Transformation with a Selective Dual-Ion Switch. *Nature* **2017**, *546* (7656), 124–128. <https://doi.org/10.1038/nature22389>.
- (42) Rashid, N. L. R. M.; Samat, A. A.; Jais, A. A.; Somalu, M. R.; Muchtar, A.; Baharuddin, N. A.; Wan Isahak, W. N. R. Review on Zirconate-Cerate-Based Electrolytes for Proton-Conducting Solid Oxide Fuel Cell. *Ceram. Int.* **2019**, *45* (6), 6605–6615. <https://doi.org/https://doi.org/10.1016/j.ceramint.2019.01.045>.
- (43) Sawant, P.; Varma, S.; Wani, B. N.; Bharadwaj, S. R. Synthesis, Stability and Conductivity of BaCe_{0.8-x}Zr_xY_{0.2}O_{3-δ} as Electrolyte for Proton Conducting SOFC. *Int. J. Hydrogen Energy* **2012**, *37* (4), 3848–3856. <https://doi.org/https://doi.org/10.1016/j.ijhydene.2011.04.106>.
- (44) Azad, A. K.; Irvine, J. T. S. Synthesis, Chemical Stability and Proton Conductivity of the Perovskites Ba(Ce,Zr)_{1-x}Sc_xO_{3-δ}. *Solid State Ionics*

2007, 178 (7), 635–640.
<https://doi.org/https://doi.org/10.1016/j.ssi.2007.02.004>.

- (45) Wang, H.; Peng, R.; Wu, X.; Hu, J.; Xia, C. Sintering Behavior and Conductivity Study of Yttrium-Doped BaCeO₃–BaZrO₃ Solid Solutions Using ZnO Additives. *J. Am. Ceram. Soc.* **2009**, *92* (11), 2623–2629. <https://doi.org/https://doi.org/10.1111/j.1551-2916.2009.03204.x>.
- (46) LÜ, J.; WANG, L.; FAN, L.; LI, Y.; DAI, L.; GUO, H. Chemical Stability of Doped BaCeO₃-BaZrO₃ Solid Solutions in Different Atmospheres. *J. Rare Earths* **2008**, *26* (4), 505–510. [https://doi.org/https://doi.org/10.1016/S1002-0721\(08\)60127-1](https://doi.org/https://doi.org/10.1016/S1002-0721(08)60127-1).
- (47) Yamazaki, Y.; Hernandez-Sanchez, R.; Haile, S. M. High Total Proton Conductivity in Large-Grained Yttrium-Doped Barium Zirconate. *Chem. Mater.* **2009**, *21* (13), 2755–2762. <https://doi.org/10.1021/cm900208w>.
- (48) Babilo, P.; Uda, T.; Haile, S. M. Processing of Yttrium-Doped Barium Zirconate for High Proton Conductivity. *J. Mater. Res.* **2007**, *22* (5), 1322–1330. [https://doi.org/DOI: 10.1557/jmr.2007.0163](https://doi.org/DOI:10.1557/jmr.2007.0163).
- (49) Zajac, W.; Rusinek, D.; Zheng, K.; Molenda, J. Applicability of Gd-Doped BaZrO₃, SrZrO₃, BaCeO₃ and SrCeO₃ Proton Conducting Perovskites as Electrolytes for Solid Oxide Fuel Cells. *Cent. Eur. J. Chem.* **2013**, *11* (4), 471–484. <https://doi.org/10.2478/s11532-012-0144-9>.
- (50) Ahmed, I.; Eriksson, S. G.; Ahlberg, E.; Knee, C. S.; Götlind, H.; Johansson, L. G.; Karlsson, M.; Matic, A.; Börjesson, L. Structural Study and Proton Conductivity in Yb-Doped BaZrO₃. *Solid State Ionics* **2007**, *178* (7–10), 515–

520. <https://doi.org/10.1016/j.ssi.2006.11.011>.
- (51) Ahmed, I.; Eriksson, S. G.; Ahlberg, E.; Knee, C. S.; Karlsson, M.; Matic, A.; Engberg, D.; Börjesson, L. Proton Conductivity and Low Temperature Structure of In-Doped BaZrO₃. *Solid State Ionics* **2006**, *177* (26-32 SPEC. ISS.), 2357–2362. <https://doi.org/10.1016/j.ssi.2006.05.030>.
- (52) Fisher, C. Defect, Protons and Conductivity in Brownmillerite-Structured Ba₂In₂O₅. *Solid State Ionics* **1999**, *118* (3–4), 355–363. [https://doi.org/10.1016/S0167-2738\(98\)00391-9](https://doi.org/10.1016/S0167-2738(98)00391-9).
- (53) Glöckner, R.; Islam, M. S.; Norby, T. Protons and Other Defects in BaCeO₃: A Computational Study. *Solid State Ionics* **1999**, *122* (1–4), 145–156. [https://doi.org/10.1016/S0167-2738\(99\)00070-3](https://doi.org/10.1016/S0167-2738(99)00070-3).
- (54) Kreuer, K. D. Aspects of the Formation and Mobility of Protonic Charge Carriers and the Stability of Perovskite-Type Oxides. *Solid State Ionics* **1999**, *125* (1), 285–302. [https://doi.org/https://doi.org/10.1016/S0167-2738\(99\)00188-5](https://doi.org/10.1016/S0167-2738(99)00188-5).
- (55) Yamazaki, Y.; Blanc, F.; Okuyama, Y.; Buannic, L.; Lucio-Vega, J. C.; Grey, C. P.; Haile, S. M. Proton Trapping in Yttrium-Doped Barium Zirconate. *Nat. Mater.* **2013**, *12* (7), 647–651. <https://doi.org/10.1038/nmat3638>.
- (56) Draber, F. M.; Ader, C.; Arnold, J. P.; Eisele, S.; Grieshammer, S.; Yamaguchi, S.; Martin, M. Nanoscale Percolation in Doped BaZrO₃ for High Proton Mobility. *Nat. Mater.* **2020**, *19* (3), 338–346. <https://doi.org/10.1038/s41563-019-0561-7>.
- (57) Gomez, M. A.; Griffin, M. A.; Jindal, S.; Rule, K. D.; Cooper, V. R. The Effect

- of Octahedral Tilting on Proton Binding Sites and Transition States in Pseudo-Cubic Perovskite Oxides. *J. Chem. Phys.* **2005**, *123* (9).
<https://doi.org/10.1063/1.2035099>.
- (58) Stokes, S. J.; Islam, M. S. Defect Chemistry and Proton-Dopant Association in BaZrO₃ and BaPrO₃. *J. Mater. Chem.* **2010**, *20* (30), 6258–6264.
<https://doi.org/10.1039/c0jm00328j>.
- (59) Saiful Islam, M. Ionic Transport in ABO₃ Perovskite Oxides: A Computer Modelling Tour. *J. Mater. Chem.* **2000**, *10* (4), 1027–1038.
<https://doi.org/10.1039/A908425H>.
- (60) Toyoura, K.; Meng, W.; Han, D.; Uda, T. Preferential Proton Conduction along a Three-Dimensional Dopant Network in Yttrium-Doped Barium Zirconate: A First-Principles Study. *J. Mater. Chem. A* **2018**, *6* (45), 22721–22730.
<https://doi.org/10.1039/C8TA08283A>.
- (61) Islam, M. S.; Slater, P. R.; Tolchard, J. R.; Dinges, T. Doping and Defect Association in AZrO₃ (A = Ca, Ba) and LaMO₃ (M = Sc, Ga) Perovskite-Type Ionic Conductors. *Dalt. Trans.* **2004**, No. 19, 3061–3066.
<https://doi.org/10.1039/B402669C>.
- (62) Stokes, S. J.; Islam, M. S. Defect Chemistry and Proton-Dopant Association in BaZrO₃ and BaPrO₃. *J. Mater. Chem.* **2010**, *20* (30), 6258–6264.
<https://doi.org/10.1039/C0JM00328J>.
- (63) Björketun, M. E.; Sundell, P. G.; Wahnström, G.; Engberg, D. A Kinetic Monte Carlo Study of Proton Diffusion in Disordered Perovskite Structured Lattices Based on First-Principles Calculations. *Solid State Ionics* **2005**, *176* (39), 3035–

3040. <https://doi.org/https://doi.org/10.1016/j.ssi.2005.09.044>.
- (64) Björketun, M. E.; Sundell, P. G.; Wahnström, G. Effect of Acceptor Dopants on the Proton Mobility in BaZrO₃: A Density Functional Investigation. *Phys. Rev. B* **2007**, *76* (5), 54307. <https://doi.org/10.1103/PhysRevB.76.054307>.
- (65) Yamazaki, Y.; Kuwabara, A.; Hyodo, J.; Okuyama, Y.; Fisher, C. A. J.; Haile, S. M. Oxygen Affinity: The Missing Link Enabling Prediction of Proton Conductivities in Doped Barium Zirconates. *Chem. Mater.* **2020**, *32* (17), 7292–7300. <https://doi.org/10.1021/acs.chemmater.0c01869>.
- (66) Ding, H.; Wu, W.; Jiang, C.; Ding, Y.; Bian, W.; Hu, B.; Singh, P.; Orme, C. J.; Wang, L.; Zhang, Y.; Ding, D. Self-Sustainable Protonic Ceramic Electrochemical Cells Using a Triple Conducting Electrode for Hydrogen and Power Production. *Nat. Commun.* **2020**, *11* (1). <https://doi.org/10.1038/s41467-020-15677-z>.
- (67) Kaus, I.; Wiik, K.; Krogh, B.; Dahle, M.; Hofstad, K. H.; Aasland, S. Stability of SrFeO₃-Based Materials in H₂O/CO₂-Containing Atmospheres at High Temperatures and Pressures. *J. Am. Ceram. Soc.* **2007**, *90* (7), 2226–2230. <https://doi.org/10.1111/j.1551-2916.2007.01727.x>.
- (68) Bork, N.; Bonanos, N.; Rossmeis, J.; Vegge, T. Simple Descriptors for Proton-Conducting Perovskites from Density Functional Theory. *Phys. Rev. B* **2010**, *82* (1), 14103. <https://doi.org/10.1103/PhysRevB.82.014103>.
- (69) Li, X.; Wang, H.; Cui, Z.; Li, Y.; Xin, S.; Zhou, J.; Long, Y.; Jin, C.; Goodenough, J. B. Exceptional Oxygen Evolution Reactivities on CaCoO₃ and SrCoO₃. *Sci. Adv.* **2019**, *5* (8), 3–10. <https://doi.org/10.1126/sciadv.aav6262>.

- (70) Islam, M. S.; Nolan, A. M.; Wang, S.; Bai, Q.; Mo, Y. A Computational Study of Fast Proton Diffusion in Brownmillerite $\text{Sr}_2\text{Co}_2\text{O}_5$. *Chem. Mater.* **2020**, *32* (12), 5028–5035. <https://doi.org/10.1021/acs.chemmater.0c00544>.
- (71) Zhou, Y.; Guan, X.; Zhou, H.; Ramadoss, K.; Adam, S.; Liu, H.; Lee, S.; Shi, J.; Tsuchiya, M.; Fong, D. D.; Ramanathan, S. Strongly Correlated Perovskite Fuel Cells. *Nature* **2016**, *534* (7606), 231–234. <https://doi.org/10.1038/nature17653>.
- (72) Li, Z.; Shen, S.; Tian, Z.; Hwangbo, K.; Wang, M.; Wang, Y.; Bartram, F. M.; He, L.; Lyu, Y.; Dong, Y.; Wan, G.; Li, H.; Lu, N.; Zang, J.; Zhou, H.; Arenholz, E.; He, Q.; Yang, L.; Luo, W.; Yu, P. Reversible Manipulation of the Magnetic State in SrRuO_3 through Electric-Field Controlled Proton Evolution. *Nat. Commun.* **2020**, *11* (1), 184. <https://doi.org/10.1038/s41467-019-13999-1>.
- (73) Hermet, J.; Torrent, M.; Bottin, F.; Dezanneau, G.; Geneste, G. Hydrogen Diffusion in the Protonic Conductor $\text{BaCe}_{1-x}\text{Gd}_x\text{SO}_3$ from Density Functional Theory. *Phys. Rev. B* **2013**, *87* (10), 104303. <https://doi.org/10.1103/PhysRevB.87.104303>.
- (74) Kalinina, M. V.; Arsent'ev, M. Y.; Kotlyarov, N. S.; Fedorenko, N. Y.; Tikhonov, P. A.; Shilova, O. A. Synthesis and Research Using Computer Simulation of Proton-Conducting Solid Electrolytes Based on Hafnate and Barium Zirconate. *Glas. Phys. Chem.* **2021**, *47* (4), 366–371. <https://doi.org/10.1134/S1087659621040106>.
- (75) Islam, M. S.; Wang, S.; Nolan, A. M.; Mo, Y. First-Principles Computational

- Design and Discovery of Novel Double-Perovskite Proton Conductors. *Chem. Mater.* **2021**. <https://doi.org/10.1021/acs.chemmater.1c02432>.
- (76) Kreuer, K. D. On the Development of Proton Conducting Materials for Technological Applications. *Solid State Ionics* **1997**, *97* (1), 1–15. [https://doi.org/10.1016/S0167-2738\(97\)00082-9](https://doi.org/10.1016/S0167-2738(97)00082-9).
- (77) Kim, J.; Jun, A.; Gwon, O.; Yoo, S.; Liu, M.; Shin, J.; Lim, T.-H.; Kim, G. Hybrid-Solid Oxide Electrolysis Cell: A New Strategy for Efficient Hydrogen Production. *Nano Energy* **2018**, *44*, 121–126. <https://doi.org/10.1016/j.nanoen.2017.11.074>.
- (78) Wang, N.; Hinokuma, S.; Ina, T.; Zhu, C.; Habazaki, H.; Aoki, Y. Mixed Proton–Electron–Oxide Ion Triple Conducting Manganite as an Efficient Cobalt-Free Cathode for Protonic Ceramic Fuel Cells. *J. Mater. Chem. A* **2020**, *8* (21), 11043–11055. <https://doi.org/10.1039/D0TA03899G>.
- (79) da Silva, F. S.; de Souza, T. M. Novel Materials for Solid Oxide Fuel Cell Technologies: A Literature Review. *Int. J. Hydrogen Energy* **2017**, *42* (41), 26020–26036. <https://doi.org/10.1016/j.ijhydene.2017.08.105>.
- (80) Bork, N. DFT Modelling of Oxide Materials for Hydrogen Permeable Membranes. **2010**, No. September.
- (81) Huang, Y.-H.; Dass, R. I.; Xing, Z.-L.; Goodenough, J. B. Double Perovskites as Anode Materials for Solid-Oxide Fuel Cells. *Science* (80-.). **2006**, *312* (5771), 254 LP – 257. <https://doi.org/10.1126/science.1125877>.
- (82) Huang, Y.-H.; Liang, G.; Croft, M.; Lehtimäki, M.; Karppinen, M.; Goodenough, J. B. Double-Perovskite Anode Materials Sr₂MMoO₆ (M = Co,

- Ni) for Solid Oxide Fuel Cells. *Chem. Mater.* **2009**, *21* (11), 2319–2326. <https://doi.org/10.1021/cm8033643>.
- (83) Korona, D. V.; Ivanova, I. V.; Obruchova, A. V.; Sharafutdinov, A. R.; Animitsa, I. E. Proton Conductivity and the Thermal Properties of Ba₂CeZnO₅. *Bull. Russ. Acad. Sci. Phys.* **2017**, *81* (5), 628–631. <https://doi.org/10.3103/s1062873817050124>.
- (84) Halwidl, D.; Mayr-Schmölzer, W.; Fobes, D.; Peng, J.; Mao, Z.; Schmid, M.; Mittendorfer, F.; Redinger, J.; Diebold, U. Ordered Hydroxyls on Ca₃Ru₂O₇(001). *Nat. Commun.* **2017**, *8* (1), 1–7. <https://doi.org/10.1038/s41467-017-00066-w>.
- (85) Goodenough, J. B. Oxide-Ion Conduction in BaIn₂O₅ and BaInM₈ (M = Ce , Hf , or Zr). *Solid State Ionics* **1990**, *44*, 21–31.
- (86) Zhang, G. B. Protonic Conduction in Ba₂In₂O₅. *Solid State Ionics* **1995**, *82* (3–4), 153–160. [https://doi.org/10.1016/0167-2738\(95\)00199-8](https://doi.org/10.1016/0167-2738(95)00199-8).
- (87) Islam, M. S.; Davies, R. A.; Fisher, C. A. J.; Chadwick, A. V. Defects and Protons in the CaZrO₃ Perovskite and Ba₂In₂O₅ Brownmillerite : Computer Modelling and EXAFS Studies. *Solid State Ionics* **2001**, *145*, 333–338.
- (88) Fisher, C. A. J.; Islam, M. S.; Brook, R. J. A Computer Simulation Investigation of Brownmillerite-Structured Ba₂In₂O₅. *J. Solid State Chem.* **1997**, *128* (1), 137–141. <https://doi.org/https://doi.org/10.1006/jssc.1996.7187>.
- (89) Bielecki, J.; Parker, S. F.; Mazzei, L.; Börjesson, L.; Karlsson, M. Structure and Dehydration Mechanism of the Proton Conducting Oxide Ba₂In₂O₅(H₂O)_X. *J. Mater. Chem. A* **2016**, *4* (4), 1224–1232. <https://doi.org/10.1039/C5TA05728K>.

- (90) Perrichon, A.; Jiménez-Ruiz, M.; Mazzei, L.; Rahman, S. M. H.; Karlsson, M. Local Structure and Vibrational Dynamics of Proton Conducting Ba₂In₂O₅(H₂O)_x. *J. Mater. Chem. A* **2019**, *7* (29), 17626–17636. <https://doi.org/10.1039/C9TA04056K>.
- (91) Lu, N.; Wang, Y.; Qiao, S.; Li, H.-B.; He, Q.; Li, Z.; Wang, M.; Zhang, J.; Tsang, S. C.; Guo, J.; Yang, S.; Zhang, J.; Deng, K.; Zhang, D.; Ma, J.; Wu, Y.; Zhu, J.; Tokura, Y.; Nan, C.; Wu, J.; Yu, P. A Protonated Brownmillerite Electrolyte for Superior Low-Temperature Proton Conductivity. *e-print arXiv:1811.10802* **2018**.
- (92) Kendrick, E.; Kendrick, J.; Knight, K. S.; Islam, M. S.; Slater, P. R. Cooperative Mechanisms of Fast-Ion Conduction in Gallium-Based Oxides with Tetrahedral Moieties. *Nat. Mater.* **2007**, *6* (11), 871–875. <https://doi.org/10.1038/nmat2039>.
- (93) Kreuer, K. D.; Dippel, T.; Baikov, Y. M.; Maier, J. Water Solubility, Proton and Oxygen Diffusion in Acceptor Doped BaCeO₃: A Single Crystal Analysis. *Solid State Ionics* **1996**, *86–88*, 613–620. [https://doi.org/https://doi.org/10.1016/0167-2738\(96\)00221-4](https://doi.org/10.1016/0167-2738(96)00221-4).
- (94) Mo, Y.; Ong, S. P.; Ceder, G. First Principles Study of the Li₁₀GeP₂S₁₂ Lithium Super Ionic Conductor Material. *Chem. Mater.* **2012**, *24* (1), 15–17. <https://doi.org/10.1021/cm203303y>.
- (95) He, X.; Mo, Y. Accelerated Materials Design of Na_{0.5}Bi_{0.5}TiO₃ Oxygen Ionic Conductors Based on First Principles Calculations. *Phys. Chem. Chem. Phys.* **2015**, *17* (27), 18035–18044. <https://doi.org/10.1039/c5cp02181b>.
- (96) Zhu, Y.; He, X.; Mo, Y. Origin of Outstanding Stability in the Lithium Solid

- Electrolyte Materials: Insights from Thermodynamic Analyses Based on First-Principles Calculations. *ACS Appl. Mater. Interfaces* **2015**, *7* (42), 23685–23693. <https://doi.org/10.1021/acsami.5b07517>.
- (97) He, X.; Zhu, Y.; Mo, Y. Origin of Fast Ion Diffusion in Super-Ionic Conductors. *Nat. Commun.* **2017**, *8* (May), 1–7. <https://doi.org/10.1038/ncomms15893>.
- (98) Zhu, Y.; He, X.; Mo, Y. First Principles Study on Electrochemical and Chemical Stability of Solid Electrolyte–Electrode Interfaces in All-Solid-State Li-Ion Batteries. *J. Mater. Chem. A* **2016**, *4* (9), 3253–3266. <https://doi.org/10.1039/C5TA08574H>.
- (99) Bai, Q.; He, X.; Zhu, Y.; Mo, Y. First-Principles Study of Oxyhydride H - Ion Conductors: Toward Facile Anion Conduction in Oxide-Based Materials. *ACS Appl. Energy Mater.* **2018**, *1* (4), 1626–1634. <https://doi.org/10.1021/acsaem.8b00077>.
- (100) Nolan, A. M.; Liu, Y.; Mo, Y. Solid-State Chemistries Stable with High-Energy Cathodes for Lithium-Ion Batteries. *ACS Energy Lett.* **2019**, *4* (10), 2444–2451. <https://doi.org/10.1021/acseenergylett.9b01703>.
- (101) Zhu, F.; Islam, M. S.; Zhou, L.; Gu, Z.; Liu, T.; Wang, X.; Luo, J.; Nan, C. W.; Mo, Y.; Ma, C. Single-Atom-Layer Traps in a Solid Electrolyte for Lithium Batteries. *Nat. Commun.* **2020**, *11* (1), 1–9. <https://doi.org/10.1038/s41467-020-15544-x>.
- (102) Zhu, Y.; He, X.; Mo, Y. Strategies Based on Nitride Materials Chemistry to Stabilize Li Metal Anode. *Adv. Sci.* **2017**, *4* (8), 1600517. <https://doi.org/https://doi.org/10.1002/advs.201600517>.

- (103) Nolan, A. M.; Wachsman, E. D.; Mo, Y. Computation-Guided Discovery of Coating Materials to Stabilize the Interface between Lithium Garnet Solid Electrolyte and High-Energy Cathodes for All-Solid-State Lithium Batteries. *Energy Storage Mater.* **2021**, *41*, 571–580. <https://doi.org/https://doi.org/10.1016/j.ensm.2021.06.027>.
- (104) Nolan, A. M.; Zhu, Y.; He, X.; Bai, Q.; Mo, Y. Computation-Accelerated Design of Materials and Interfaces for All-Solid-State Lithium-Ion Batteries. *Joule* **2018**, *2* (10), 2016–2046. <https://doi.org/https://doi.org/10.1016/j.joule.2018.08.017>.
- (105) Bai, Q.; Yang, L.; Chen, H.; Mo, Y. Computational Studies of Electrode Materials in Sodium-Ion Batteries. *Adv. Energy Mater.* **2018**, *8* (17), 1702998. <https://doi.org/https://doi.org/10.1002/aenm.201702998>.
- (106) Bai, Q.; Zhu, Y.; He, X.; Wachsman, E.; Mo, Y. First Principles Hybrid Functional Study of Small Polarons in Doped SrCeO₃ Perovskite: Towards Computation Design of Materials with Tailored Polaron. *Ionics (Kiel)*. **2018**, *24* (4), 1139–1151. <https://doi.org/10.1007/s11581-017-2268-6>.
- (107) Zhu, Y.; Mo, Y. Materials Design Principles for Air-Stable Lithium/Sodium Solid Electrolytes. *Angew. Chemie Int. Ed.* **2020**, *59* (40), 17472–17476. <https://doi.org/10.1002/anie.202007621>.
- (108) He, X.; Bai, Q.; Liu, Y.; Nolan, A. M.; Ling, C.; Mo, Y. Crystal Structural Framework of Lithium Super-Ionic Conductors. *Adv. Energy Mater.* **2019**, *9* (43), 1–12. <https://doi.org/10.1002/aenm.201902078>.
- (109) Liu, Y.; Wang, S.; Nolan, A. M.; Ling, C.; Mo, Y. Tailoring the Cation Lattice

- for Chloride Lithium-Ion Conductors. *Adv. Energy Mater.* **2020**, *10* (40), 2002356. <https://doi.org/10.1002/aenm.202002356>.
- (110) Kang, S. G.; Sholl, D. S. First Principles Assessment of Perovskite Dopants for Proton Conductors with Chemical Stability and High Conductivity. *RSC Adv.* **2013**, *3* (10), 3333–3341. <https://doi.org/10.1039/c2ra23405j>.
- (111) Fabbri, E.; Pergolesi, D.; Traversa, E. Materials Challenges toward Proton-Conducting Oxide Fuel Cells: A Critical Review. *Chem. Soc. Rev.* **2010**, *39* (11), 4355–4369. <https://doi.org/10.1039/b902343g>.
- (112) Münch, W.; Kreuer, K.-D.; Seifert, G.; Maier, J. Proton Diffusion in Perovskites: Comparison between BaCeO₃, BaZrO₃, SrTiO₃, and CaTiO₃ Using Quantum Molecular Dynamics. *Solid State Ionics* **2000**, *136–137*, 183–189. [https://doi.org/10.1016/S0167-2738\(00\)00304-0](https://doi.org/10.1016/S0167-2738(00)00304-0).
- (113) Dawson, J. A.; Miller, J. A.; Tanaka, I. First-Principles Insight into the Hydration Ability and Proton Conduction of the Solid State Proton Conductor, *y* and Sn Co-Doped BaZrO₃. *Chem. Mater.* **2015**, *27* (3), 901–908. <https://doi.org/10.1021/cm504110y>.
- (114) Mather, G. C.; Islam, M. S. Defect and Dopant Properties of the SrCeO₃-Based Proton Conductor. *Chem. Mater.* **2005**, *17* (7), 1736–1744. <https://doi.org/10.1021/cm047976l>.
- (115) Sundell, P. G.; Björketun, M. E.; Wahnström, G. Density-Functional Calculations of Prefactors and Activation Energies for H Diffusion in BaZr O₃. *Phys. Rev. B - Condens. Matter Mater. Phys.* **2007**, *76* (9), 1–7. <https://doi.org/10.1103/PhysRevB.76.094301>.

- (116) Wang, Y. Z.; Bevillon, E.; Chesnaud, A.; Geneste, G.; Dezanneau, G. Atomistic Simulation of Pure and Doped BaSnO₃. *J. Phys. Chem. C* **2009**, *113* (47), 20486–20492. <https://doi.org/10.1021/jp9054878>.
- (117) Fjeld, H.; Toyoura, K.; Haugrud, R.; Norby, T. Proton Mobility through a Second Order Phase Transition: Theoretical and Experimental Study of LaNbO₄. *Phys. Chem. Chem. Phys.* **2010**, *12* (35), 10313–10319. <https://doi.org/10.1039/c002851g>.
- (118) Islam, M. S.; Slater, P. R.; Tolchard, J. R.; Dinges, T. Doping and Defect Association in AZrO₃ (A = Ca, Ba) and LaMO₃ (M = Sc, Ga) Perovskite-Type Ionic Conductors. *Dalt. Trans.* **2004**, *3* (19), 3061–3066. <https://doi.org/10.1039/b402669C>.
- (119) Balachandran, J.; Lin, L.; Anchell, J. S.; Bridges, C. A.; Ganesh, P. Defect Genome of Cubic Perovskites for Fuel Cell Applications. *J. Phys. Chem. C* **2017**, *121* (48), 26637–26647. <https://doi.org/10.1021/acs.jpcc.7b08716>.
- (120) Takahashi, H.; Yashima, I.; Amezawa, K.; Eguchi, K.; Matsumoto, H.; Takamura, H.; Yamaguchi, S. First-Principles Calculations for the Energetics of the Hydration Reaction of Acceptor-Doped BaZrO₃. *Chem. Mater.* **2017**, *29* (4), 1518–1526. <https://doi.org/10.1021/acs.chemmater.6b03907>.
- (121) Bandura, A. V.; Evarestov, R. A.; Kuruch, D. D. Hybrid HF-DFT Modeling of Monolayer Water Adsorption on (001) Surface of Cubic BaHfO₃ and BaZrO₃ Crystals. *Surf. Sci.* **2010**, *604* (19–20), 1591–1597. <https://doi.org/10.1016/j.susc.2010.05.030>.
- (122) Islam, M. S.; Simanjuntak, P.; Mitra, S.; Sakidja, R. DFT Study on the Li

- Mobility in Li-Ion-Based Solid-State Electrolytes. *MRS Adv.* **2017**, *2* (54), 3277–3282. <https://doi.org/DOI: 10.1557/adv.2017.393>.
- (123) Wang, S.; Bai, Q.; Nolan, A. M.; Liu, Y.; Gong, S.; Sun, Q.; Mo, Y. Lithium Chlorides and Bromides as Promising Solid-State Chemistries for Fast Ion Conductors with Good Electrochemical Stability. *Angew. Chemie Int. Ed.* **2019**, *58* (24), 8039–8043. <https://doi.org/https://doi.org/10.1002/anie.201901938>.
- (124) Ding, P.; Li, W.; Zhao, H.; Wu, C.; Zhao, L.; Dong, B.; Wang, S. Review on Ruddlesden-Popper Perovskites as Cathode for Solid Oxide Fuel Cells. *JPhys Mater.* **2021**, *4* (2). <https://doi.org/10.1088/2515-7639/abe392>.
- (125) Dawson, J. A.; Tanaka, I. Proton Trapping in γ and Sn Co-Doped BaZrO₃. *J. Mater. Chem. A* **2015**, *3* (18), 10045–10051. <https://doi.org/10.1039/c5ta01450f>.
- (126) Jacobs, R.; Mayeshiba, T.; Booske, J.; Morgan, D. Material Discovery and Design Principles for Stable, High Activity Perovskite Cathodes for Solid Oxide Fuel Cells. *Adv. Energy Mater.* **2018**, *8* (11), 1702708. <https://doi.org/https://doi.org/10.1002/aenm.201702708>.
- (127) Gomez, M. A.; Chunduru, M.; Chigweshe, L.; Foster, L.; Fensin, S. J.; Fletcher, K. M.; Fernandez, L. E. The Effect of Yttrium Dopant on the Proton Conduction Pathways of BaZrO₃, a Cubic Perovskite. *J. Chem. Phys.* **2010**, *132* (21). <https://doi.org/10.1063/1.3447377>.
- (128) Perdew, J. P.; Ernzerhof, M.; Burke, K. Rationale for Mixing Exact Exchange with Density Functional Approximations. *J. Chem. Phys.* **1996**, *105* (22), 9982–9985. <https://doi.org/10.1063/1.472933>.
- (129) Kresse, G.; Hafner, J. Ab Initio Molecular Dynamics for Liquid Metals. *Phys.*

- Rev. B* **1993**, 47 (1), 558–561. <https://doi.org/10.1103/PhysRevB.47.558>.
- (130) Jain, A.; Hautier, G.; Moore, C. J.; Ping Ong, S.; Fischer, C. C.; Mueller, T.; Persson, K. A.; Ceder, G. A High-Throughput Infrastructure for Density Functional Theory Calculations. *Comput. Mater. Sci.* **2011**, 50 (8), 2295–2310. <https://doi.org/10.1016/j.commatsci.2011.02.023>.
- (131) Ong, S. P.; Richards, W. D.; Jain, A.; Hautier, G.; Kocher, M.; Cholia, S.; Gunter, D.; Chevrier, V. L.; Persson, K. A.; Ceder, G. Python Materials Genomics (Pymatgen): A Robust, Open-Source Python Library for Materials Analysis. *Comput. Mater. Sci.* **2013**, 68, 314–319. <https://doi.org/10.1016/j.commatsci.2012.10.028>.
- (132) Wang, L.; Maxisch, T.; Ceder, G. Oxidation Energies of Transition Metal Oxides within the $\mathit{GGA}+\mathit{U}$ Framework. *Phys. Rev. B* **2006**, 73 (19), 195107. <https://doi.org/10.1103/PhysRevB.73.195107>.
- (133) Sheppard, D.; Terrell, R.; Henkelman, G. Optimization Methods for Finding Minimum Energy Paths. *J. Chem. Phys.* **2008**, 128 (13), 1–10. <https://doi.org/10.1063/1.2841941>.
- (134) Ong, S. P.; Wang, L.; Kang, B.; Ceder, G. Li - Fe - P - O₂ Phase Diagram from First Principles Calculations. *Chem. Mater.* **2008**, 20 (5), 1798–1807. <https://doi.org/10.1021/cm702327g>.
- (135) Nolan, A. M.; Zhu, Y.; He, X.; Bai, Q.; Mo, Y. Computation-Accelerated Design of Materials and Interfaces for All-Solid-State Lithium-Ion Batteries. *Joule* **2018**, 2 (10), 2016–2046. <https://doi.org/10.1016/j.joule.2018.08.017>.
- (136) Glazer, A. M. The Classification of Tilted Octahedra in Perovskites. *Acta*

Crystallogr. Sect. B Struct. Crystallogr. Cryst. Chem. **1972**, 28 (11), 3384–3392.
<https://doi.org/10.1107/s0567740872007976>.

- (137) Brivio, F.; Frost, J. M.; Skelton, J. M.; Jackson, A. J.; Weber, O. J.; Weller, M. T.; Goñi, A. R.; Leguy, A. M. A.; Barnes, P. R. F.; Walsh, A. Lattice Dynamics and Vibrational Spectra of the Orthorhombic, Tetragonal, and Cubic Phases of Methylammonium Lead Iodide. *Phys. Rev. B - Condens. Matter Mater. Phys.* **2015**, 92 (14), 1–8. <https://doi.org/10.1103/PhysRevB.92.144308>.
- (138) Shimojo, F.; Hoshino, K.; Okazaki, H. First-Principles Molecular-Dynamics Simulation of Proton Diffusion in Perovskite Oxides. *Solid State Ionics* **1998**, 113–115, 319–323. [https://doi.org/10.1016/s0167-2738\(98\)00296-3](https://doi.org/10.1016/s0167-2738(98)00296-3).
- (139) Kreuer, K.-D.; Fuchs, A.; Maier, J. HD Isotope Effect of Proton Conductivity and Proton Conduction Mechanism in Oxides. *Solid State Ionics* **1995**, 77, 157–162. [https://doi.org/10.1016/0167-2738\(94\)00265-T](https://doi.org/10.1016/0167-2738(94)00265-T).
- (140) Kreuer, K. D.; Adams, S.; Münch, W.; Fuchs, A.; Klock, U.; Maier, J. Proton Conducting Alkaline Earth Zirconates and Titanates for High Drain Electrochemical Applications. *Solid State Ionics* **2001**, 145 (1), 295–306. [https://doi.org/10.1016/S0167-2738\(01\)00953-5](https://doi.org/10.1016/S0167-2738(01)00953-5).
- (141) Bohn, H. G.; Schober, T. Electrical Conductivity of the High-Temperature Proton Conductor BaZr_{0.9}Y_{0.1}O_{2.95}. *J. Am. Ceram. Soc.* **2000**, 83 (4), 768–772. <https://doi.org/10.1111/j.1151-2916.2000.tb01272.x>.
- (142) Polfus, J. M.; Norby, T.; Bredesen, R. Protons in Oxysulfides, Oxysulfates, and Sulfides: A First-Principles Study of La₂O₂S, La₂O₂SO₄, SrZrS₃, and BaZrS₃. *J. Phys. Chem. C* **2015**, 119 (42), 23875–23882.

<https://doi.org/10.1021/acs.jpcc.5b08278>.

- (143) Scherban, T.; Nowick, A. S. Bulk Protonic Conduction in Yb-Doped SrCeO₃. *Solid State Ionics* **1989**, *35* (1), 189–194.
[https://doi.org/https://doi.org/10.1016/0167-2738\(89\)90029-5](https://doi.org/https://doi.org/10.1016/0167-2738(89)90029-5).
- (144) Scherban, T.; Lee, W.-K.; Nowick, A. S. Bulk Protonic Conduction in Yb-Doped SrCeO₃ and BaCeO₃. *Solid State Ionics* **1988**, *28–30*, 585–588.
[https://doi.org/https://doi.org/10.1016/S0167-2738\(88\)80106-1](https://doi.org/https://doi.org/10.1016/S0167-2738(88)80106-1).
- (145) Liu, J. F.; Nowick, A. S. The Incorporation and Migration of Protons in Nd-Doped BaCeO₃. *Solid State Ionics* **1992**, *50* (1), 131–138.
[https://doi.org/https://doi.org/10.1016/0167-2738\(92\)90045-Q](https://doi.org/https://doi.org/10.1016/0167-2738(92)90045-Q).
- (146) Shi, Z.; Sun, W.; Wang, Z.; Qian, J.; Liu, W. Samarium and Yttrium Codoped BaCeO₃ Proton Conductor with Improved Sinterability and Higher Electrical Conductivity. *ACS Appl. Mater. Interfaces* **2014**, *6* (7), 5175–5182.
<https://doi.org/10.1021/am500467m>.
- (147) Kreuer, K. D.; Schönherr, E.; Maier, J. Proton and Oxygen Diffusion in BaCeO₃ Based Compounds: A Combined Thermal Gravimetric Analysis and Conductivity Study. *Solid State Ionics* **1994**, *70–71*, 278–284.
[https://doi.org/https://doi.org/10.1016/0167-2738\(94\)90323-9](https://doi.org/https://doi.org/10.1016/0167-2738(94)90323-9).
- (148) Münch, W.; Kreuer, K. D.; Adams; Seifert, G.; Maier, J. The Relation between Crystal Structure and the Formation and Mobility of Protonic Charge Carriers in Perovskite-Type Oxides: A Case Study of Y-Doped BaCeO₃ and SrCeO₃. *Phase Transitions* **1999**, *68* (3), 567–586.
<https://doi.org/10.1080/01411599908224535>.

- (149) Ketkaew, R.; Tantirungrotechai, Y.; Harding, P.; Chastanet, G.; Guionneau, P.; Marchivie, M.; Harding, D. J. OctaDist: A Tool for Calculating Distortion Parameters in Spin Crossover and Coordination Complexes. *Dalt. Trans.* **2021**, *50* (3), 1086–1096. <https://doi.org/10.1039/D0DT03988H>.
- (150) Falcón, H.; Barbero, J. A.; Alonso, J. A.; Martínez-Lope, M. J.; Fierro, J. L. G. SrFeO_{3-δ} Perovskite Oxides: Chemical Features and Performance for Methane Combustion. *Chem. Mater.* **2002**, *14* (5), 2325–2333. <https://doi.org/10.1021/cm011292l>.
- (151) Matsuo, S.; Yugami, H.; Ishigame, M. Local Proton Dynamics in Perovskite-Type Protonic Conductors by Spectral Hole Burning Spectroscopy. *Phys. Rev. B - Condens. Matter Mater. Phys.* **2001**, *64* (2), 243021–243026. <https://doi.org/10.1103/PhysRevB.64.024302>.
- (152) Sata, N.; Hiramoto, K.; Ishigame, M.; Hosoya, S. Site Identification of Protons in: Mechanism for Large Protonic Conduction. *Phys. Rev. B - Condens. Matter Mater. Phys.* **1996**, *54* (22), 15795–15799. <https://doi.org/10.1103/PhysRevB.54.15795>.
- (153) Unemoto, A.; Kaimai, A.; Sato, K.; Yashiro, K.; Matsumoto, H.; Mizusaki, J.; Amezawa, K.; Kawada, T. Hydrogen Permeability and Electrical Properties in Oxide Composites. *Solid State Ionics* **2008**, *178* (31), 1663–1667. <https://doi.org/https://doi.org/10.1016/j.ssi.2007.11.001>.
- (154) Macías, J.; Yaremchenko, A. A.; Rodríguez-Castellón, E.; Sarykevich, M.; Frade, J. R. Compromising Between Phase Stability and Electrical Performance: SrVO₃–SrTiO₃ Solid Solutions as Solid Oxide Fuel Cell Anode Components.

- ChemSusChem* **2019**, *12* (1), 240–251. <https://doi.org/10.1002/cssc.201801727>.
- (155) Tahini, H. A.; Tan, X.; Schwingenschlögl, U.; Smith, S. C. In Operando Self-Healing of Perovskite Electrocatalysts: A Case Study of SrCoO₃ for the Oxygen Evolution Reaction. *Part. Part. Syst. Charact.* **2017**, *34* (4). <https://doi.org/10.1002/ppsc.201600280>.
- (156) He, Z.; Nie, J.; Liu, K.; Sivajee Ganesh, K.; Akbar, M.; Xia, C.; Wang, X.; Dong, W.; Huang, J.; Wang, B. Compositing Protonic Conductor BaZr_{0.5}Y_{0.5}O₃ (BZY) with Triple Conductor BaCo_{0.4}Fe_{0.4}Zr_{0.1}Y_{0.1}O_{3-δ} (BCFZY) as Electrolyte for Advanced Solid Oxide Fuel Cell. *Int. J. Hydrogen Energy* **2020**, *3* (xxxx), 1–10. <https://doi.org/10.1016/j.ijhydene.2020.06.102>.
- (157) Vasala, S.; Karppinen, M. A₂B'B''O₆ Perovskites: A Review. *Prog. Solid State Chem.* **2015**, *43* (1), 1–36. <https://doi.org/https://doi.org/10.1016/j.progsolidstchem.2014.08.001>.
- (158) Day, B. E.; Bley, N. D.; Jones, H. R.; McCullough, R. M.; Eng, H. W.; Porter, S. H.; Woodward, P. M.; Barnes, P. W. Structures of Ordered Tungsten- or Molybdenum-Containing Quaternary Perovskite Oxides. *J. Solid State Chem.* **2012**, *185*, 107–116. <https://doi.org/https://doi.org/10.1016/j.jssc.2011.11.007>.
- (159) Wallace, T. K.; Colman, R. H.; McLaughlin, A. C. A Variable Temperature Synchrotron X-Ray Diffraction Study of the Ferroelastic Double Perovskite Ba₂GdMoO₆. *Phys. Chem. Chem. Phys.* **2013**, *15* (22), 8672–8677. <https://doi.org/10.1039/C2CP43732E>.
- (160) Kasamatsu, S.; Sugino, O.; Ogawa, T.; Kuwabara, A. Dopant Arrangements in Y-Doped BaZrO₃ under Processing Conditions and Their Impact on Proton

- Conduction: A Large-Scale First-Principles Thermodynamics Study. *J. Mater. Chem. A* **2020**, *8* (25), 12674–12686. <https://doi.org/10.1039/d0ta01741h>.
- (161) Yin, W. J.; Weng, B.; Ge, J.; Sun, Q.; Li, Z.; Yan, Y. Oxide Perovskites, Double Perovskites and Derivatives for Electrocatalysis, Photocatalysis, and Photovoltaics. *Energy Environ. Sci.* **2019**, *12* (2), 442–462. <https://doi.org/10.1039/c8ee01574k>.
- (162) Tsang, S.-C.; Zhang, J.; Tse, K.; Zhu, J. Towards Understanding the Special Stability of SrCoO_{2.5} and HSrCoO_{2.5}. *Phys. Rev. Mater.* **2019**, *3* (2), 24603. <https://doi.org/10.1103/PhysRevMaterials.3.024603>.
- (163) Muñoz, A.; De La Calle, C.; Alonso, J. A.; Botta, P. M.; Pardo, V.; Baldomir, D.; Rivas, J. Crystallographic and Magnetic Structure of SrCoO_{2.5} Brownmillerite: Neutron Study Coupled with Band-Structure Calculations. *Phys. Rev. B - Condens. Matter Mater. Phys.* **2008**, *78* (5). <https://doi.org/10.1103/PhysRevB.78.054404>.
- (164) Jeen, H.; Choi, W. S.; Freeland, J. W.; Ohta, H.; Jung, C. U.; Lee, H. N. Topotactic Phase Transformation of the Brownmillerite SrCoO_{2.5} to the Perovskite SrCoO_{3-δ}. *Adv. Mater.* **2013**, *25* (27), 3651–3656. <https://doi.org/10.1002/adma.201300531>.
- (165) Munch, W. A Quantum Molecular Dynamics Study of Proton Diffusion in SrTiO₃. **1999**, *125*, 39–45.
- (166) Henkelman, G.; Arnaldsson, A.; Jónsson, H. A Fast and Robust Algorithm for Bader Decomposition of Charge Density. *Comput. Mater. Sci.* **2006**, *36* (3), 354–360. <https://doi.org/10.1016/j.commatsci.2005.04.010>.

- (167) Liang, L.; Qiao, S.; Du, S.; Zhang, S.; Wu, J.; Liu, Z. Role of Interstitial Hydrogen in SrCoO_{2.5} Antiferromagnetic Insulator. *Phys. Rev. Mater.* **2018**, *2* (11), 1–5. <https://doi.org/10.1103/PhysRevMaterials.2.114409>.
- (168) Chandra, S.; Singh, N.; Hashmi, S. A. Proton Conduction in Solids. In *Proc Indian Nat Acad*; 1986; Vol. 52, pp 338–362.
- (169) Hull, S. Superionics: Crystal Structures and Conduction Processes. *Reports Prog. Phys.* **2004**, *67* (7), 1233–1314. <https://doi.org/10.1088/0034-4885/67/7/R05>.
- (170) Ong, S. P.; Mo, Y.; Ceder, G. Low Hole Polaron Migration Barrier in Lithium Peroxide. *Phys. Rev. B* **2012**, *85* (8), 81105. <https://doi.org/10.1103/PhysRevB.85.081105>.
- (171) Liao, P.; Toroker, M. C.; Carter, E. A. Electron Transport in Pure and Doped Hematite. *Nano Lett.* **2011**, *11* (4), 1775–1781. <https://doi.org/10.1021/nl200356n>.
- (172) Maxisch, T.; Zhou, F.; Ceder, G. Ab Initio Study of the Migration of Small Polarons in Olivine Li_xFePO₄ and Their Association with Lithium Ions and Vacancies. *Phys. Rev. B* **2006**, *73* (10), 104301. <https://doi.org/10.1103/PhysRevB.73.104301>.
- (173) de Grotthuss, C. J. T. *Mémoire Sur La Décomposition de l'eau: Et Des Corps Qu' Elle Tient En Dissolution à l'aide de l'électricité Galvanique*; publisher not identified, 1805.
- (174) Kweon, K. E.; Varley, J. B.; Shea, P.; Adelstein, N.; Mehta, P.; Heo, T. W.; Udovic, T. J.; Stavila, V.; Wood, B. C. Structural, Chemical, and Dynamical

- Frustration: Origins of Superionic Conductivity in Closo-Borate Solid Electrolytes. *Chem. Mater.* **2017**, *29* (21), 9142–9153. <https://doi.org/10.1021/acs.chemmater.7b02902>.
- (175) Kreuer, K. D. Aspects of the Formation and Mobility of Protonic Charge Carriers and the Stability of Perovskite-Type Oxides. *Solid State Ionics* **1999**, *125* (1), 285–302. [https://doi.org/10.1016/S0167-2738\(99\)00188-5](https://doi.org/10.1016/S0167-2738(99)00188-5).
- (176) Xu, X.; Liu, C.; Ma, J.; Jacobson, A. J.; Nan, C.; Chen, C. Physicochemical Properties of Proton-Conducting SmNiO₃ Epitaxial Films. *ACS Mater. Lett.* **2019**, *5*, 247–251. <https://doi.org/10.1021/jm50001a011>.
- (177) Kreuer, K. D.; Adams, S.; Münch, W.; Fuchs, A.; Klock, U.; Maier, J. Proton Conducting Alkaline Earth Zirconates and Titanates for High Drain Electrochemical Applications. *Solid State Ionics* **2001**, *145* (1–4), 295–306. [https://doi.org/10.1016/S0167-2738\(01\)00953-5](https://doi.org/10.1016/S0167-2738(01)00953-5).
- (178) Iwahara, H.; Yajima, T.; Hibino, T.; Ozaki, K.; Suzuki, H. Protonic Conduction in Calcium, Strontium and Barium Zirconates. *Solid State Ionics* **1993**, *61* (1–3), 65–69. [https://doi.org/10.1016/0167-2738\(93\)90335-Z](https://doi.org/10.1016/0167-2738(93)90335-Z).
- (179) Iwahara, H.; Uchida, H.; Tanaka, S. High Temperature Type Proton Conductor Based on SrCeO₃ and Its Application to Solid Electrolyte Fuel Cells. *Solid State Ionics* **1983**, *9–10*, 1021–1025. [https://doi.org/10.1016/0167-2738\(83\)90125-X](https://doi.org/10.1016/0167-2738(83)90125-X).
- (180) Düvel, A.; Heitjans, P.; Fedorov, P.; Scholz, G.; Cibin, G.; Chadwick, A. V.; Pickup, D. M.; Ramos, S.; Sayle, L. W. L.; Sayle, E. K. L.; Sayle, T. X. T.; Sayle, D. C. Is Geometric Frustration-Induced Disorder a Recipe for High Ionic

- Conductivity? *J. Am. Chem. Soc.* **2017**, *139* (16), 5842–5848.
<https://doi.org/10.1021/jacs.7b00502>.
- (181) Stefano, D. Di; Miglio, A.; Robeyns, K.; Filinchuk, Y.; Lechartier, M.; Senyshyn, A.; Ishida, H.; Spannenberger, S.; Prutsch, D.; Lunghammer, S.; Rettenwander, D.; Wilkening, M.; Roling, B.; Kato, Y.; Hautier, G. Superionic Diffusion through Frustrated Energy Landscape. *Chem* **2019**, *5* (9), 2450–2460.
<https://doi.org/https://doi.org/10.1016/j.chempr.2019.07.001>.
- (182) Thangadurai, V.; Narayanan, S.; Pinzaru, D. Garnet-Type Solid-State Fast Li Ion Conductors for Li Batteries: Critical Review. *Chem. Soc. Rev.* **2014**, *43* (13), 4714–4727. <https://doi.org/10.1039/c4cs00020j>.
- (183) Kamaya, N.; Homma, K.; Yamakawa, Y.; Hirayama, M.; Kanno, R.; Yonemura, M.; Kamiyama, T.; Kato, Y.; Hama, S.; Kawamoto, K.; Mitsui, A. A Lithium Superionic Conductor. *Nat. Mater.* **2011**, *10* (9), 682–686.
<https://doi.org/10.1038/nmat3066>.
- (184) Kato, Y.; Hori, S.; Saito, T.; Suzuki, K.; Hirayama, M.; Mitsui, A.; Yonemura, M.; Iba, H.; Kanno, R. High-Power All-Solid-State Batteries Using Sulfide Superionic Conductors. *Nat. Energy* **2016**, *1* (4), 16030.
<https://doi.org/10.1038/nenergy.2016.30>.
- (185) Xiong, S.; He, X.; Han, A.; Liu, Z.; Ren, Z.; McElhenny, B.; Nolan, A. M.; Chen, S.; Mo, Y.; Chen, H. Computation-Guided Design of LiTaSiO₅, a New Lithium Ionic Conductor with Sphene Structure. *Adv. Energy Mater.* **2019**, *9* (22), 1–11. <https://doi.org/10.1002/aenm.201803821>.
- (186) Emery, A. A.; Saal, J. E.; Kirklin, S.; Hegde, V. I.; Wolverton, C. High-

- Throughput Computational Screening of Perovskites for Thermochemical Water Splitting Applications. *Chem. Mater.* **2016**, *28* (16), 5621–5634. <https://doi.org/10.1021/acs.chemmater.6b01182>.
- (187) Hempelmann, R. Hydrogen Diffusion Mechanism in Proton Conducting Oxides. *Phys. B Condens. Matter* **1996**, *226* (1), 72–77. [https://doi.org/https://doi.org/10.1016/0921-4526\(96\)00251-7](https://doi.org/https://doi.org/10.1016/0921-4526(96)00251-7).
- (188) Matzke, T.; Stimming, U.; Karmonik, C.; Soetratmo, M.; Hempelmann, R.; Güthoff, F. Quasielastic Thermal Neutron Scattering Experiment on the Proton Conductor SrCe_{0.95}Yb_{0.05}H_{0.02}O_{2.985}. *Solid State Ionics* **1996**, *86–88*, 621–628. [https://doi.org/https://doi.org/10.1016/0167-2738\(96\)00223-8](https://doi.org/https://doi.org/10.1016/0167-2738(96)00223-8).
- (189) Hui, Z.; Michèle, P. Preparation, Chemical Stability, and Electrical Properties of Ba(Ce_{1-x}Bix)O₃ (x = 0.0–0.5). *J. Mater. Chem.* **2002**, *12* (12), 3787–3791. <https://doi.org/10.1039/B205107A>.
- (190) Fabbri, E.; Pergolesi, D.; D’Epifanio, A.; Di Bartolomeo, E.; Balestrino, G.; Licoccia, S.; Traversa, E. Design and Fabrication of a Chemically-Stable Proton Conductor Bilayer Electrolyte for Intermediate Temperature Solid Oxide Fuel Cells (IT-SOFCs). *Energy Environ. Sci.* **2008**, *1* (3), 355–359. <https://doi.org/10.1039/b806655h>.
- (191) Tanner, C. W.; Virkar, A. V. Instability of BaCeO₃ in H₂O-Containing Atmospheres. *J. Electrochem. Soc.* **1996**, *143* (4), 1386–1389. <https://doi.org/10.1149/1.1836647>.
- (192) Kim, J. H.; Kang, Y. M.; Byun, M. S.; Hwang, K. T. Study on the Chemical Stability of Y-Doped BaCeO_{3-δ} and BaZrO_{3-δ} Films Deposited by Aerosol

- Deposition. *Thin Solid Films* **2011**, *520* (3), 1015–1021.
<https://doi.org/10.1016/j.tsf.2011.08.013>.
- (193) Gopalan, S.; Virkar, A. V. Thermodynamic Stabilities of SrCeO₃ and BaCeO₃ Using a Molten Salt Method and Galvanic Cells. *J. Electrochem. Soc.* **1993**, *140* (4), 1060–1065. <https://doi.org/10.1149/1.2056197>.
- (194) Ricote, S.; Bonanos, N.; Caboche, G. Water Vapour Solubility and Conductivity Study of the Proton Conductor BaCe(0.9–x)Zr_xY_{0.1}O(3–δ). *Solid State Ionics* **2009**, *180* (14), 990–997.
<https://doi.org/https://doi.org/10.1016/j.ssi.2009.03.016>.
- (195) Zhang, C.; Zhao, H. Chemical and Structural Stability of Sm- and In- Co-Doped Proton Conductor BaCe_{0.80}–XSm_{0.20}In_xO₃–Δin Various Atmospheres. *J. Electrochem. Soc.* **2012**, *159* (7), F316–F321.
<https://doi.org/10.1149/2.083207jes>.
- (196) Saher, S.; Song, J.; Vibhu, V.; Nicollet, C.; Flura, A.; Bassat, J.-M.; Bouwmeester, H. J. M. Influence of Annealing at Intermediate Temperature on Oxygen Transport Kinetics of Pr₂NiO₄+δ. *J. Mater. Chem. A* **2018**, *6* (18), 8331–8339. <https://doi.org/10.1039/C7TA08885J>.
- (197) Wang, Z.; Yang, W.; Shafi, S. P.; Bi, L.; Wang, Z.; Peng, R.; Xia, C.; Liu, W.; Lu, Y. A High Performance Cathode for Proton Conducting Solid Oxide Fuel Cells. *J. Mater. Chem. A* **2015**, *3* (16), 8405–8412.
<https://doi.org/10.1039/C5TA00391A>.
- (198) Zhou, X.-D.; Templeton, J. W.; Nie, Z.; Chen, H.; Stevenson, J. W.; Pederson, L. R. Electrochemical Performance and Stability of the Cathode for Solid Oxide

- Fuel Cells: V. High Performance and Stable Pr₂NiO₄ as the Cathode for Solid Oxide Fuel Cells. *Electrochim. Acta* **2012**, *71*, 44–49. <https://doi.org/10.1016/j.electacta.2012.03.067>.
- (199) Bai, Q.; Yang, L.; Chen, H.; Mo, Y. Computational Studies of Electrode Materials in Sodium-Ion Batteries. *Adv. Energy Mater.* **2018**, *8* (17), 1–29. <https://doi.org/10.1002/aenm.201702998>.
- (200) Ong, S. P.; Mo, Y.; Richards, W. D.; Miara, L.; Lee, H. S.; Ceder, G. Phase Stability, Electrochemical Stability and Ionic Conductivity of the Li_{10±1}MP₂X₁₂ (M = Ge, Si, Sn, Al or P, and X = O, S or Se) Family of Superionic Conductors. *Energy Environ. Sci.* **2013**, *6* (1), 148–156. <https://doi.org/10.1039/C2EE23355J>.
- (201) Chase, M. W. NIST-JANAF Thermochemical Tables for Oxygen Fluorides. *J. Phys. Chem. Ref. data* **1996**, *25* (2), 551–603.
- (202) Krukau, A. V.; Vydrov, O. A.; Izmaylov, A. F.; Scuseria, G. E. Influence of the Exchange Screening Parameter on the Performance of Screened Hybrid Functionals. *J. Chem. Phys.* **2006**, *125* (22). <https://doi.org/10.1063/1.2404663>.
- (203) Grimme, S. Density Functional Theory with London Dispersion Corrections. *WIREs Comput. Mol. Sci.* **2011**, *1* (2), 211–228. <https://doi.org/10.1002/wcms.30>.
- (204) Grimme, S. Accurate Description of van Der Waals Complexes by Density Functional Theory Including Empirical Corrections. *J. Comput. Chem.* **2004**, *25* (12), 1463–1473. <https://doi.org/10.1002/jcc.20078>.
- (205) Gebhardt, J.; Viñes, F.; Bleiziffer, P.; Hieringer, W.; Görling, A. Hydrogen

Storage on Metal Oxide Model Clusters Using Density-Functional Methods and
Reliable van Der Waals Corrections. *Phys. Chem. Chem. Phys.* **2014**, *16* (11),
5382–5392. <https://doi.org/10.1039/c3cp54704c>.